November 2015

Protein Charge Anisotropy Mediated Self-Association And Phase Separation

Daniel P. Seeman
University of Massachusetts Amherst

PROTEIN CHARGE ANISOTROPY MEDIATED SELF-ASSOCIATION AND PHASE SEPARATION

A Dissertation Presented

by

DANIEL SEEMAN

Submitted to the Graduate School of the

University of Massachusetts Amherst in partial fulfillment

of the requirements for the degree of

DOCTOR OF PHILOSOPHY

September 2015

Chemistry

PROTEIN CHARGE ANISOTROPY MEDIATED SELF-ASSOCIATION AND PHASE SEPARATION

A Dissertation Presented

by

DANIEL SEEMAN

Approved as to style and content by:

_____

Paul L. Dubin, Chair

_____

Michael J. Knapp, Member

_____

Igor A. Kaltashov, Member

_____

Sarah L. Perry, Member

_____

Craig T. Martin, Department Head

Chemistry

DEDICATION

For all the people who helped along the way, friends, family, classmates, and colleagues; your support means more to me than you can know.

ACKNOWLEDGMENTS

I would like to thank my advisor, Prof. Paul Dubin for his continued guidance and support, for his creativity, and his unbounded enthusiasm for coacervation. I also genuinely appreciate the contributions of my committee members, Prof. Mike Knapp (UMass-Amherst, Chemistry), Prof. Igor Kaltashov (UMass-Amherst, Chemistry) who I thank for thoughtful discussions, and useful advice, both academic and career, and most recently Prof. Sarah Perry (UMass-Amherst, Chemical Engineering). Additionally I thank Prof. Surita Bhatia (Stony Brook University, Chemistry) for discussions regarding careers, proposal writing, and neutron scattering, Prof. David Hoagland (UMass-Amherst, Polymer Science/PSE) with whom we shared numerous joint group meetings, and Dr. Rachel Wollacott (UMassMed, MassBiologics). I would also like to express my appreciation to Shana Passonno, both in her role as ICE program manager, and also in the Office of Graduate and Professional Development. Additionally, I would like to thank Prof. David Pink and Bonnie Quinn, for assistance in developing Monte Carlo simulations. Also, Alex Malanowski for assistance with monoclonal antibody work.

I feel the need to recognize the role of Prof. Bob Weis (UMass-Amherst, Chemistry), who is no longer with us, but whose dedication to not only his own research, but to the development of critical scientists and researchers, has made a lasting impact on our department, and on many of its graduate students.

I also acknowledge the support of my friends, coworkers, and lab mates –past and –present, too numerous to list entirely. I am especially grateful to those with whom I have worked closely over the years including, but not limited to, Dr. Ebru Kizilay, Bingqian

Zheng, Fatih Cömert, and Dr. Yaxun Fan. Thanks also, to all members of the Dubin, Hoagland, Kaltashov, and Perry Research Groups, as well as other groups with which I have worked. And thanks to others from my incoming graduate class, including Dr. Elih Velazquez, and Dr. Muslum Yildiz, and Jamie Buske.

Lastly, but certainly not least, I thank my family, in particular my parents. My mother, Marianne Corbino who inspired interest in scientific research from a very early age; and my father, Abe Seeman, who taught me the importance of enjoying life.

ABSTRACT

PROTEIN CHARGE ANISOTROPY MEDIATED SELF-ASSOCIATION AND PHASE SEPARATION

SEPTEMBER 2015

DANIEL SEEMAN

Ph.D., UNIVERSITY OF MASSACHUSETTS AMHERST

Directed by: Professor Paul L. Dubin

Protein charge anisotropy results from the asymmetric distribution of charged residues on the exterior of a particular protein. Interactions between proteins and other macromolecules can be described in terms of attractive electrostatics; since electrostatic free energies, at optimal I, are on the order of kT, it is unlikely that such associations would result in desolvation, thus it is reasonable to consider such intermolecular attractions as being mediated by hydrated protein surfaces. Such interactions can be broken down in terms of a single protein interacting with a range of "binding partners", including (1) protein-protein interactions, (2) protein-polymer interactions, and (3) protein-surface interactions. Protein-protein interactions can be divided into two types, self-interaction, where two monomers of the same protein interact as is the case with either multimerization or aggregation; or heteroprotein interactions where two *different* proteins associate, such as is seen with

heteroprotein coacervation. Protein-polyelectrolyte (PE) interactions, have been shown to result in formation of either soluble complexes, or in the case of protein-PE coacervation, liquid-liquid phase separation (LLPS). The final case becomes useful when examining non-ideal chromatographic behavior of proteins, where interactions between protein and stationary phase can alter elution times, relative to those seen for the purely hydrodynamic (or ideal) case. In all cases it is the hydrated protein that is key to such interactions.

The aggregation of model protein β-lactoglobulin (BLG) near its isoelectric point was studied as a function of ionic strength and pH, where rates of aggregation were obtained through a highly precise and convenient pH/turbidimetric titrations. A similar titration procedure was used to obtain self-association rates of the more pharmaceutically relavent protein, monoclonal antibody (mAb), at low temperature. Antibody (mAb) centrifuged at $T < 0^{o}C$ underwent LLPS upon thawing. The dense-phase was clearly identified, and a sharp interface between mAb-enriched and mAb-depleted phases was confirmed. In cases where LLPS was induced in the presence of a dye-labeled protein of opposite charge to mAb, the two proteins were colocalized in the lower phase.

Heteroprotein coacervation of BLG and lactoferrin (LF) was examined by SANS and rheology; the molar stoichiometry in coacervate has been reported to be $LF(BLG_2)_2$ assumed to be the primary structural unit of the coacervate. Surface-bound water in protein solutions was identified by a reduction in the heat of freezing of various coacervating systems, with a specific focus on non-freezing water (NFW) in protein-protein (heteroprotein) coacervates. These results are attributed to maximization of water-protein contacts, structural features that reflect the mode of sample assembly, as they are not seen in a non-coacervated LF-BLG solution with identical concentrations of all species.

A method was developed in order to determine the yield and selectivity of coacervates prepared from monoclonal antibody (mAb) and anionic polysaccharide hyaluronic acid (HA). The yield of mAb, in such coacervates, is shown to be as high as 80%, with final concentrations of MAb-A > 170 mg/mL; the yield of HA is ca. 75%; and a selectivity ratio, S, of ca. 490 was obtained for coacervates prepared at $pH_c^{BSA} < pH < pH_\varphi^{mAb}$. Values corresponding to the start of complexation, and coacervation (pH_c, pH_φ) are reported over a range of ionic strengths, I <200mM.

Monoclonal antibody (mAb), a protein with a highly patchy (or anisotropic) surface, is shown to interact anomalously with chromatography columns at low *I*. Absolute molecular weight (MW) determination *vis-à-vis* light scattering detection, suggests that late eluting peaks, are *larger* in aggregation number than monomeric antibody. Such results suggest that despite the lower apparent size obtained from column calibration, chemical degradation *cannot* be responsible for these types of delayed elution volumes. This demonstrates the importance of equilibrium controlled protein-protein and protein-surface interactions even in single protein systems.

Protein self-interactions result in a type of LLPS with features similar to coacervation, but over a much less restricted range of conditions. Heteroprotein-interactions introduce a structural constraint that is reflected in a highly constrained set of conditions for heteroprotein coacervation. Protein-PE coacervates can be formed over a much more extended range of pH and *I*, possible due to the greater flexibility of the PE chain; and finally, direct interactions with chromatography columns may involve attractive electrostatic interactions, analogous to those seen in coacervating systems.

TABLE OF CONTENTS

Page

LIST OF TABLES

LIST OF FIGURES

Figure Page

CHAPTER 1

INTRODUCTION

1.1 Overview of Protein Electrostatics

Protein charge anisotropy results from the asymmetric distribution of charged residues on the exterior of a particular protein, such that there exists a careful balance of repulsive and attractive electrostatics, which controls interactions between like-charged proteins near their isoelectric points (pIs). Such asymmetric charge domains, or protein charge patches can facilitate attractive interactions between like-charged macromolecules (e.g., protein-polyelectrolyte, and protein-protein complexes). Because protein–protein interactions involve solvent-accessible surfaces, protein charge anisotropy is often a major factor.[1, 2]

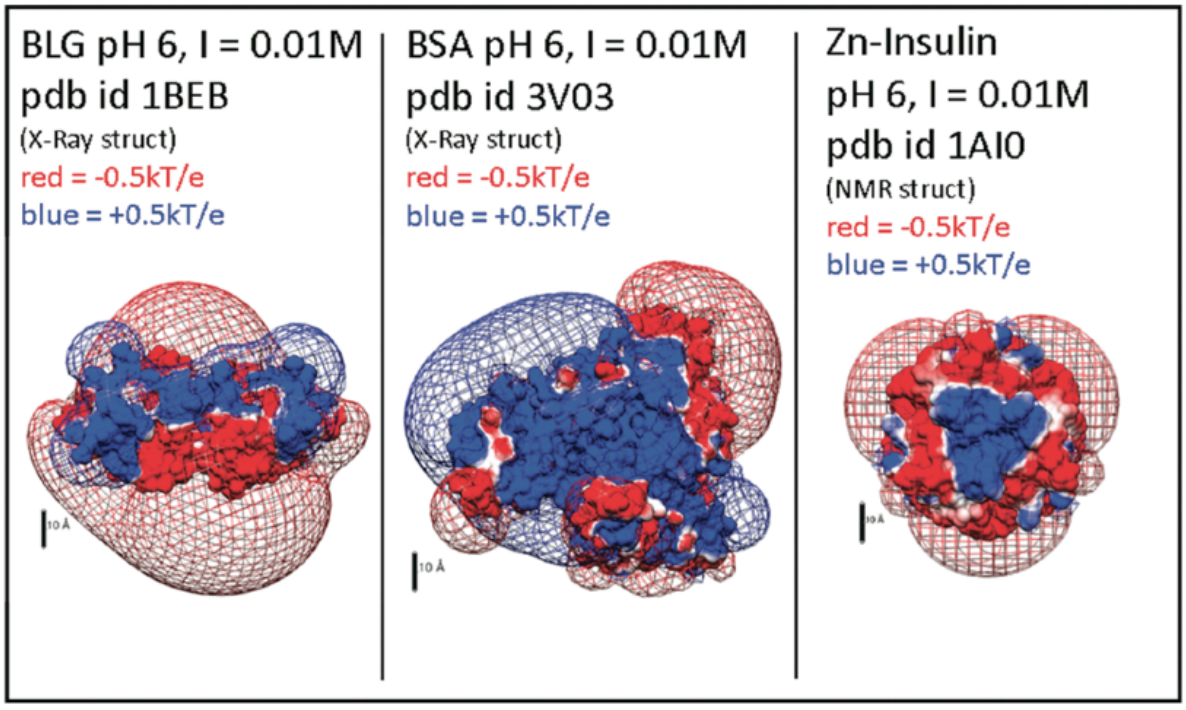

Figure 1.1: Representative charge anisotropy of three common model proteins; BLG; BSA; insulin. Scale bar = 1nm.

Protein charge anisotropy is a major component of both protein self-association, *and* interactions with polyelectrolytes (PEs). Figure 1.1 shows electrostatic potentials of three proteins: β-lactoglobulin (BLG), bovine serum albumin (BSA), and Zn-Insulin; screened electrostatics are calculated using a program called DelPhi which provides solutions to the nonlinear Poisson Boltzmann equation.[3] Isopotential contours (grids of constant potential) from such calculations are displayed at a cutoff of ±0.5 kT/e, where the electrostatic potential, ψ, is expressed in terms of thermal energy, kT, per elementary charge unit, e. The nonlinear Poisson Boltzmann equation is extremely useful for objects with arbitrary or irregular geometries, such as proteins and many other macromolecules, where no simple empirical models, based on geometry, exist.

Proper consideration of electrostatics requires an expression relating ionic strength (I) to the falloff of electrostatic potential at some distance, r, from a protein surface. For monovalent electrolytes, such as NaCl, I is directly equivalent to the molar concentration of salt. The Debye length (κ^{-1}) can then be calculated according to:

$$\kappa^{-1} = 1/\sqrt{(8\pi\lambda_B N_A I)} = 0.304/\sqrt{I} \qquad \textbf{(1.1)}$$

This expression is in terms of the Bjerrum length (λ_B = 0.6nm in H_2O) defined as the distance over which an interaction between a pair of charges is equal to thermal energy, or kT. This term, λ_B, absorbs all the temperature and solvent dependent terms, allowing for the simplification of the entire expression to κ^{-1} = 0.304/√([NaCl]), which yields the Debye length in units of nm.

A

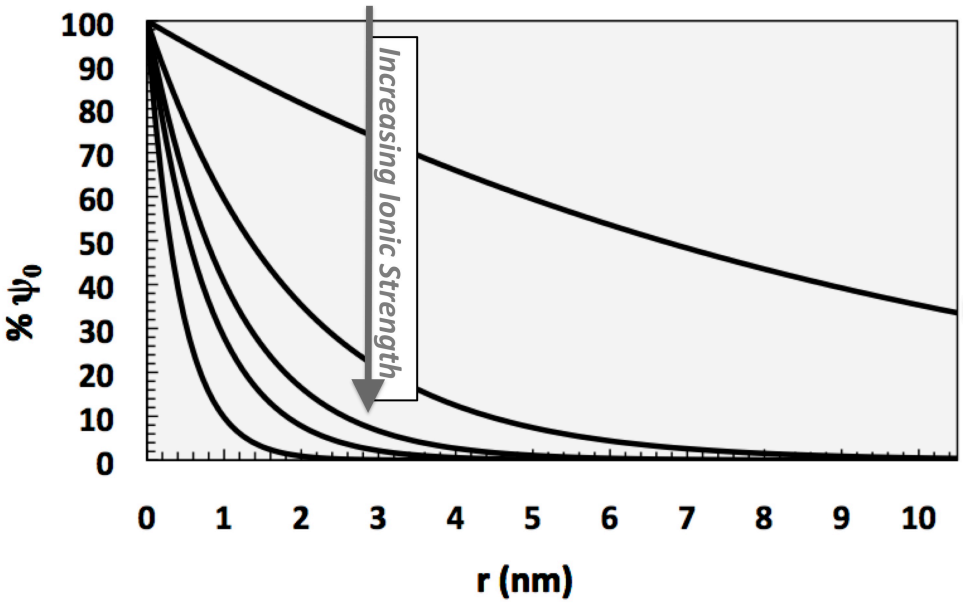

B

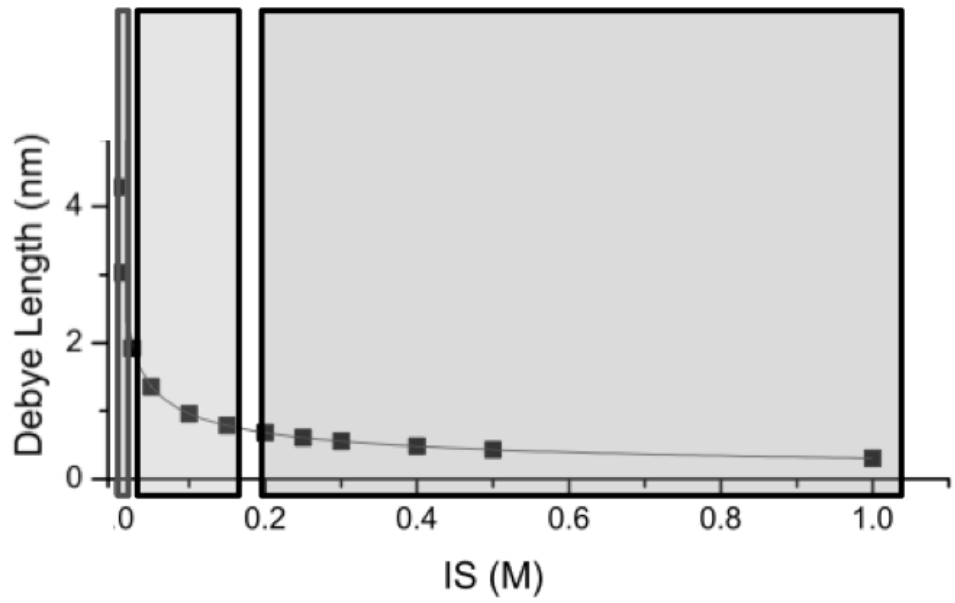

Figure 1.2: The Debye length, κ^{-1}, functions as a decay constant controlling the **(a)** falloff of an electrostatic potential, ψ(r), at a given distance, r, from a flat surface at I = 0.001, 0.025, 0.075, 0.150, and 0.500 M, with corresponding values of κ^{-1} = 9.6, 1.9, 1.1, 0.4, and 0.8 nm, (**b**) the range of electrostatic interactions is controlled by addition of salt, with the most dramatic effect at low (< 10 mM) salt, boxes correspond to regions of κ^{-1} greater than, similar to, and less than protein size.

By assuming a particular surface geometry (i.e., sphere, cylinder, or flat plane) it becomes possible to explicitly calculate a surface potential, given a known charge density. For the simple case, a flat surface of low surface potential, ψ_0, the Poisson equation can be solved explicitly, giving the result:

$$\Psi(r) = \Psi_0 \exp(-r\kappa) \tag{1.2}$$

With, κ, simply being the inverse of κ^{-1}, the Debye length. The result is that the potential decays exponentially at increasing distance from the surface, r. As *I* is increased, κ increases, meaning that the decay of the electrostatic potential with r occurs more rapidly, decreasing the distance over which the potential extends from the surface.

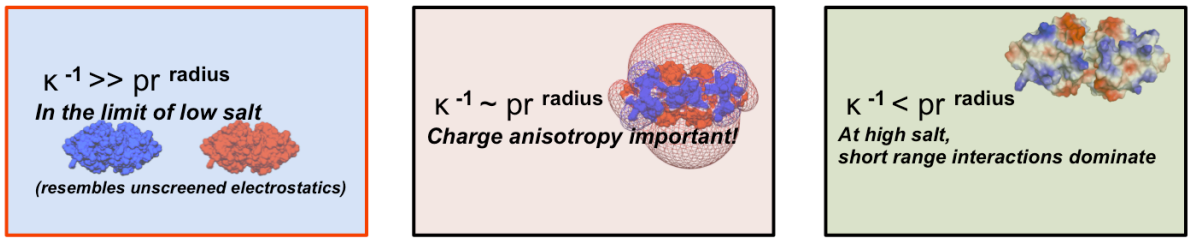

Figure 1.3: Protein structure mediates electrostatic interactions, *vis-à-vis* placement of amino charges. At intermediate *I*, the arrangement of charges results in the formation of charge domains.

The effective length-scale over which electrostatic interactions, either attractive or repulsive, can persist is controlled by ionic strength, via the effective screening length κ^{-1} (Figure 1.2B). The Debye length becomes extremely large in the limit of low salt, a condition at which electrostatic interactions start to resemble bare (unscreened) coulombics. In the case where κ^{-1} is on the order of the protein radius, the arrangement of acidic and basic residues (Figure 1.3) results in the formation of well-defined charge domains, harder to

define at very high, or very low *I*.

1.2 Measuring Protein and Amino Acid Charge

Charge asymmetry is visualized by electrostatic modeling based on protein sequence, three-dimensional structure, and protein titration curves. In nearly all cases, the primary sequence of a protein of interest is available; in many instances high-resolution protein structures exist, and can be taken with minimal modification from the RCSB Protein Data Bank (http://www.rcsb.org). The atomic coordinates of such proteins are usually obtained from either X-ray diffraction, or from 2D-NMR; when no such information is available, protein structures can be constructed via homology modeling, assuming that an adequate level of sequence homology exists between the template and the protein whose structure is being modeled. Knowing the location of each titratable side-chain allows for assignment of amino acid charges on the basis the degree of dissociation of a particular residue.

This degree of dissociation (α) of a particular amino acid is generated using a method based on the spherical-smeared-charge model proposed by Charles Tanford[4] via iterative refinement of protein charge curves (Figure 1.4), where such curves are obtained directly from potentiometric titration. Such experiments allow for the charge state on a titratable macromolecule to be obtained directly from the volume difference between blank and experimental solutions, so long as titrants of precisely known molarity are used.

Using this smeared-charge model, the role of pH on perturbing α can be described by an empirical electrostatic interaction parameter, *w*, the effect of which is controlled by total protein charge, Z:

$$\alpha(pH) = 10^{(pH-pK+0.868\times w\times Z)}/(1+10^{(pH-pK+0.868\times w\times Z)}) \quad \textbf{(1.3)}$$

This expression allows for consideration of electrostatic repulsion among charged amino acids, often resulting in perturbation of the intrinsic pK of a particular amino acid, an effect that is amplified when the ionizable group is within a protein charge domain (Figure 1.1).

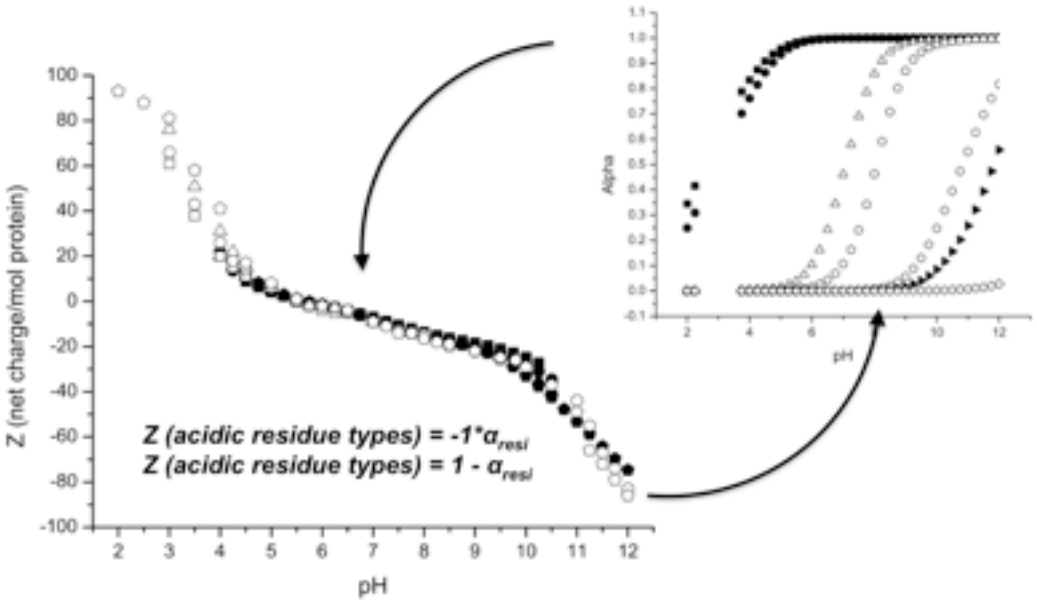

Figure 1.4: Total protein charge is calculated by summing the degree of dissociation, α, of all acidic and basic amino acids, at a predefined set of pHs.

In order to couple electrostatic modeling with experimental measurements of protein charge, an iterative method is used to extract accurate intrinsic pK values from potentiometric titrations. Charge curves are calculated via the following summation:

$$Ztotal = \Sigma(Z_i^{resi} \times n_i^{resi}) \qquad \textbf{(1.4)}$$

Where Z is the charge of the *i*th amino acid side chain, based on the degree of dissociation (α) calculated at a particular pH, n^{resi}_i is the total number of the *i*th type of

amino acid, and Z^{total} is the sum over all charged groups within a particular protein. A charge curve can be generated by calculating Z^{total} as a function of pH (Figure 1.4); these curves can then be compared directly with experimentally obtained titration curves; each successive iteration represents a new permutation of pK_n and w_n; therefore, this refinement allows us to calculate the degree of dissociation of the *n*th amino acid, α_n, using the experimental pH dependence of Z as input.

1.3 Interest in Understanding Charged Interactions in Native Proteins

Open-ended self-association of compact globular proteins is of great importance in the production, storage, and formulation of many biologically based pharmaceuticals. These issues arise in predicting the stability of so-called classical protein drugs e.g., growth factors, insulin, and insulin analogs at high concentrations.[5, 6, 7] Until recently, the focus on protein conformational diseases[8] has led to a focus on interactions between unfolded, or partially-unfolded, proteins. Denaturing aggregation, controlled by intrinsically short range interactions, is frequently irreversible and highly protein-specific.[9] On the other hand, self-association of natively folded globular proteins[10] can be readily reversed by changing solution conditions (e.g., pH[11] or I[12, 13]). With the increase in production of biologics, specifically focused on production of monoclonal antibodies (mAbs), new issues have arisen with regard to protein stability against aggregation. In order to understand this kind of unwanted self-association behavior, it becomes necessary to consider protein-protein interactions between native proteins. In the case of native protein aggregation, such interactions are between two or more monomers of the same protein.

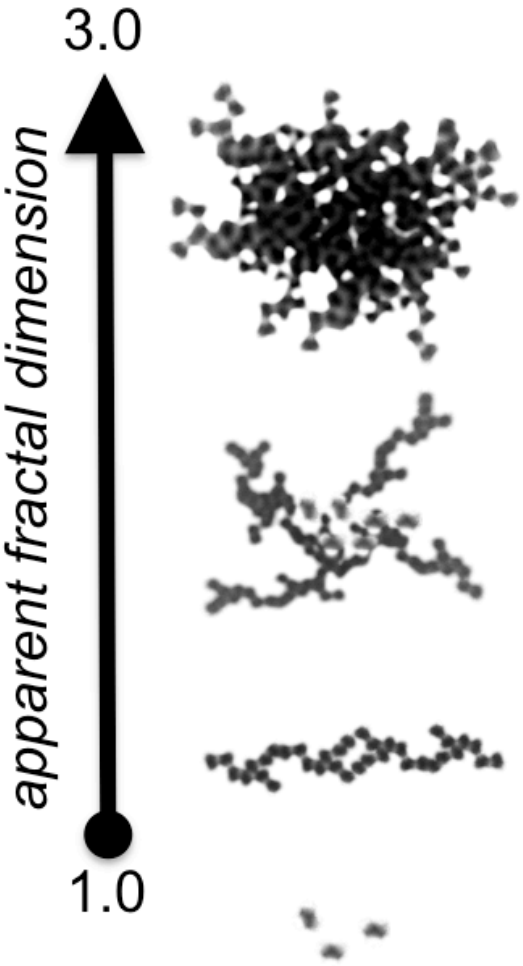

Figure 1.5: Fractal dimensions can be used to determine the density of aggregates assembled from well-defined, colloidal particles.[14]

Any attempt to correlate electrostatic effects with protein charge anisotropy, in the context of the kinetics of protein aggregation must account for the mechanism of aggregation.[15] Consumption of free monomeric protein via addition to preformed protein aggregates should be controlled by the structure of such aggregates.[16] Comparison of such structures to those described by simple colloidal models (i.e., diffusion or reaction - limited aggregation processes) can reveal information about the mechanism of self-association (Figure 1.5). Equilibrium solution behavior is typically seen at high salt, $I \geq 0.15$ M where

electrostatic interactions are largely screened at all but short protein-protein separation distances, and at pH far from protein pI where the attractive force responsible for kinetically controlled aggregation of native protein is typically minimized.

Turbidimetric measurements[17, 18, 19] are often used to relate aggregation kinetics to pH dependent solution behavior, using pH titrations. Such measurements are made on largely transparent solutions, where the "turbidity" being measured is in fact derived from a measurement of transmittance, measurable up to ±1 ppt. These turbidimetric titrations are sensitive to very small changes in the intensity of scattered light, measured as the % of transmitted light lost to scattering at all non-zero scattering angles. In such experiments, turbidity is expressed as 100 - %T, which is linear with classical turbidity τ in the limit of low turbidity. These titrations are capable of detecting small increases in τ resulting from increase in aggregation number (monomer, dimer, etc.) and also complexation, as well as gross increases in turbidity due to aggregation, phase separation, and droplet formation. The later phenomenon are frequently seen in systems involving either heteroprotein interactions or protein-PE interactions.

1.4 Hydrated Protein Surfaces Mediate Numerous Intermolecular Interactions

Interactions between proteins and other macromolecules can be described in terms of attractive electrostatics; since such electrostatic interactions are on the order of kT, it is unlikely that such associations would result in desolvation; thus it is reasonable to consider such intermolecular attractions as being mediated by hydrated protein surfaces.

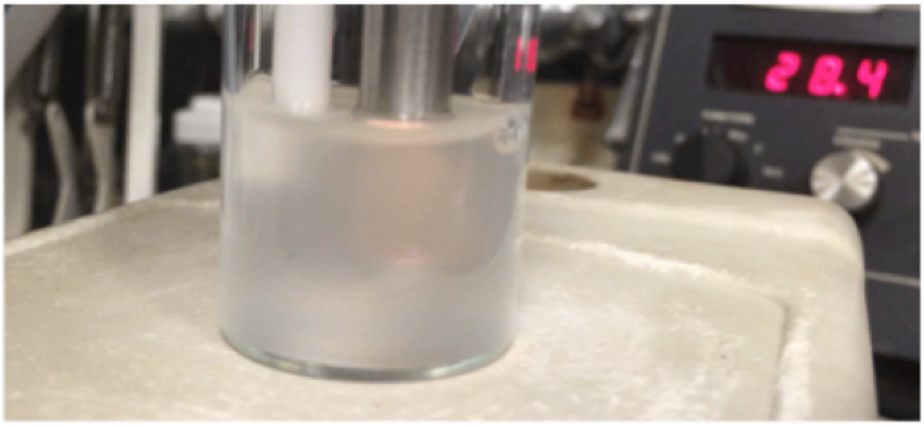

Figure 1.6: Typical grainy appearance of a suspension of coacervate droplets, as seen *during* a turbidimetric titration. Note graininess is due to the presence of stable droplets with a unique set of refractive indices, and of a characteristic size.

These types of interactions can include a single protein interacting with a range of "binding partners", including (1) protein-protein interactions, (2) protein-polymer interactions, and (3) protein-surface interactions. Protein-protein interactions can be divided into two types: self-interaction, where two monomers of the same protein interact, as is the case with either multimerization or aggregation; or interactions where two *different* proteins associate, such as is seen with heteroprotein coacervation. The second case, protein-PE interactions, where a compact electrostatically complex binding partner has been replaced by a flexible polymer of high (but uniform) charge density, has been shown to result in formation of either soluble complexes, or in the case of protein-PE coacervation, liquid-liquid phase separation (LLPS). In all cases it is the hydrated protein that is key to such interactions.

1.5 Complex Coacervation

Complex coacervation is a unique form of LLPS that results from non-specific attractive electrostatic interactions between oppositely charged macromolecules;[20] such coacervates (Figure 1.6) can be prepared from a number of precursors. Self-association of globular

proteins can in some cases result in equilibrium controlled LLPS, although it is not clear to what extent this is analogous to coacervation, as there is a single precursor protein. The case for two different proteins, referred to as heteroprotein coacervation, occurs under a very narrow range of solution conditions, even when the proteins remain oppositely charged over a wide range of pHs and *I*s. When one of the proteins is replaced by a flexible polyelectrolyte, coacervation can occur over a much wider range of conditions, and interactions often begin at pHs where the protein and PE are of like charge, pH > pI for polyanions *or* pH < pI for polycations, such cases termed "binding on the wrong side of pI".

Interactions with surfaces such as chromatography packing particles, while also equilibrium controlled, and in many cases also involving patchy interactions between particles and proteins of like-charge, are likely too different in form from the above cases to be effectively compared to coacervating systems, although the formation of soluble complexes may be a useful analogy in this case.

1.6 Overview

Protein self-interaction can result in a type of LLPS with features similar to coacervation, but over a much less specific set of conditions. Heteroprotein-interactions introduce a level of geometric constraint that is reflected in a highly constrained set of conditions for heteroprotein coacervation. Protein-PE coacervates can be formed under a much more extended set of solution conditions, possible due to the flexibility of the PE chain; and finally, non-ideal interactions in chromatography may involve attractive electrostatic interactions, involving protein charge patches, analogous to those seen in coacervating systems.

CHAPTER 2

pH-DEPENDENT AGGREGATION AND DISAGGREGATION OF NATIVE β-LACTOGLOBULIN IN LOW SALT

Yunfeng Yan, Daniel Seeman,* Bingqian Zheng, Ebru Kizilay, Yisheng Xu, and Paul L. Dubin * *Langmuir*, **2013**, *29* (14), pp 4584–4593

*corresponding author

2.1 Abstract

The aggregation of β-lactoglobulin (BLG) near its isoelectric point was studied as a function of ionic strength and pH. We compared the behavior of native BLG with those of its two isoforms, BLG-A and BLG-B, and with that of a protein with a very similar pI, bovine serum albumin (BSA). Rates of aggregation were obtained through a highly precise and convenient pH/turbidimetric titration that measures transmittance to ±0.05 %T. A comparison of BLG and BSA suggests that the difference between pH_{max} (the pH of the maximum aggregation rate) and pI is systematically related to the nature of protein charge asymmetry, as further supported by the effect of localized charge density on the dramatically different aggregation rates of the two BLG isoforms. Kinetic measurements including very short time periods show well-differentiated aggregation steps. BLG was analyzed by light scattering under conditions corresponding to maxima in the first and second steps. Dynamic light scattering (DLS) was used to monitor the kinetics, and static light scattering (SLS) was used to evaluate the aggregate structure fractal dimensions at different quench points. The rate of the first step is relatively symmetrical around pH_{max} and is attributed to the local charges within the negative domain of the free protein. In contrast, the remarkably linear pH dependence of the second step is related to the uniform reduction in global protein charge

with increasing pH below pI, accompanied by an attractive force due to surface charge fluctuations.

2.2 Introduction

The aggregation of proteins in their native state, an effect predominant at low ionic strength and pH near pI, is a reflection of their surface properties, in particular, the distribution of charged domains. In contrast to unfolding aggregation, native state aggregation involves interactions among hydrated protein surfaces. Without the exposure of solvophobic groups, the aggregation rate does not depend on the kinetics of an array of transient intermediates and exhibits a higher degree of reversibility. To the extent that the limited states involved in the aggregation process are well defined, the aggregation kinetics can be analyzed from the perspective of energetics. Surface charges and their distributions then become the focus of interprotein and interparticle interactions. The diminished role of primary structure means that the aggregation of folded proteins is less protein-specific, and predictive rules based on protein tertiary structure and charge anisotropy are possible.

The association of folded proteins is of considerable importance for pharmaceutical formulation stability[5, 6, 7] and is likely to influence subsequent behavior under more extreme conditions. However, current concerns about protein conformational diseases[8] have led to a focus on the irreversible association of unfolded precursors. Unfolding aggregation requires the disruption of secondary or tertiary structure and therefore the disturbance of the numerous hydrophobic and hydrogen-bonding interactions that stabilize the native state. Proteins with various primary structures show different aggregation mechanisms, manifested in a variety of intermediates, aggregate structures, and critical temperatures. Because

different regions of the protein surface become exposed and engaged in short-range interactions, unfolding aggregation can be irreversible and the mechanisms can also be highly protein-specific.[9] The corresponding numerous forms of denaturing aggregation have led to several attempts at aggregation classification – with some referring to the mechanism and some referring to the size, morphology, and reversibility of aggregates.[8] However, no general rules can be proposed to relate the sequence arrangement to the unfolding aggregation behavior, which is often observed to occur irreversibly, particularly under extreme conditions.

The characteristic reversibility of aggregation in the native state arises from the absence of high-energy unfolded intermediates subject to a new set of short-range interactions.[10] For intrinsically reversible native state aggregation,[11] the interactions involved can be better understood as involving only the hydrated protein surface.[21] Interprotein interactions may be resolved into enthalpic and entropic contributions,[22] in a way almost impossible when subject to ongoing protein conformational changes.[22] The fact that native state aggregation, isoelectric precipitation, is suppressed by salt reveals the electrostatic origin of these contributions and suggests considerations of protein charge anisotropy.[12, 13] Protein charge anisotropy is characterized by an asymmetric distribution of charge domains on a protein such that there are similar magnitude repulsive and attractive interactions present between like-charged proteins near the pI. Such charge patches are necessary to explain instances of attractive interactions between proteins and PEs observed on the "wrong side" of the isoelectric point for which neither net charge nor highly short-range interactions would provide an adequate explanation.[23]

Electrostatic interactions among native proteins govern both the aggregation process

and the structure of the final aggregate. When self-association involves electrostatic interactions, their long-range nature means that spatial separation, the first step of disaggregation, can be accomplished through changes in pH and ionic strength without exposure of hydrophobic residues. Resolvation, screening by small ions, or repulsive forces arising from changes in pH then compensates for the loss of interprotein attractive forces. Those pairwise interactions can be defined at specified conditions of pH, ionic strength, and temperature.[24] Resolution into enthalpic and entropic contributions[25] is possible when the initial and final states are well-defined and kinetics do not dominate. Modeling can then help to predict the geometry of multimers and to resolve equilibrium association constants for cognate protein–protein interactions into k_{on} and k_{off}.[26, 27] Because protein–protein interactions involve solvent-accessible surfaces, protein charge anisotropy is often a contributing factor.[1, 2]

The role of charge anisotropy in native state aggregation is revealed by the tendency of proteins to become insoluble at pH near the isoelectric point.[28] Because the net charge is near zero, electrostatic attractions can come only from charge asymmetry that can be visualized by computational methods based on protein structure (from the RCSB Protein Data Bank) and protein charge curves.[23] However, the correlation of protein charge with aggregation kinetics must take into account the mechanism of aggregation and deal with simultaneous equilibrium and kinetic behavior where subsequent steps governed by transient intermediates may be rate-determining.[15] Clustering or later-stage monomer consumption can be influenced by the structure of aggregates, the assembly of which is conveniently described by fractal dimensions.[16] In addition, later stages of aggregation prior to irreversible association can be subject to hysteresis because competing disaggregation may proceed by a

different pathway.[29, 30] Nevertheless, strong evidence of correlations between the protein surface charge state and native state aggregation rates prior to loss of solubility has been gleaned from turbidimetric measurements.[31, 32, 33] β-lactoglobulin (BLG) with two isoforms that differ with respect to a charge patch should provide an example of such behavior.[31]

The aggregation of BLG has probably been studied more than that of any other protein. The great majority of these studies have involved denaturing conditions[34, 35] (e.g., extremes in pH or temperature because of their relevance to food and dairy processing[36, 37]). The heat-induced aggregation of BLG is sometimes used as a general model for fibril formation,[38, 39] a process that is implicated in neurodegenerative diseases.[40] Although many papers on denaturing aggregation focus on kinetics,[41, 42] studies of the native state aggregation of BLG mainly deal with the equilibrium association of multimers or oligomers. Major findings include (1) the formation of dimers in equilibrium with monomers at $3 < \text{pH} < 9$[43, 44, 45, 46] enhanced by increasing ionic strength I[46, 47, 48, 49] and (2) the formation of higher-order multimers at pH 4 to 5, which for the case of an octamer[48, 50, 51, 52] shows an opposite ionic strength dependence, shifting toward the dimer with added salt, but other reports suggest that the tetramer and hexamer could coexist.[53] Such equilibrium behavior seems to be typical for BLG at $I \geq 0.1$ M at pH far from its pI, where open-ended aggregation is avoided, although the distinction between multimerization and aggregation becomes less clear when the products of the association are small (e.g., clusters containing relatively small numbers of proteins[54]).

Kinetically controlled aggregation of BLG in the native state is typical at $I < 0.01$ M, especially at pH near pI. Kumosins et al.[53] concluded from sedimentation kinetics that the aggregation of BLG is the sum of three possible interactions, namely, A–A and B–B self-

interactions and A–B interactions. Timasheff and Townend[55] expanded on this, concluding that the aggregation of BLG is due primarily to a single isoform, namely, BLG-A. Majhi et al.[31] found two processes: an initial fast consumption of the BLG dimer to form an aggregate of intermediate size, followed by slow growth of the aggregates. The maximum aggregation rate occurred near pH 4.6, below the pI of 5.2, and the pH dependence of the initial aggregation rate was highly asymmetric. At pH 5.0, the initial rate increased with $1/I$. This open-ended aggregation at pH ≠ pI was attributed to the charge anisotropy of native BLG that was visualized by computer modeling. Such visualization was used to explain the dramatic effect on the aggregation rate when residues in BLG-B (Gly64, Ala118) are replaced in BLG-A (Asp64, Val118). However, the nature of the proposed two-step mechanism was not clearly elucidated, and little attention was paid to the role of pH-dependent disaggregation.

Here we consider the mechanism of pH-induced BLG native state aggregation in the vicinity of pI, with particular attention to two factors not previously examined: (1) the strong effect of the direction of pH adjustment on both aggregation and disaggregation kinetics, and (2) the nature of the two characteristic rate processes and their relationships to net versus local protein charge.[48, 51] We used turbidimetric pH titrations as a convenient and effective method for measuring aggregation rates as a function of pH and the time dependence of turbidity to resolve and quantitate pH effects on the two rates. Dynamic light scattering (DLS) was used to evaluate the kinetics in terms of hydrodynamic diameters and scattering intensity under conditions where the two steps are easily resolved as revealed from titration experiments. Static light scattering (SLS) was employed to evaluate the fractal structure of quenched aggregates at two pH values corresponding to maximum values of the two rates.

Electrostatic protein modeling was employed to support two distinct molecular descriptions for these processes. Finally, we show the broad and general significance of these approaches with reference to BSA as an example of protein with charge anisotropy distinct from that of BLG.

2.3 Experimental Section

Materials. Native bovine β-lactoglobulin (BLG, 18 kDa, pI = 5.2) was a gift from C. Schmitt (Nestlé, Lausanne; >97%, batch number JE 001-8-415, 55.4% BLG-A and 41.6% BLG-B). Isoforms of BLG (BLG-A and BLG-B) were from Sigma-Aldrich (lot nos. 097K7010 and 048K7003 V, respectively). Fatty acid-free bovine serum albumin fraction V (BSA, 68 kDa, pI = 4.9, >99%) was Calbiochem lot D00096763. NaCl and standard NaOH and HCl solutions were purchased from Fisher Scientific. Milli-Q water was used in all sample preparation.

Turbidimetric Methods. Turbidimetric titrations were performed by the addition of either 0.1 N NaOH (forward titration) or 0.1 N HCl (backward titration) to a 15 mL protein solution with stirring and the simultaneous monitoring of pH and transmittance at 25 °C. It is conventional to report turbidity (τ) as 100 – %T, a unitless quantity that is linear with turbidity over a certain range of transmittance. It is convenient to describe it in this form because it absorbs terms such as the extinction coefficient, which would otherwise be poorly defined for such systems. The rate of pH change was kept at 0.2 pH units/min in all titrations except for the experiments in Figure 2.11. For kinetic experiments, protein solutions were prepared at pH 9 and brought to the desired pH by the addition of 0.1 N HCl in 15 s. The transmittance of protein solutions was measured using a Brinkmann PC 800 colorimeter

equipped with a 420 nm filter and a 1 cm path length fiber optic probe, calibrated to 100% transmittance with Milli-Q water. Instrument drift during a single measurement was less than 0.05 %T after a 30 min warm-up. pH was measured with a Corning 240 pH meter. Samples were filtered with a 0.22 μm membrane (Millipore) before titration. With this technique, turbidity measurements are precise to ±2 ppt and highly robust, with repeatability demonstrated by the precise reproduction of the *I* dependence of BLG aggregation rates previously measured[31] (Figure 2.13).

Dynamic Light Scattering (DLS). DLS was carried out at 25.0 °C with a Malvern Zetasizer Nano ZS instrument equipped for backscattering at 173° with a 633 nm He–Ne laser. Protein solutions were adjusted rapidly from a nonaggregating pH 7.0 to pH 4.9 or 5.1. DLS measurements were started within 30 s of the pH adjustment. The distributions of the mean apparent translational diffusion coefficients (D_T) were determined by fitting the DLS autocorrelation functions using non-negative constrained least-squares (NNLS). The robustness of this algorithm vis-à-vis CONTIN has been amply demonstrated, even for systems with more than two decay modes. The distribution of the apparent hydrodynamic radii (R_{app}) was obtained from the distribution of mean apparent translational diffusion coefficients (D_T) via

$$R_{app} = kT/6\pi\eta D_T \qquad (2.1)$$

where k is the Boltzmann constant, T is the absolute temperature, and η is the solvent viscosity, which was assumed to be that of water.

Static Light Scattering (SLS). SLS experiments were performed using a BI-200 SM goniometer and BIC-2030D photon counting system (Brookhaven Instruments Inc.) with an

Omnichrome Ar ion laser (100 mW, λ = 488 nm) at ambient temperature, ~25 °C. The scattering intensity was measured as a function of scattering angle between 75 and 120°. Fractal dimensions (D_f) were extracted from angle dependence in the high-q limit via linearization[56] of the scattering data using the relation

$$I(q) \propto q^{-Df} \quad (2.2)$$

where $I(q)$ is the scattering intensity and the scattering vector q is $(4\pi n/\lambda)\sin(\theta/2)$, with n the refractive index of the fluid, λ the wavelength, and θ the scattering angle. BLG aggregation in 0.01 M NaCl was initiated by pH adjustment from 7.0 to either 4.9 or 5.1 and sustained for 5–20 min. Aggregation was quenched by rapid adjustment from the aggregating pH to pH 4.4, at which point the aggregate size was found by DLS to no longer change with time. Each SLS measurement was made in replicate over the course of 2 h to ensure that quenched samples were invariant with respect to time.

Computational Methods. DelPhi[3] V. 4r1.1 was used to model the electrostatic potential around the protein as a function of pH and ionic strength. PDB 3V03 (BSA monomer) and 1BEB (BLG dimer) were taken from the RCSB Protein Data Bank (http://www.rcsb.org). The amino acid charges were generated using the spherical-smeared-charge model proposed by Tanford on the basis of titration curves of BLG and BSA.[4]

2.4 Results

2.4.1 Turbidimetric pH Titrations

The increase in turbidity upon addition of acid or base, as shown for the curve of larger magnitude in Figure 2.1A, summarizes the accumulation of soluble aggregates and

their subsequent redissolution with diminishing pH. Even at fixed protein concentration and ionic strength, the turbidity, as a kinetic variable, is sensitive to the elapsed time between titrant increments, which is presumably responsible for deviations in absolute turbidity among duplicate runs; this did not exceed 15% (relative). However, the pH corresponding to the maximum change in turbidity $(d\tau/dt)_{max}$ did not vary. The rate of titrant addition was controlled to ensure that dpH/dt is constant; consequently, the instantaneous rate of aggregation at any pH ($(d\tau/dt)_{pH}$) is given by (dτ/dpH)(dpH/dt). Hence, the plot in Figure 2.1B essentially describes the pH dependence of the instantaneous rate of aggregation. As will be shown below, $(d\tau/dt)_{pH}$ obtained in this way is remarkably similar to $(d\tau/dt)_{t=0}$ at fixed pH so that the inflection points indicated by the vertical dashed lines are the pHs of the maximum aggregation rate. It is of interest to note the crossing point of the two curves in Figure 2.1A, which correspond closely to the identical pH positions of the maxima in Figure 2.1B. The absence of any effect of the titration direction on the rate at this point suggests that the process is controlled by free protein and not prior aggregates. Furthermore, the pH values at the turbidity maxima can be directly confirmed as conditions of constant turbidity (Figure 2.12 in the Supporting Information). The magnitude of accumulated aggregate τ_{max} clearly depends on the direction of titration (Figure 2.1A). This may indicate differences in aggregate structure, which also would lead to differences in disaggregation. However, regardless of the titration *direction*, the curves cross at the inflection point (see also dτ/dpH in Figure 2.1B): the maximum aggregation rate occurs at the same pH.

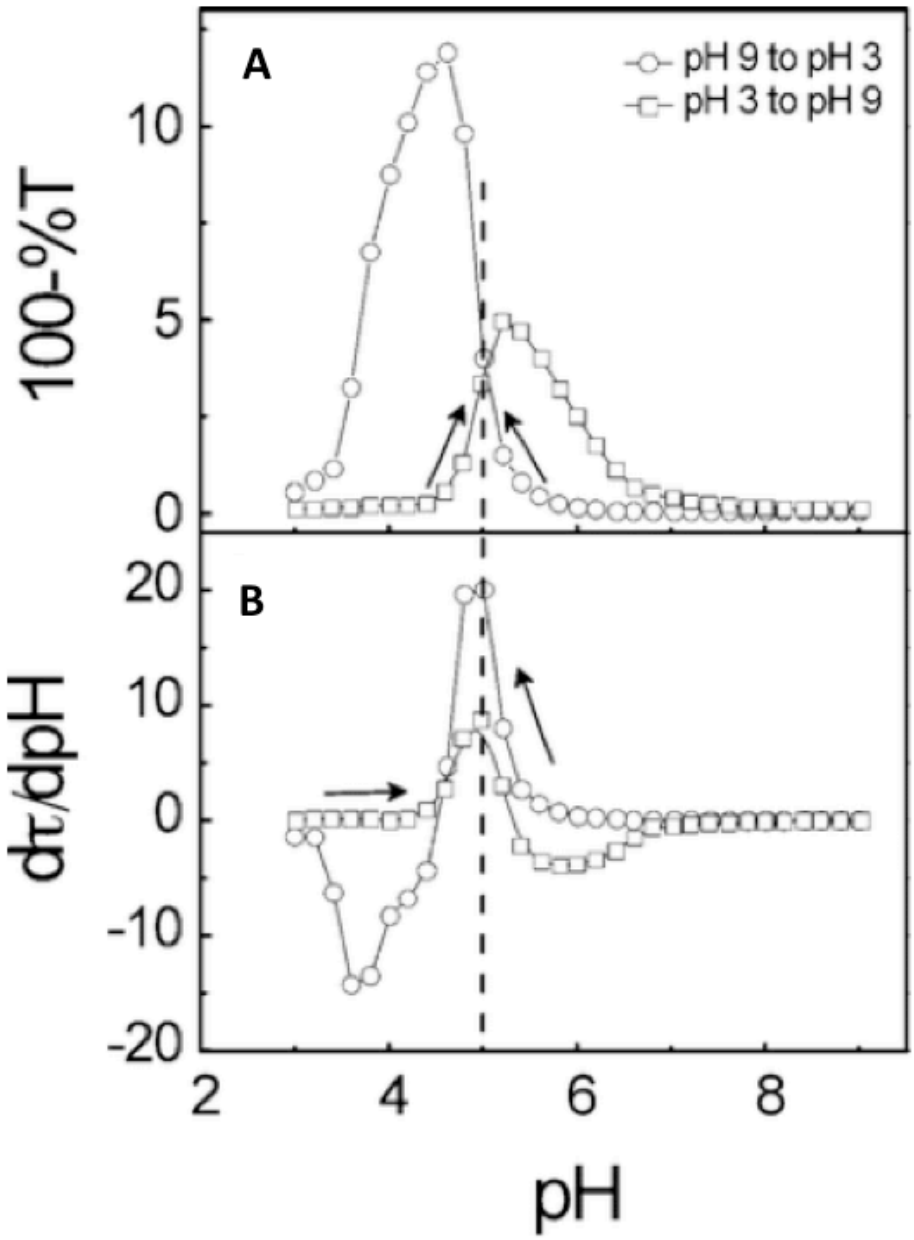

Figure 2.1: (A) Type 1 titrations of 1.0 g/L BLG in 0.0045 M NaCl. **(B)** dτ/dpH vs pH. The rate of addition of HCl or NaOH was 0.2 pH unit/min. The titration directions indicated by arrows are (□) low to high pH and (○) high to low pH. The vertical dashed line corresponds to the inflection points (maximum aggregation rates) for both directions. −dτ/dpH is shown for pH 9 → 3 to adjust for the trivially negative values of dpH: negative values in **(B)** correspond to disaggregation.

To demonstrate the utility of turbidimetric pH titrations, we carried out titrations with acid at ionic strengths *I* ranging from 0.0045 to 0.1 M (NaCl). The ionic strength dependence

of the inflection points $(d\tau/dpH)_{max}$ showed nearly the same I^{-1} dependence (Figure 2.13) as seen previously for the initial rate at fixed pH $(d\tau/dt)_0$.[31] As expected, the maximum turbidity depended on the rate of titration, increasing ca. 40% with a 3-fold decrease in (dpH/d*t*), but the characteristic pHs of τ_{max} and $(d\tau/dt)_{max}$ (figure 2.11) were independent of (dpH/d*t*). The pH titrations thus yield, more conveniently, very similar results to the more laborious time-dependent studies at fixed pH.

2.4.2 Identification of Two Steps

The extent of aggregation of BLG increases with pH from 4.4 to 4.8 and decreases as the pH increases from 5.1 to 5.7 (Figure 2.2), but the pH dependence of the amount of aggregate is seen to be mainly determined in the first ca. 10 min. In other words, a fast initial step is followed by a slow second step. The pH dependences of the aggregation rates for the fast initial step (t < 10 min) and the following slow step (45 < t < 90 min) are reported as $(d\tau/dt)_0$ and $(d\tau/dt)_2$ in Figure 2.3A and B, respectively. The pH dependence of $(d\tau/dt)_0$ is symmetric around a maximum at pH 4.9 (i.e., below pI = 5.2). In contrast, $(d\tau/dt)_2$, typically ca. 25 times smaller than $(d\tau/dt)_0$, is remarkably linear with pH, attaining a maximum at pI. In addition, the two steps show different ionic strength dependences (i.e., the aggregation rate is linear with I^{-1} for the initial step and with $I^{-0.25}$ for the second step (Figure 2.4)). The implications regarding the different mechanisms and the respective roles of protein charge anisotropy in the two steps will be discussed below.

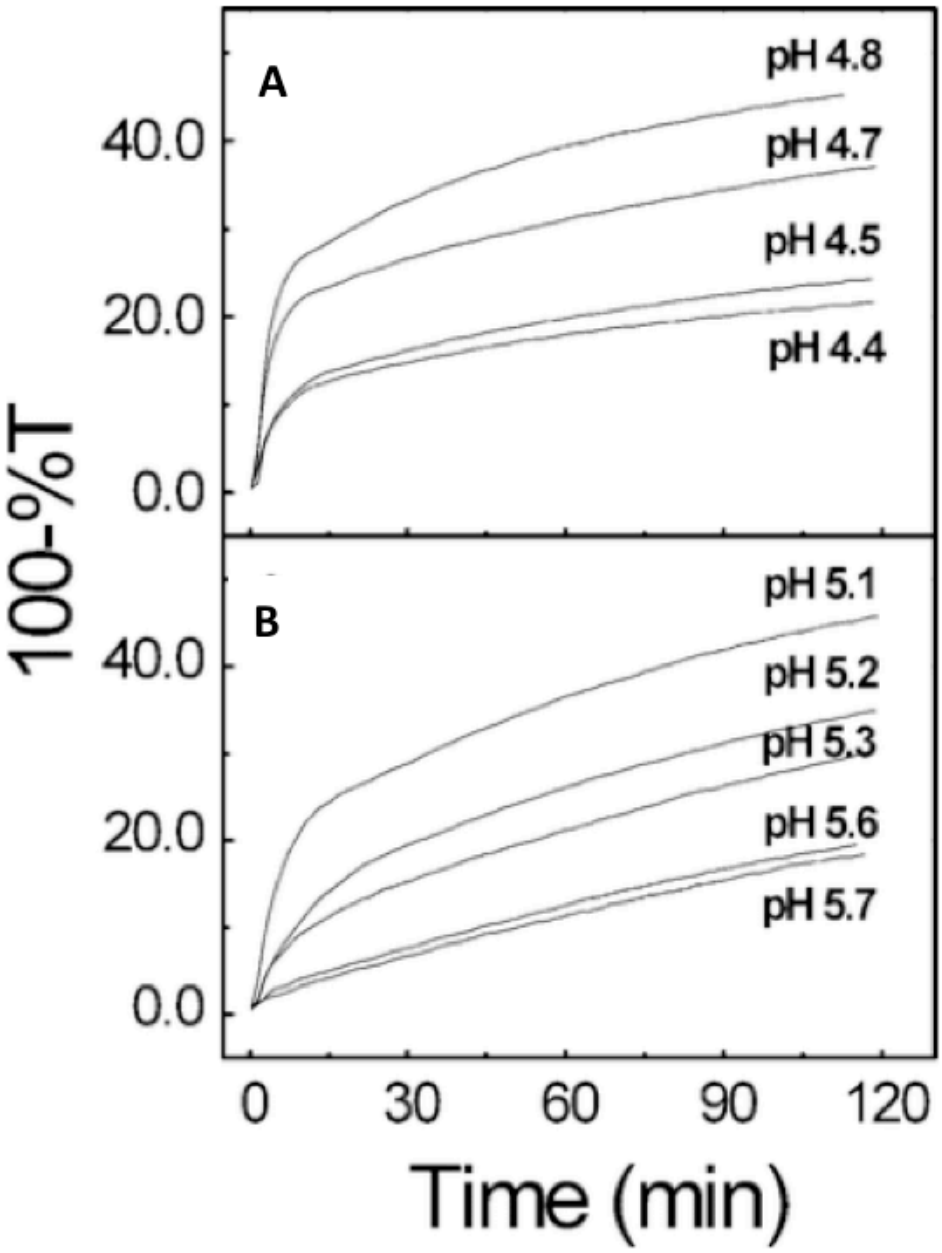

Figure 2.2: Turbidity vs time for 1.0 g/L BLG (1.3:1 A/B), I = 0.0045 M **(A)** pH 4.4–4.8 and **(B)** pH 5.1–5.7.

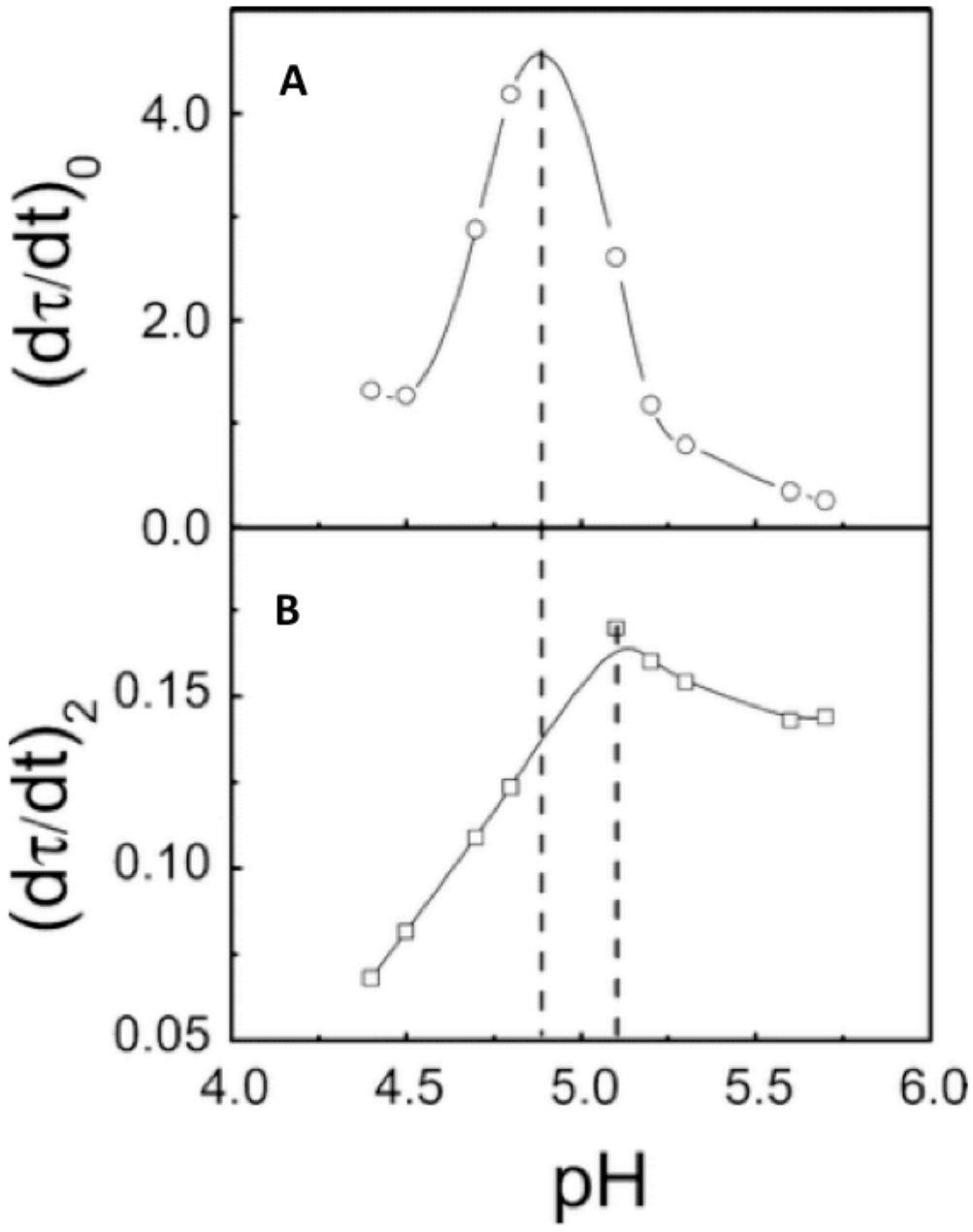

Figure 2.3: Aggregation rate ($d\tau/dt$) vs pH from Figure 2.2. **(A)** Initial rate $(d\tau/dt)_0$ and **(B)** aggregation rate for the second step $(d\tau/dt)_2$. The vertical dashed lines denote the pHs for the maxima of $(d\tau/dt)_0$ and $(d\tau/dt)_2$. Note the different scales for plots ***A*** and ***B*** showing the dominant effect of the initial rate.

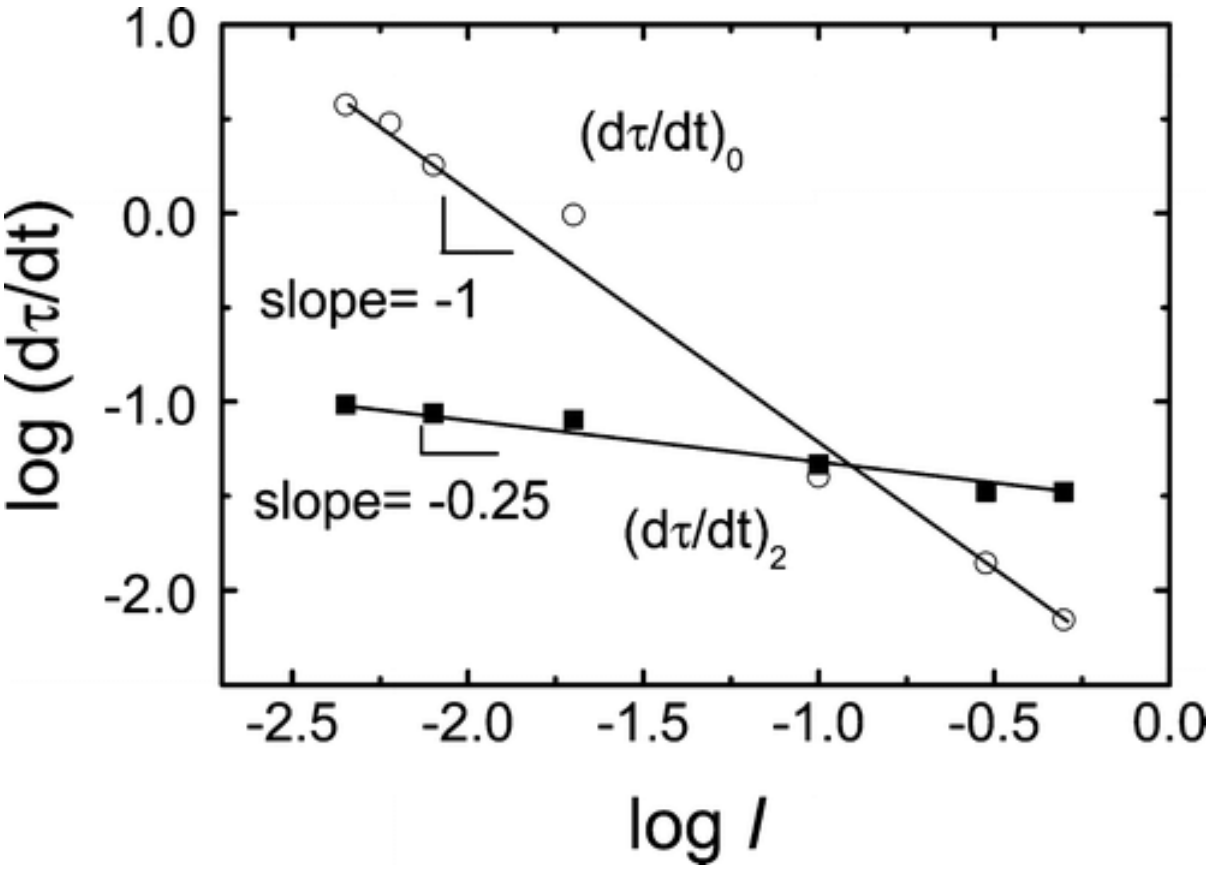

Figure 2.4: Logarithmic plot of dτ/dt and I (open symbols for the initial rate, filled symbols for the second step) at pH 5.0. The slopes are −1 and −0.25 for $(d\tau/dt)_0$ and $(d\tau/dt)_2$, respectively. Data are reproduced from a previous paper.[31]

2.4.3 Structure of BLG Aggregates

Dynamic light scattering (DLS) was used to study the aggregation of 1.0 g/L BLG at pH 4.9 and 5.1, conditions that correspond to the apparent aggregation rate maxima in the initial and second steps, respectively. At pH 4.9, where the initial rate dominates, hydrodynamic diameters (Figure 2.5A) grow to over a micrometer in t < 10 min, during which time the scattering intensity increases dramatically (Figure 2.5C). In contrast, at pH 5.1, a gradual increase in size is observed (Figure 2.5B) along with an almost negligible increase in scattering intensity (Figure 2.5D). The increase in diameters seen at pH 4.9 at short time together with the relatively smaller effect at pH 5.1 suggests that the initial rate is

controlled by the formation of nuclei, and the second step involves the growth of preformed nuclei. Notably absent is any evidence of species of intermediate size, indicating that aggregates are formed from BLG dimers (possibly in equilibrium with monomers) with no involvement of multimers such as tetramers and hexamers.

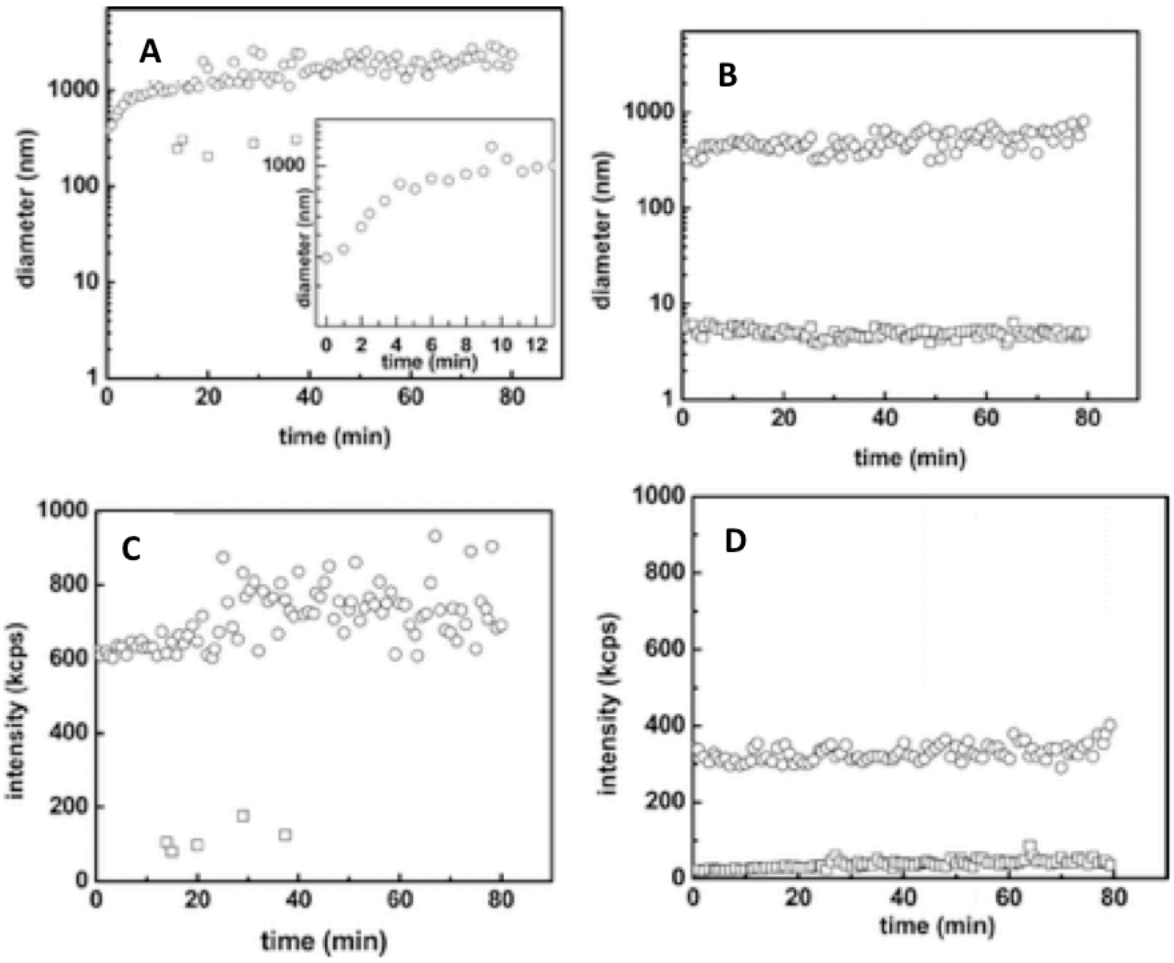

Figure 2.5: DLS kinetics of 1.0 g/L BLG in I = 0.01 M at **(A, C)** pH 4.9 and **(B, D)** pH 5.1. (○) Slow mode and (□) fast mode obtained from the intensity-weighted distribution of apparent diameters. The inset in plot ***A*** is an expansion of the first 13 min.

The apparent quenching of aggregate growth (Figures 2.1B and 12) arises from a balance of aggregation and disaggregation rates at a particular pH (i.e., 4.4). Adjustment

from aggregating conditions (pH 4.9 or 5.1) to this quenching condition halts the growth of protein aggregates. SLS results under these two conditions are shown in Figure 2.6. Fractal dimensions, a power law describing the distribution of mass or scattering centers within an aggregate, were measured for each quenched sample.

SLS results for the sample quenched from pH 4.9 (Figure 2.6A) where step one is maximal show that the apparent D_f of BLG aggregates increases continuously before finally converging to a limiting value of 3.0, which is consistent with a fully compact structure. At pH 5.1 (Figure 2.6B), the increase in fractal dimension is comparable but a lower limiting value is reached, indicating that these aggregates remain somewhat fractal in nature even at t = 20 min (Figure 2.6C). The D_f increases slowly during the first ~10 min, a lag time displayed at both pHs. In this first step the structures formed are loose, allowing for the rapid packing of free BLG into the aggregate. The values of D_f would seem to preclude both classical diffusion- and reaction-limited cluster–cluster aggregation[14] but are consistent with an initial nucleation step represented by diffusion-limited particle–cluster aggregation.[14] By the final quench point, aggregates are no longer fractal in nature, possibly explained by a switch to reaction-limited particle cluster aggregation[14] in which the close packing of free protein results in a nearly homogeneous structure. At pH 5.1, such nucleation occurs more slowly, leading to a smaller observed fractal dimension at the final quench point.

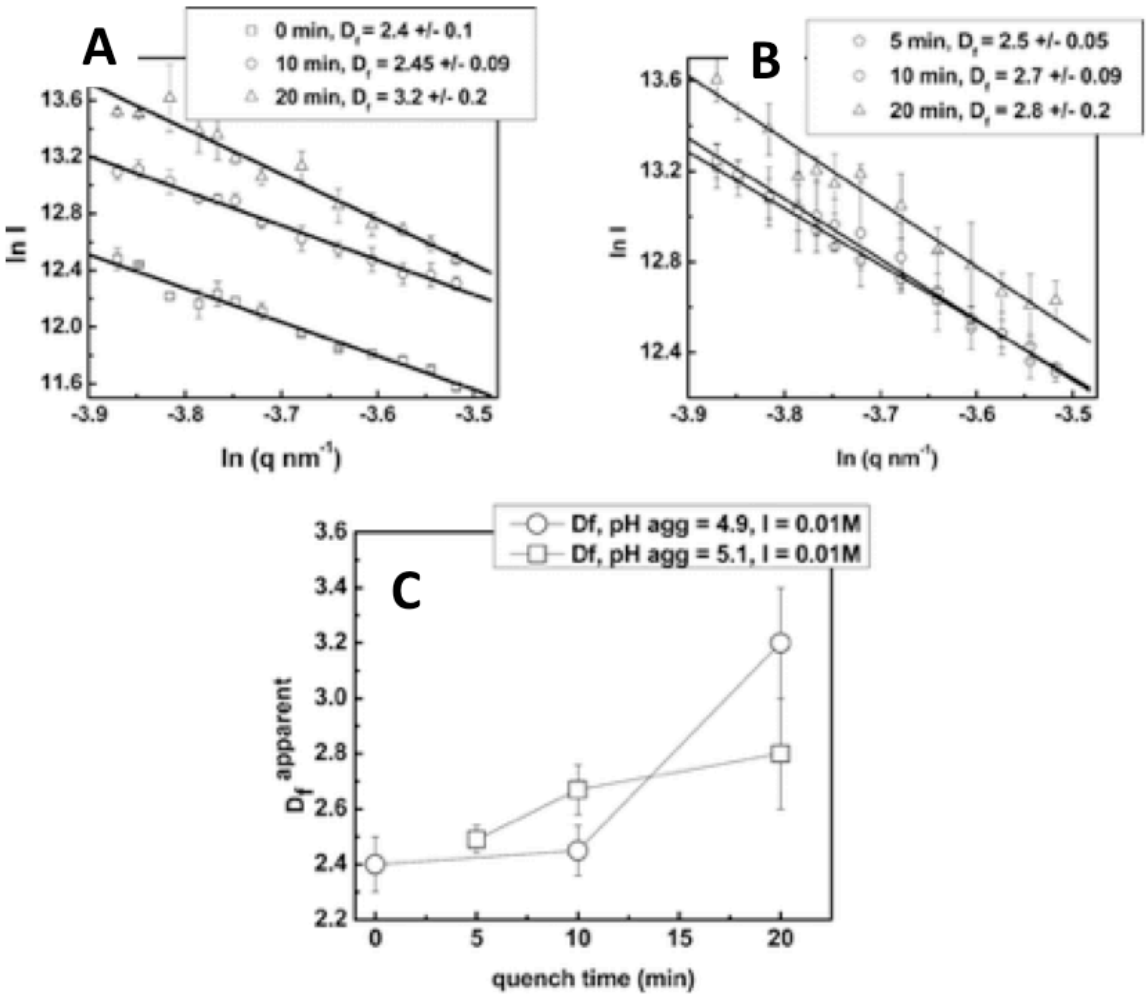

Figure 2.6: SLS of 1 g/L BLG in I = 0.01 M quenched by adjustment to pH 4.4 after a fixed amount of time. BLG aggregation is induced at **(A)** pH 4.9 and **(B)** pH 5.1. **(C)** Apparent D_f as a function of quench time.

In the absence of intermediate species (e.g., oligomers), the increase in turbidity must be attributed to the formation of aggregates that grow in size and decrease in number. With appropriate assumptions about their density, based on fractal dimensions, it is possible to estimate that the number of dimers per aggregate increases from roughly 2×10^4 to 5×10^6 over the first 20 min, with a concomitant 250-fold decrease in the number of aggregates. The present results do not indicate whether this occurs by aggregate fusion or dimer consumption,

which is the subject of an ongoing size exclusion study.

2.4.4 Aggregation of BLG Isoforms

The marked difference between the amplitudes of aggregation of BLG variants A and B provides strong evidence of the effect of charge anisotropy that arises from the replacement of uncharged amino acid glycine by aspartic acid in BLG-A, adding two additional negative charges per dimer, as previously noted.[57] Native BLG can be found under dimer dissociation conditions,[31] to contain roughly equal numbers of the A and B monomers, but the distribution among the three possible dimers is not always clear. Mass spectra of Sigma BLG-A prepared at pH 4.5 showed unresolved dimer peaks,[58] but more recently obtained higher-resolution spectra (Figure 2.14) suggest that the AA and BB dimers that predominate in native BLG may dissociate to form the AB heterodimer. This complexity provides additional motivation to examine the aggregation behavior of the homodimers.

Turbidimetric pH titrations of AA and BB are shown in Figure 2.7A,B. Regardless of the direction of titration, aggregation rates are larger by factors of 20–30 for the A dimer. For both titration directions, the aggregation of BLG-A begins only at pH within 0.5 pH unit of the pI. For titration with base, significant disaggregation commences at pH 7.5, and for titration with acid, at pH 3.5. The equivalence of crossing points with points of maximum aggregation rate noted in Figure 2.1 is notably absent in Figure 2.7B because of the large difference in rates. Further comparisons of BLG-B with BLG-A are complicated by the different magnitudes mentioned above.

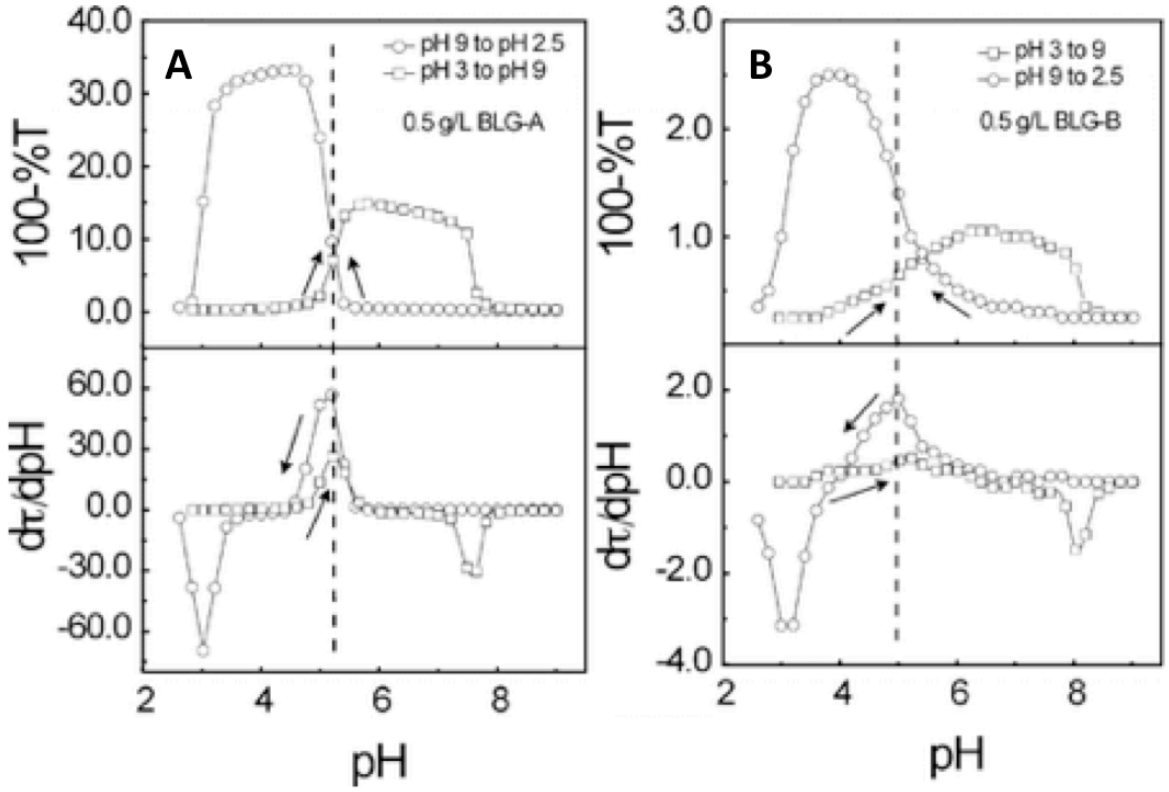

Figure 2.7: Type 1 titrations and dτ/dpH vs pH for **(A)** 0.5 g/L BLG-A and **(B)** 0.5 g/L BLG-B. The rate of addition of HCl or NaOH was 0.2 pH unit/min. The dashed line corresponds to the pH of the maximum aggregation rate, independent of direction. Titration direction: (□) low to high and (○) high to low. I = 0.0045 M. We show −dτ/dpH to adjust for the trivially negative values of dpH for pH 9 → 3 in the lower curves.

2.4.5 Turbidimetric pH Titration of BSA

BLG aggregates most strongly at pH < pI where it is net positive charged because of its negative charge patch.[31] Because BSA, in contrast to BLG, has a positive charge patch,[23] comparative titrations were done with BSA to reinforce this relationship with protein charge anisotropy. The results of this type 1 titration for BSA in Figure 2.8 may be compared to the analogous plot for BLG in Figure 2.1. As is the case for BLG, the pH for the maximum aggregation rate of BSA does not depend on the titration direction, but in contrast to BLG, the pH_{max} for BSA (5.4) is well *above* its pI (4.9).

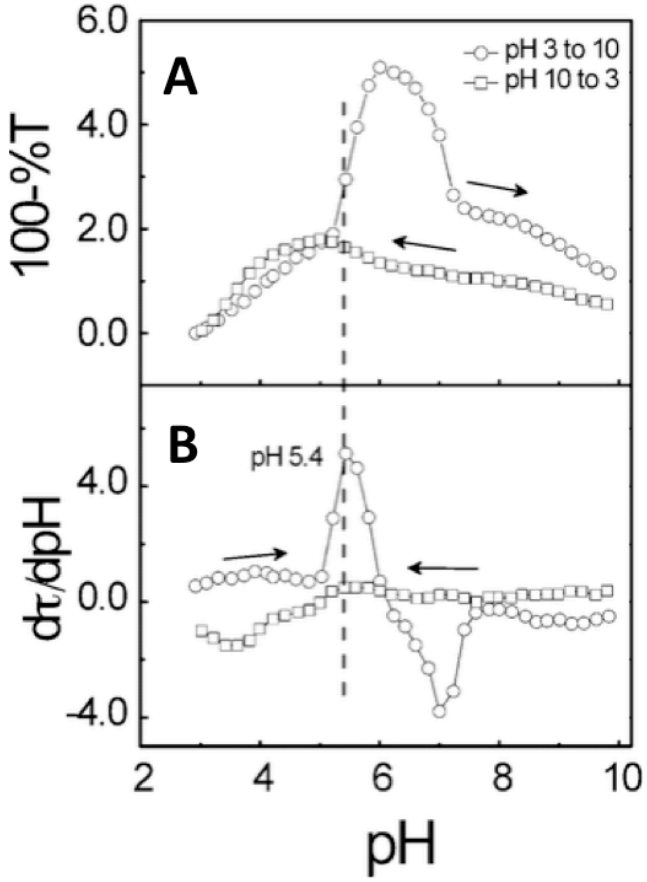

Figure 2.8: (A) Type 1 titrations of 1.0 g/L BSA in 0.0045 M NaCl with NaOH or HCl (arrows). **(B)** dτ/dpH vs pH. The rate of addition of HCl or NaOH was 0.2 pH unit/min. The titration directions indicated by arrows are (○) low to high pH and (□) high to low pH. The vertical dashed line corresponds to the inflection points (maximum aggregation rates) for both titration directions. −dτ/dpH is shown for pH 9 → 3 in plot B to adjust for the trivially negative values of dpH.

2.5 Discussion

2.5.1 Forward and Backward pH Titrations

Turbidimetric pH titration is a convenient method for the study of electrostatically driven native protein aggregation, particularly when the titration rate (dpH/dt) is constant. The instantaneous aggregation rate $(d\tau/dt)_{pH}$ at any pH is then obtained by (dτ/dpH)(dpH/dt). For example, with dpH/dt = 0.2 pH unit/min, we obtain from the acid titration in Figure 2.1B

an aggregation rate of 4.0 %T min^{-1}. The kinetic measurement at pH 4.8 (Figures 2.2 and 2.3) gives the initial rate of $d\tau/dt$ = 4.1 %T min^{-1}. The validation of this method was also confirmed by the ionic strength dependence of the aggregation rate from turbidimetric pH titration at varying *I* (Figure 2.13), similar to previous results. [31] The inflection points in Figure 2.1 correspond to the pHs of the maximum aggregation rate, and the turbidity maxima correspond to pH values at which turbidimetric rates of association and dissociation are equal (Figure 2.12). These observations should apply generally to the pH dependence of native state protein aggregation.

2.5.2 First Aggregation Step

The crossing point at pH 5.0 in Figure 2.1 shows the importance of the direction of titration but also indicates a condition at which the rate of aggregation is independent of the sample history. The strong influence of titration direction is in contrast to previous reports of pH-induced aggregation, for instance with Zn-free insulin that appears to be essentially reversible.[59] The nearly symmetrical behavior in that case (titration curves did *not* cross) was related to the dipole-like behavior of the protein, with high- and low-pH deviations from pI essentially leading to charge mirror images. The dramatically different shapes of low-to-high and high-to-low curves indicate important effects of the surface charge distribution not reflected in |pH – pI|. However, the pHs at maximum $d\tau/dt$ (5.0) are independent of direction, because they reflect only rates of change regardless of prior accumulations of aggregate and thus depend uniquely on the state of the free protein. This point is 0.2 pH unit below pI; this and the marked difference in aggregation rates for BLG-A and BLG-B[31] suggest an important role for the negative patch of BLG (Figure 2.9) wherein reside the additional two Asp residues of the A dimer. The variation of the charge in this domain accounts for the pH

dependence of aggregation, which is seen in Figure 2.3A to arise mainly from the first step. The impact of this first step can be understood from charge anisotropy: the onset of aggregation at pH ~4.6 for base titration in Figure 2.1A corresponds to a large positive domain (Figure 2.9C) capable of interacting with the negative domains of several others, resulting in an open aggregate with a lower fractal dimension.[60] A diffusion-limited analysis of this process[31] was shown to account for the I^{-1} dependence of the initial rate shown in Figure 2.4. Acid titration commencing at pH ~5.4 shows less asymmetry, which could lead to a more dense structure possibly producing higher turbidity (Figure 2.1A). Although the structure of the aggregate formed may depend on the direction, the state of free protein that determines the rate of the first step does not.

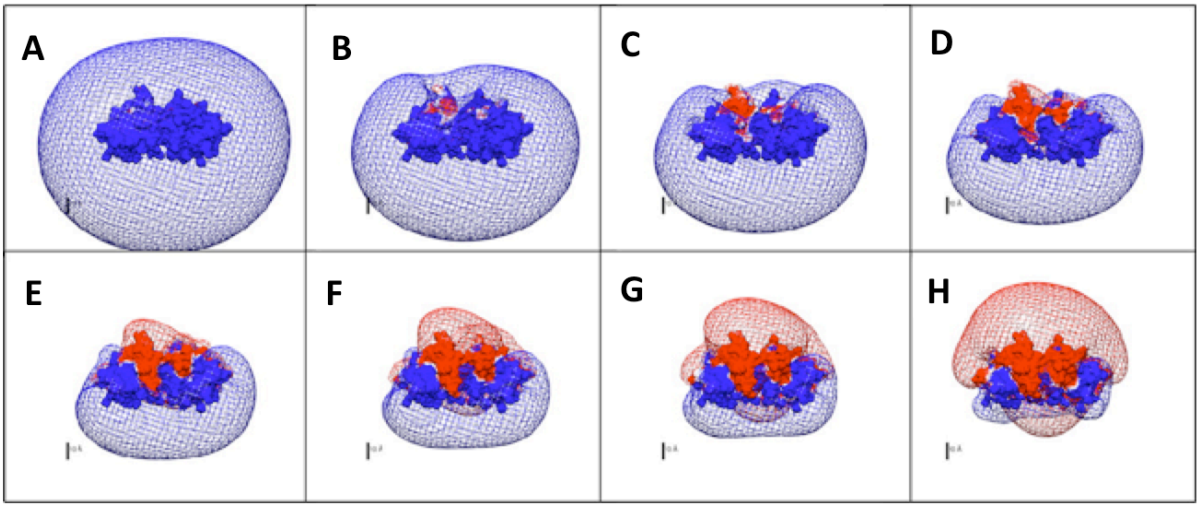

Figure 2.9: Electrostatic potential contours (+0.5*kT*/*e* (blue) and −0.5*kT*/*e* (red)) around the BLG dimer at ionic strength 0.0045 M. pH values and corresponding net charges: **(A)** 4.0, +12, **(B)** 4.4, +7, **(C)** 4.6, +6, **(D)** 4.8, +5, **(E)** 5.0, +3, **(F)** 5.2, 0, **(G)** 5.4, −2, and **(H)** 5.8, −3. Calculation was based on pdb id 1BEB, which has the same arrangement (and number) of charged residues as BLG B but has an additional noncharged amino acid. The scale bar is equal to 1 nm. Dimer net charge[61] rounded to the nearest whole number.

2.5.3 Second Aggregation Step

In marked contrast to the behavior of the first step, we see for $(d\tau/dt)_2$ Figure 2.3B, aggregation behavior that is highly asymmetric with respect to pH, with a local maximum at pI, and a remarkably linear pH dependence of $d\tau/dt$ at lower pH. This linearity is consistent with the linearity of net protein charge Z with pH in this region,[61] along with maximum aggregation at pH = pI, this suggests that global charge, not anisotropy, is dominant. As seen in Figure 2.4, the diminution of $(d\tau/dt)_2$ with added salt also implies an electrostatic attractive force, even at pH = pI. However, $(d\tau/dt)_0$ shows a stronger ionic strength dependence, increasing with I^{-1}. This proportionality was previously explained[31] as a consequence of an increase in the target area of the protein negative domain with the square of the Debye length κ^{-1}, which leads to the observed I^{-1} dependence because for 1:1 electrolytes $\kappa^{-1} \approx 0.3/I^{1/2}$ (where the units of κ^{-1} and I are nm and M). $(d\tau/dt)_2$, however, depends on $I^{-0.25}$. Because free protein is consumed before the second step, it is necessary to identify a weakly screened attractive force between clusters of low net charge. The theory by Miklavic for inhomogeneously charged surfaces at short separation describes an attractive force that becomes dominant when charges can migrate.[62, 63] With any aggregating system, diffusion will eventually induce microscopic concentration fluctuations that will bring two particles to the short separation distances at which such theory becomes very relevant. The overall attraction in this treatment increases with intercharge spacing and decreases with κ^2, the first term dominating for low salt. To this effect we add a weak Z-dependent repulsion that decreases with increasing κ (i.e., increasing I). The relative magnitudes of these two opposing effects depend on the intercharge spacing of the cluster surface, which is not known, but the observed $I^{-0.25}$ dependence of the attraction reflects their sum. The treatment

of Miklavic et al. suggests that a balance between attraction and repulsion dictated by charge spacing on the surface of protein clusters could lead to the observed *I* dependence. In summary, protein net charge *Z* provides a weak repulsion, and its disappearance at pH 5.2 accounts for the maximum in $(d\tau/dt)_2$ in Figure 2.3B. The mobility of protein charges on the cluster surface accounts for the attractive force that drives cluster–cluster association, in contrast to the fixed charges on the nonaggregated dimer that control the first step.

2.5.4 BLG-A and BLG-B

The influence of protein charge anisotropy, in particular, the role of the negative domain seen most clearly in Figure 2.9D–F, can be assessed by a comparison of BLG-A and BLG-B. The type 1 titrations in Figure 2.7 reveal aggregation rates an order of magnitude higher for the -A isoform. Focusing first on the crossing points where turbidity is independent of the direction of titration, it is reasonable to suggest that these represent the rate of aggregation of the dimer (first step). The crossing points of pH 5.2 and 5.4 for AA and BB, respectively, suggest that an increase in pH to 5.4 for BB results in behavior similar to that of AA at pH 5.2. Thus titration with NaOH up to pH 5.0 involves more retention of net positive protein for BLG-B (pI ~5.2) than for BLG-A (pI ~5.1), accounting for the accumulation of fewer aggregates and the absence of a crossing point. Comparison with Figure 2.1 shows that the aggregation rate at pH 5.0 (high to low titration) for native BLG is lower than that for AA by a factor of 3, even though the protein concentration is twice as large for the native form. The finding that the turbidity of native BLG (Figure 2.1) is much smaller than the sum of the contributions of AA and BB (Figure 2.7) is also in agreement with earlier observations that BB suppresses the aggregation of AA.

2.5.5 Turbidimetric Titration of BSA

The charge anisotropy of BSA (Figure 2.10) is distinctly different from that of BLG. As in the case of BLG, the absence of any influence of the titration direction on the pH of the maximum aggregation rate (pH_{max}) reflects the dominant role of the charge anisotropy of the free protein. However, pH_{max} is above pI for BSA vs. below pI for BLG. There are two possible explanations for this effect. If positive patches are stable at low pH, as is the case for BSA in the range of $4.5 < pH < 6$,[64] then the aggregation rate will be determined by the expansion of the diffuse negative domain at higher pH; if a negative patch is stable at high pH, then aggregation will be enhanced by the expansion of a diffuse positive domain at lower pH. This scenario describes BSA and BLG, respectively. The second explanation involves two steps, the first some form of nucleation and the second reflecting the tendency of net charge to oppose cluster formation. Preliminary kinetics experiments suggest that this two-step mechanism is consistent even at 10-fold-higher protein concentrations. Because the two steps have different pH and concentration dependences, the transition from step 1 to step 2 during the course of a type 1 titration will depend not only on the direction of titration but also on the rate of acid/base addition and on the total protein concentration. A more detailed investigation of this scenario would involve monitoring the initial and aggregated species by DLS as a function of the direction and rate of pH change, which is beyond the scope of the current work.

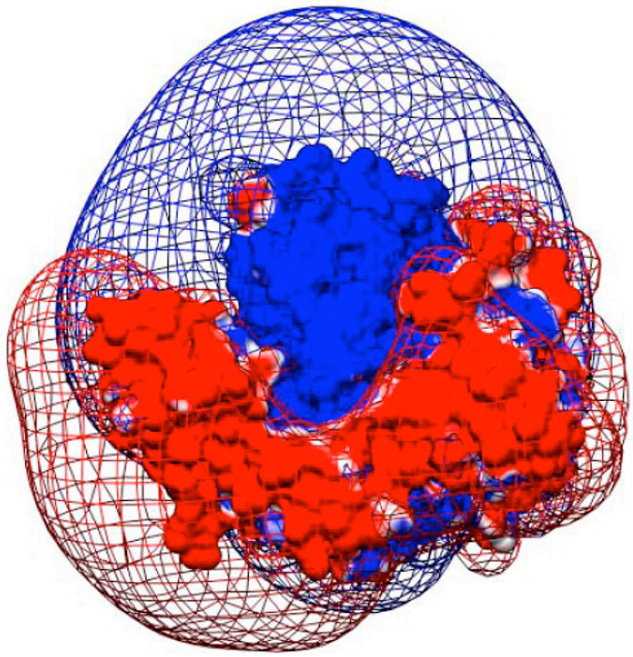

Figure 2.10: Electrostatic potential contours (+0.5*kT*/*e* (blue) and −0.5*kT*/*e* (red)) around BSA at an ionic strength of 0.0045 M and pH 5.4 (conditions identical to those for BLG in Figure 2.9G).

2.6 Conclusions

Turbidimetric pH titrations (type 1 titration) conveniently provide accurate measurements of the pH-dependent rate of aggregation ($d\tau/dt$) of native state proteins: the pH of the maximum aggregation rate (pH_{max}) and the ionic strength dependence of ($d\tau/dt$) are equivalent to results from kinetic measurements. The results for BLG lead to the identification of two predominantly electrostatic steps. The rate of the first step, ascribed to the aggregation of free protein and dominated by charge anisotropy, is symmetrical around pH_{max} (4.9) and inversely proportional to the ionic strength. At pH_{max}, DLS kinetics shows the rapid growth of apparent size at early time relative to that at pH 5.1, whereas SLS of

aggregates at both pHs shows the formation of increasingly dense structures consistent with particle–cluster aggregation. The relatively slow aggregation rate in the second step varies linearly with pH at constant I for pH < pI and is inversely proportional to $I^{0.25}$. This process is due to the association of clusters with inhomogeneous and mobile charge surfaces. The role of charge anisotropy in the first step is substantiated by the more rapid aggregation of the A isoform of BLG and by the contrasting aggregation behavior of BSA with inverted charge anisotropy.

2.7 Acknowledgments

We thank Dr. Christophe Schmitt and Prof. Sven Holger Behrens for helpful discussions. B.Z. acknowledges the support of a Bradspies summer research fellowship.

2.8 Supporting Information

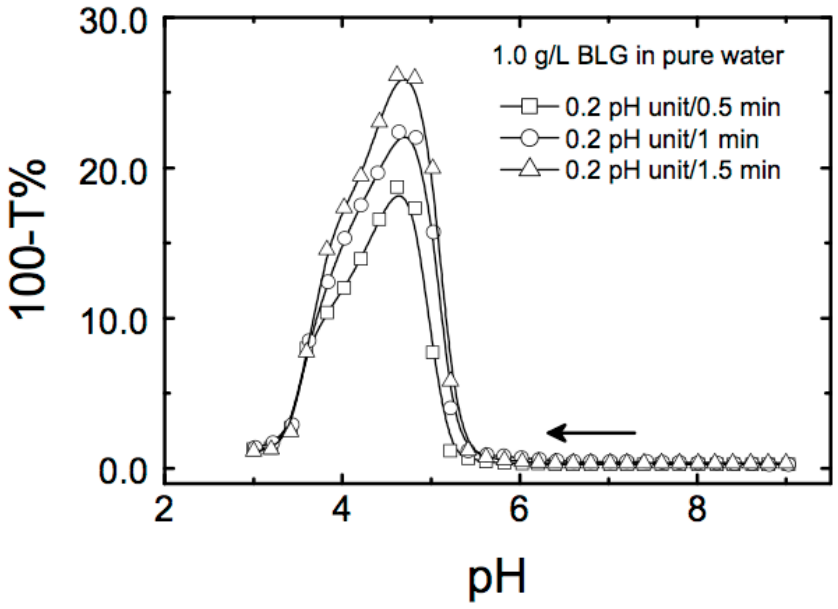

Figure 2.11: Type 1 titration of 1.0 g/L BLG from high to low pH with titration rates of 0.4 pH unit/min, 0.2 pH unit/min, and 0.13 pH unit/min.

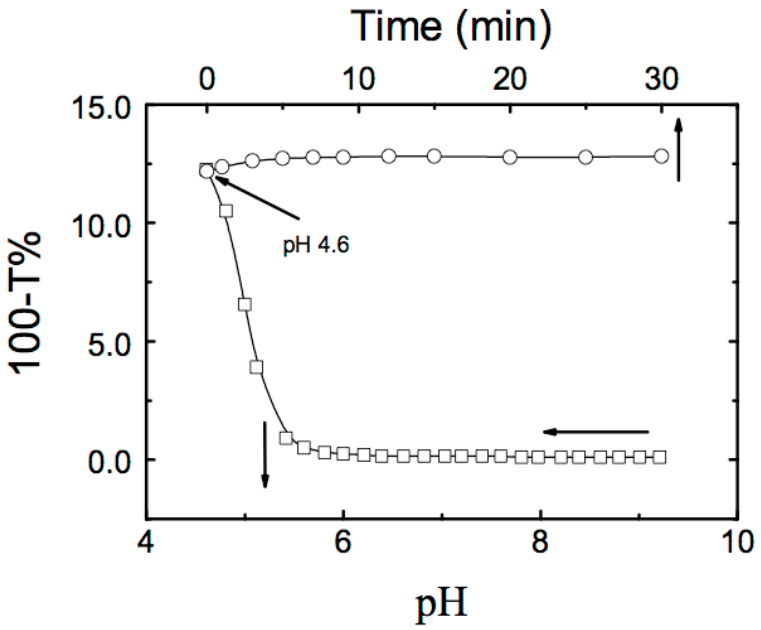

Figure 2.12: 1 g/L BLG in 0.0045 M NaCl was titrated with 0.1 N HCl to pH 4.6 (the point of maximum turbidity) (lower curve, □). The absence of any time dependence (upper curve, ○) confirms the equality of aggregation and disaggregation rates at this condition.

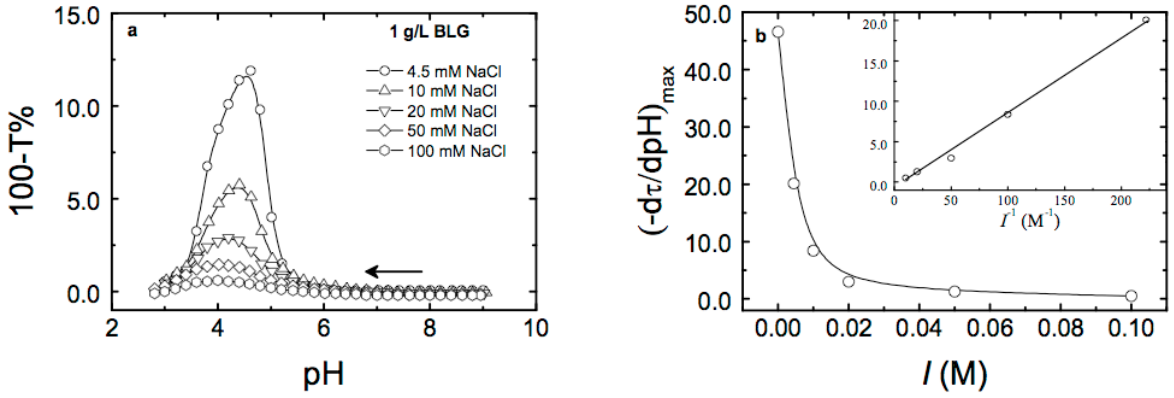

Figure 2.13: (A) Type 1 titration of 1.0 g/L BLG with 0.1 N HCl in 0.0045-0.1 M NaCl. **(B)** Ionic strength dependence of $(-d\tau/dpH)_{max}$. Insert: $(-d\tau/dpH)_{max}$ vs I^{-1}, agreement with kinetic studies confirms[31] extraction of rates from type 1 titration.

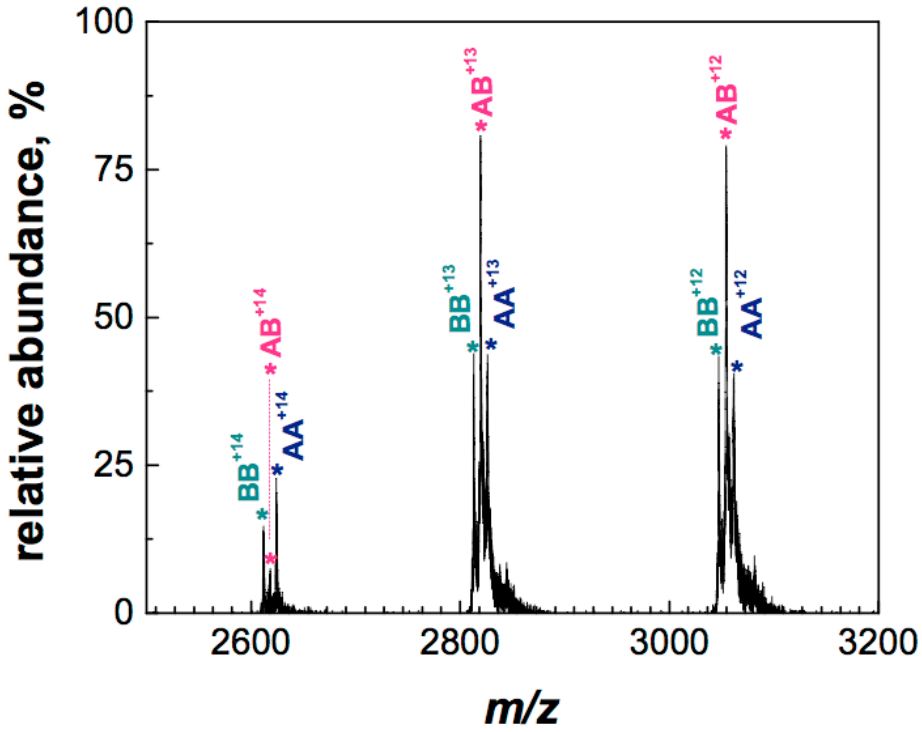

Figure 2.14: Mass spectra of BLG-A and BLG-B mixture (wt/wt, 1/1; C_{BLG} = 1.0 g/L) at pH 6.3. MS shows that "native" BLG is a statistical collection of AA, BB and AB with a ratio of 1:2:1.

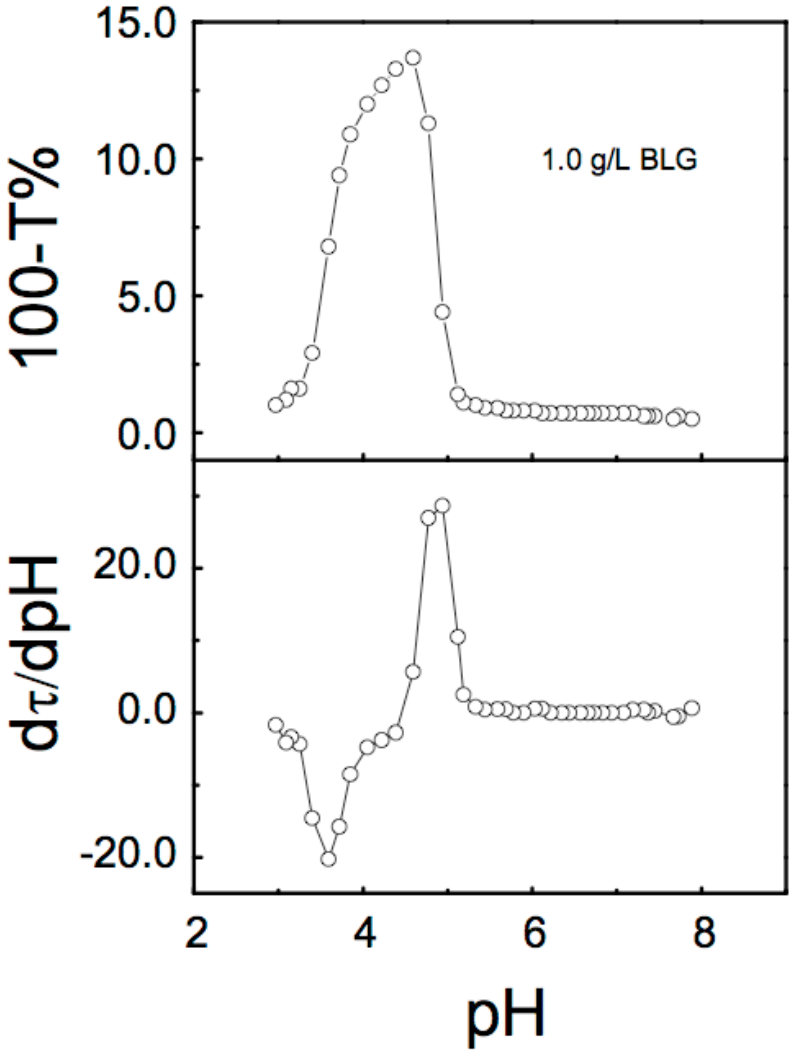

Figure 2.15: Type 1 titration of 1.0 g/L BLG in 0.0045 M NaCl with 0.1 N HCl.

CHAPTER 3

STRUCTURE OF BOVINE β-LACTOGLOBULIN–LACTOFERRIN COACERVATES

Ebru Kizilay, **Daniel Seeman,* Yunfeng Yan**, **Xiaosong Du**, **Paul L. Dubin**, **Laurence Donato-Capel**, **Lionel Bovetto, and Christophe Schmitt** *Soft Matter*, **2014**, 10, pp 7262-7268

*corresponding author

3.1 Abstract

Lactoferrin (LF) and β-lactoglobulin (BLG) are among the protein pairs that exhibit heteroprotein coacervation, a unique and relatively unexamined type of liquid–liquid phase separation (LLPS). In prior work we found that LF and BLG undergo coacervation at highly constrained conditions of pH, ionic strength and protein stoichiometry. The molar stoichiometry in coacervate and supernatant is LF:BLG_2 1:2 (where BLG_2 represents the 38 kDa BLG dimer), suggesting that this is the primary unit of the coacervate. The precise balance of repulsive and attractive forces among these units, thought to stabilize the coacervate, is achieved only at limited conditions of pH and *I*. Our purpose here is to define the process by which such structural units form, and to elucidate the forces among them that lead to the long-range order found in equilibrium coacervates. We use confocal laser scanning microscopy (CLSM), small angle neutron scattering (SANS), and rheology to (1) define the uniformity of interprotein spacing within the coacervate phase, (2) verify structural unit dimensions and spacing, and (3) rationalize bulk fluid properties in terms of inter-unit forces. Electrostatic modeling is used in concert with SANS to develop a molecular model for the primary unit of the coacervate that accounts for bulk viscoelastic properties. Modeling

suggests that the charge anisotropies of the two proteins stabilize the dipole-like $LF(BLG_2)_2$ primary unit, while assembly of these dipoles into higher order equilibrium structures governs the macroscopic properties of the coacervate.

3.2 Introduction

Complex coacervation, a spontaneous liquid–liquid phase separation, can be exhibited under a wide range of conditions by a variety of systems including: oppositely charged polyelectrolytes (PE),[65] or PEs in combination with oppositely charged macroions including proteins[66, 67, 68] micelles[69, 70] or dendrimers.[71] These phenomena all differ from coacervation of oppositely charged proteins[72, 73, 74] which is known to arise from the tendency of those macroions to assemble as dense, homogeneous fluids under a very limited range of stoichiometry, ionic strength and pH.[72, 75] Heteroprotein coacervation is still a largely unexplored phenomenon, with the majority of publications originating from a single group, in many cases not explicitly identified as complex coacervation.[76, 77, 78] The lactoferrin–β-lactoglobulin system serves as one example of a heteroprotein coacervation with characteristic dependence on the aforementioned variables.[75]

The relatively few papers reporting on heteroprotein coacervation reveal substantial differences from classic examples of complex coacervation. Soluble complexes have been established as precursors in nearly all typical forms of macroionic coacervation[79] and in some cases, particularly those involving PE–colloid systems, these complexes and aggregates thereof have been well characterized by techniques such as light scattering[80] and electrophoresis[81, 82] and neutron scattering.[83] Evidence for analogous primary complexes in heteroprotein systems is currently very limited. Charge stoichiometry ([+]/[−]) appears to play a different role for heteroprotein *vs.* PE–PE or PE–colloid coacervation, often appearing

in the latter case as the dominant factor determining coacervation yield, but apparently a necessary but not sufficient condition for heteroprotein coacervation.[84] The range of charge stoichiometry over which this form of coacervation can occur seems more narrower than for the more typical macroionic systems.[85] The difference between highly flexible polyions and conformationally rigid globular proteins would of course be expected to have dramatic consequences because of the limitations of ion-pairing on intermolecular mixing in the protein–protein case, leading to a greatly reduced role for counterion release and configurational entropy in the heteroprotein system. Phenomenological studies of the conditions under which heteroprotein systems coacervate have illuminated some of these issues.[86, 87]

In our previous study,[75] we used turbidimetry and dynamic light scattering (DLS) to examine the conditions that lead to coacervation in a system composed of two bovine milk proteins: β-lactoglobulin (BLG) and lactoferrin (LF). Complex coacervation of these two oppositely charged proteins was obtained only under a very narrow range of ionic strength, pH, total protein concentration, and protein–protein stoichiometry. The last variable was constrained to 1:1 weight ratio (1:4 mole ratio). This same stoichiometry was observed in both supernatant and coacervate, corresponding to complexes that were also detected in less concentrated one-phase systems. These constraints on conditions for pure coacervation were attributed to *inter alia* (1) the requirements for the formation of a basic primary unit, $LF(BLG_2)_2$, and (2) effective competition with BLG self association which depletes free BLG. However, it is unknown whether this $LF(BLG_2)_2$ primary unit is subject to disproportionation and therefore whether the features of this complex might not be retained in the resultant structures; and whether the variables such as pH, ionic strength and

stoichiometry that dictate assembly – within their highly constrained ranges – could affect the resultant properties of the coacervate.

Here we use confocal laser scanning microscopy (CLSM), small-angle neutron scattering (SANS) and rheology to better understand the structure of BLG–LF coacervates formed in the absence of added salt, at pH near 6. Electrostatic and molecular modeling is used in conjunction with experimental SANS data to determine the geometry and interparticle spacing of the primary unit of the coacervate $LF(BLG_2)_2$. Finally, the apparent hierarchical structure of the dense phase at different conditions is used to explain the unique and pH-dependent viscoelastic properties of the coacervate.

3.3 Experimental section

Materials. Bovine β-lactoglobulin (36 kDa) (from Davisco Foods International, Inc., batch number: JE 001-8-415) and lactoferrin (76–80 kDa) (from DMV International Nutritionals, Netherlands, batch number: 10444427), supplied by Nestlé Research Center (Lausanne, Switzerland). The compositions were (g per 100 g wet powder), 97% (for LF); and BLG-A (55.4%), BLG-B (41.6%), and α-lactalbumin (1.6%) (for BLG). Lactoferrin, an iron-containing protein has two $2Fe^{3+}$ binding sites and appears orange due to iron absorbance. Milli-Q water was used in all sample preparation.

Preparation of samples for SANS and rheology. Stock 40 g L^{-1} solutions of each protein were prepared in filtered D_2O for SANS, and in Milli-Q water for rheology. The solutions were adjusted to a target pH (5.8 or 6.0 for rheology, 6.0 for SANS) using 0.1 N NaOH or HCl. To prepare coacervates the LF solution was quickly poured into a pre-adjusted BLG solution in 15 mL centrifuge tubes followed by vortexing for 10 s and centrifuging for 30

min at 3200 × *g*. The total starting protein concentration was 40 g L^{-1} for SANS and rheology.

Protein labeling. Fluorescently labeled proteins, FITC-BLG and RITC-LF, were prepared according to Zhang et al.[88] Stocks of 5 g L^{-1} FITC or RITC ethanol solution were added dropwise under mild stirring into 200 μM BLG or LF in pH 8.0, 0.1 M phosphate buffer with a molar ratio (dye–protein) of 2.0. After 1 h reaction in the dark, labeling was terminated and free dye was removed by dialysis (10 kDa MW cutoff) against 10 mM Tris–HCl buffer (pH 7.4, 0.6 M NaCl). The external solution was replaced by Milli-Q water to remove salt; at least 4 times. Bright yellow FITC-BLG and purple RITC-LF were obtained after freeze-drying.

Confocal laser scanning microscopy (CLSM). Samples for microscopy were prepared by mixing 20 g L^{-1} protein stock solutions prepared in Milli-Q water at pH 6.0, followed by 1.0 h equilibration. The morphology and protein distribution in BLG–LF (containing 0.5‰ labeled protein) droplets were investigated by confocal scanning laser microscope (Leica TCS SP, Germany). A 50× objective lens was used for generating confocal images in transmission mode. Emission spectra of FITC-labeled proteins were taken from 500–530 nm with excitation wavelength 488 nm. Emission spectra of RITC-labeled proteins were taken from 590–620 nm with excitation wavelength 543 nm.

SANS measurements. Scattering experiments were carried out on coacervates using the CG-2 (General-Purpose SANS (GP-SANS)) instrument at Oak Ridge National Laboratory (ORNL). SANS spectra $I(\boldsymbol{q})$ were obtained as dependence of intensities on the scattering vector $\boldsymbol{q} = (4\pi/\lambda)\sin\theta$, where λ is the neutron wavelength, and 2θ the scattering angle. The sample was held at 15 °C in a 1 mm quartz banjo cell. Data from two sample-to-detector

distances (1 and 14 m) were merged to give an effective ***q***-range of approximately 0.004 to 0.48 $Å^{-1}$ (using 6 Å neutrons). Raw data were processed using data reduction modules provided by ORNL and then adjusted to an absolute scale by measuring the scattering of a provided standard at low-***q***. Prior to merging, scattering from an empty cell was subtracted from data corresponding to both detector configurations to account for background scattering, for high-***q*** and low-***q*** data.

Rheology. Rheology of coacervates was measured with a stress-controlled rheometer (TA Instruments AR-G2) with cone and plate geometry. The samples were loaded at 25 °C with a measurement gap of 1 mm. After a 15 min conditioning time, dynamic oscillatory frequency sweeps were made from 100 to 0.1 rad s^{-1} with an oscillatory strain amplitude of 5%, which was determined to be in the linear viscoelastic regime for the ranges of frequency and temperature investigated.

Electrostatic modeling. DelPhi[3] V. 4r1.1 was used to model the electrostatic potential around the proteins as a function of pH and ionic strength. PDB ID 1BLF (diferric bovine LF) and 1BEB (BLG dimer) were taken from the RCSB Protein Data Bank (http://www.rcsb.org). Amino acids charges were generated using the spherical-smeared-charged model proposed by Tanford based on titration curves of BLG[61] and LF (Figure 3.7). Atomic coordinates were used to calculate single-particle form factors as well as R_g, for individual proteins and protein–protein complexes, using CRYSON 2.7.[89]

3.4 Results

3.4.1 Confocal microscopy. BLG and LF appear to be uniformly dispersed within coacervate droplets. Confocal laser scanning microscopy was used to investigate the

distribution of component proteins in (1) BLG–LF suspensions of 10–50 μm droplets, obtained by mixing labeled LF and BLG at pH 6.0 and C_p = 20 g L^{-1} (1:1, w/w), and (2) corresponding coacervates obtained after 24 h settling. The fluorescent label, present at less than 0.25% total protein, was found to have no inhibitory effect on coacervation. Figures 3.1C and D indicate that BLG and LF are homogeneously dispersed throughout the droplets at the 20 μm scale.

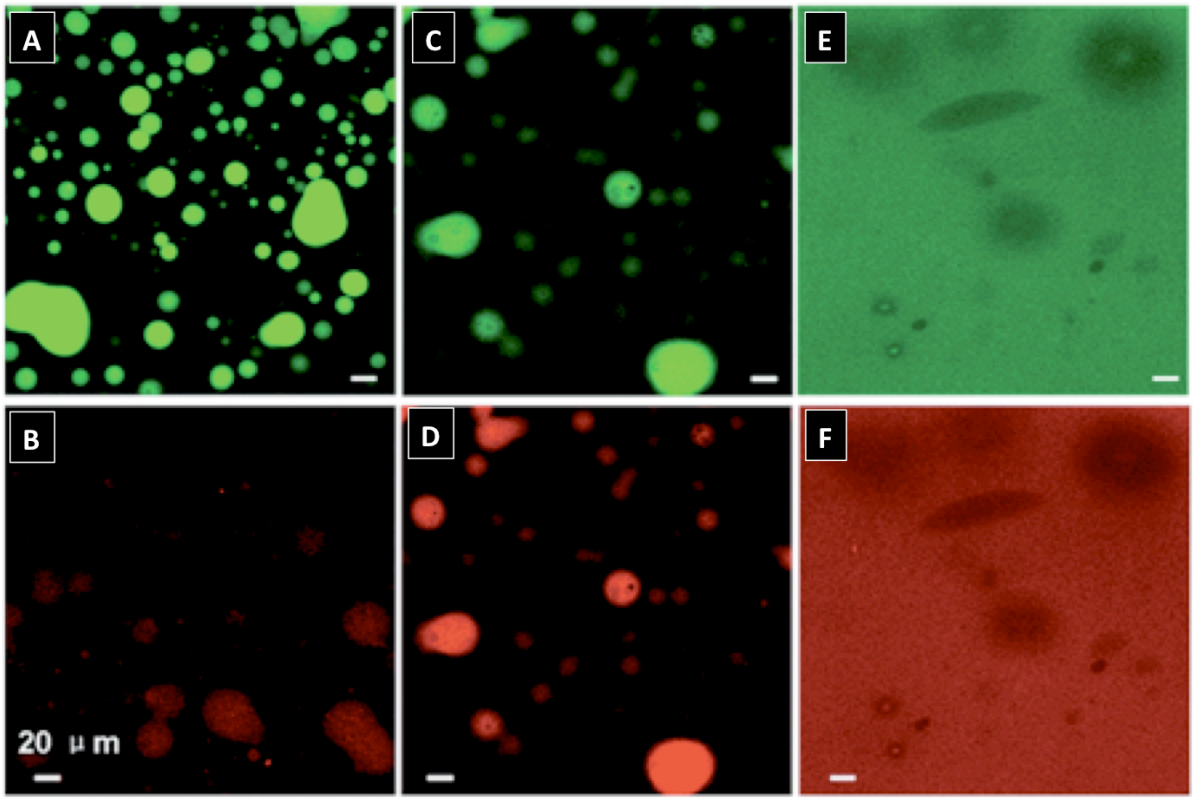

Figure 3.1: Confocal images of **(A)** suspensions of FITC-BLG–LF, **(B)** BLG–RITC-LF, and **(C)** and **(D)** FITC-BLG–RITC-LF; and **(E** and **F)** coacervate of FITC-BLG–RITC-LF after 1.0 h equilibration. C_p = 20 g L^{-1}, r_{wt} = 1.0, pH = 6.0, 0 mM NaCl. Excitation wavelengths 488 nm **(A, C** and **E)** and 543 nm **(B, D** and **F).** Emissions wavelengths 500–530 nm **(A, C** and **E)** and 590–620 nm **(B, D** and **F)**.

3.4.2 Small-Angle Neutron Scattering (SANS).

Observed scattering can only be explained by the existence of a primary unit with

dimensions comparable to $LF(BLG_2)_2$. The coacervate homogeneity at large length scales established by CLSM supports the use of SANS and its attendant length scales for elucidation of coacervate structure, in order to observe structural features too small to be optically resolvable. In order to extract basic structural information, a series of standard plots was constructed as shown in Figures 3.2A,B.

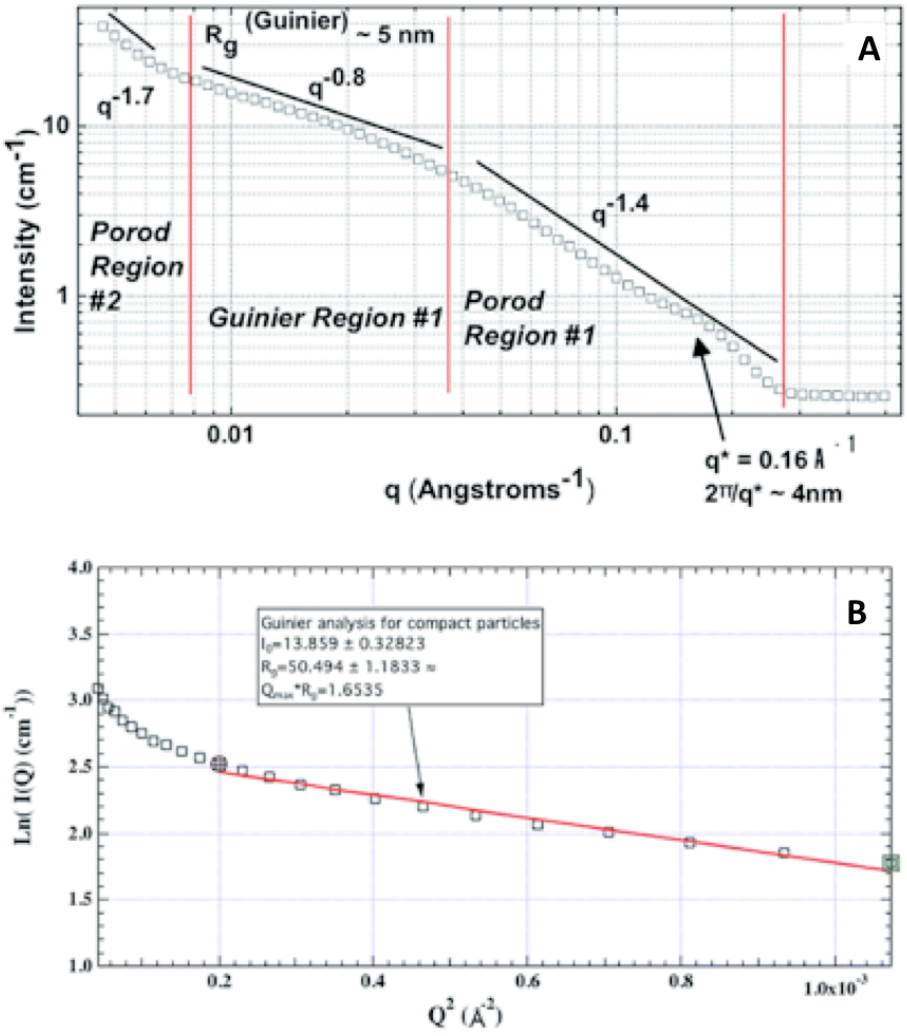

Figure 3.2: SANS of BLG–LF coacervate. **(A)** Porod exponents for all regions **(B)** Guinier plot (R_g = 50.5 ± 1.1 Å). Also reported is the correlation length (40 Å) corresponding to ***q****. The existence of a second Guinier region is inferred at lower-***q***.

Data were subdivided according to observed scaling laws, with data between

approximately $\boldsymbol{q}$ = 0.008 and 0.035 Å^{-1} used to estimate radius of gyration of 5 nm, *via* a Guinier plot (figure 3.2B). For the first Porod region, scattering scales as $I \propto \boldsymbol{q}^{-1.4}$, suggesting a loosely packed structure intermediate between rod and fractal aggregate. While the first Porod region more closely resembles a branched cylindrical object, the second Porod region, corresponding to higher order structures, shows scaling more characteristic of a classical fractal aggregate, suggesting a mechanism by which primary units may assemble to form larger structures. Additionally a correlation peak, q^*, was observed at $\boldsymbol{q}$ = 0.16 Å^{-1}, suggesting a correlation length of approximately 4 nm, although the broadness of the peak indicates considerable polydispersity with respect to position and orientation of protein monomers within a primary unit.

3.4.3 Rheology

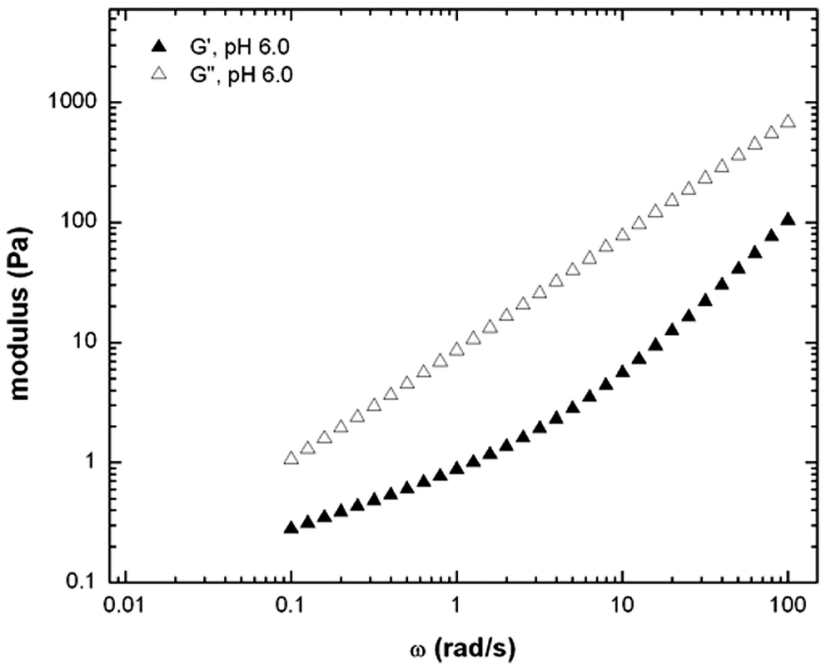

Figure 3.3: Dynamic oscillatory frequency sweeps of coacervate formed at pH 6.0, at 5% strain (G': closed and G'': open symbols).

The frequency-dependent viscoelastic moduli of coacervates prepared from BLG and

LF solutions prepared at pH 6 are shown in Figure 3.3. Oscillatory strain amplitude was determined to be in the linear viscoelastic regime over the range of frequencies used. Samples prepared at different mixing pHs (Figure 3.7) – (note that we did not attempt to measure the pH of the coacervate itself) all show viscoelastic behavior consistent with a highly viscous liquid, *i.e.* the storage (elastic) modulus G' is always less than the loss (viscous) modulus G''.

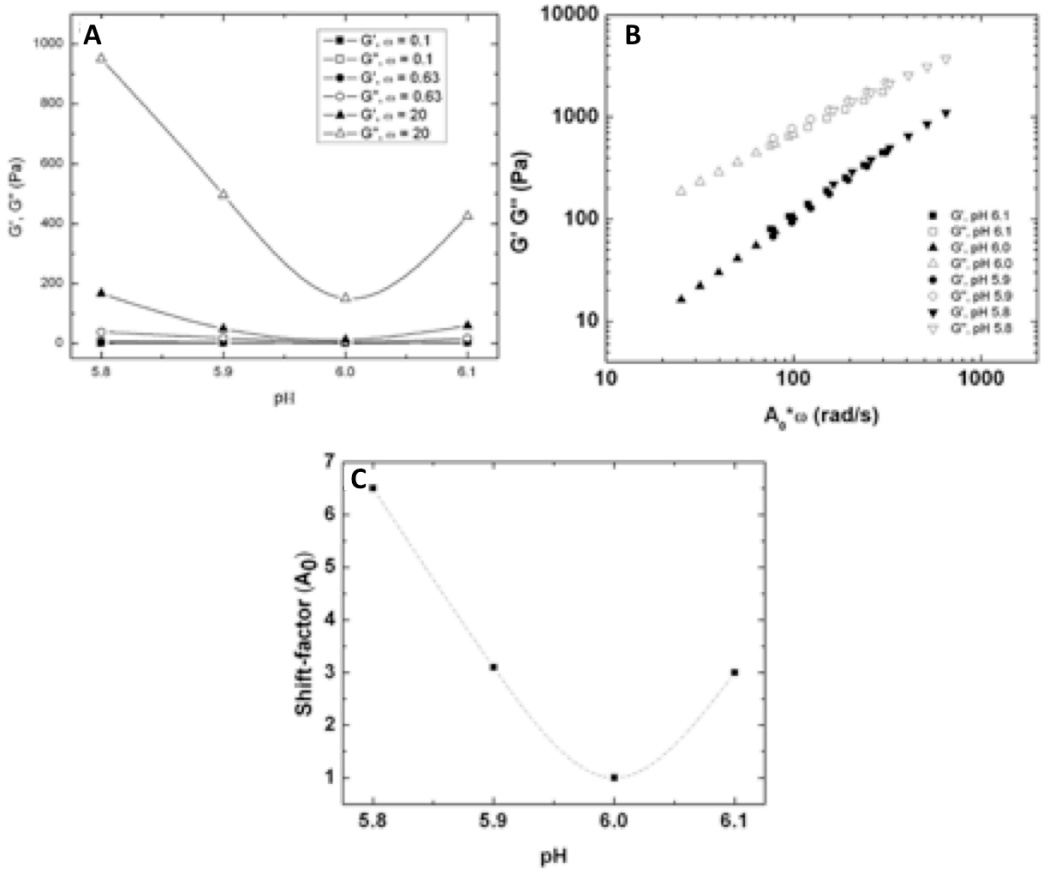

Figure 3.4: G' and G'' for coacervates prepared at four mixing pHs, results are shown at ω = 0.1, 0.63, and 20 (s^{-1}); using data from figures 3.3 and 3.7; **(A)** G' and G'' as a function of mixing pH; **(B)** Superposition of high frequency (ω > 25 rad s^{-1}) data; **(C)** pH dependence of the shift factors used in ***B***.

For coacervates prepared at pH 6, the frequency dependence of G'' is constant across all measured ω values up to 100 rad s^{-1}. In contrast, the dependence of G' on ω increases

sharply above ω = 10 rad s^{-1}. G'' is larger than G' at all measured frequencies, indicating that any crossover point must occur at ω > 100 rad s^{-1}. This suggests that the interconnected structures responsible for the viscoelastic properties have characteristic relaxation times shorter than 0.01 s. Linear extrapolation in Figure 3.3 of G' and G'' up to their cross-over point gives a typical relaxation time of 0.001 s. The viscous modulus (G'') at ω = 0.1, 0.63, and 20 is shown to increase dramatically at pH < 6, particularly at higher frequencies (ω = 20) (Figure 3.4A, open symbols).

High frequency (ω > 25 rad s^{-1}) data were superimposed (Figure 3.4B) using a pH dependent shift factor A_0 (Figure 3.4C). The success of this superposition using only shifts in ω suggests that the shear modulus G_0, as obtained from a Maxwell fit (eqn (3.1) and (3.2)), should be largely invariant with respect to mixing pH.

$$G' = G_0(\omega\tau)^2/(1 + (\omega\tau)^2) \quad \textbf{(3.1)}$$

$$G'' = G_0(\omega\tau)/(1 + (\omega\tau)^2 \quad \textbf{(3.2)}$$

3.5 Discussion

3.5.1 Atomistic Model of the Primary Unit.

Protein charge anisotropy allows us to construct an atomistic model of the primary unit. The results from SANS can be interpreted on the basis of a molecular model consistent with the charge anisotropy and structure of the individual protein monomers using two assumptions: (1) the charge anisotropy of the individual proteins controls formation of primary units at incipient coacervation, and (2) the dipolar structure of this complex controls long-range order in separated coacervate phases. This primary unit, $LF(BLG_2)_2$ (Figure 3.5)

was constructed using the atomic coordinates of LF monomer and BLG dimer. The initial separation between BLG and LF in such complexes was taken to be no more than 6–7 nm. Coarse refinement of this structure was facilitated by comparison of calculated form factors with experimental scattering curves. Since the component proteins are chemically and structurally monodisperse, the only source of polydispersity is orientational and positional heterogeneity within the primary unit.

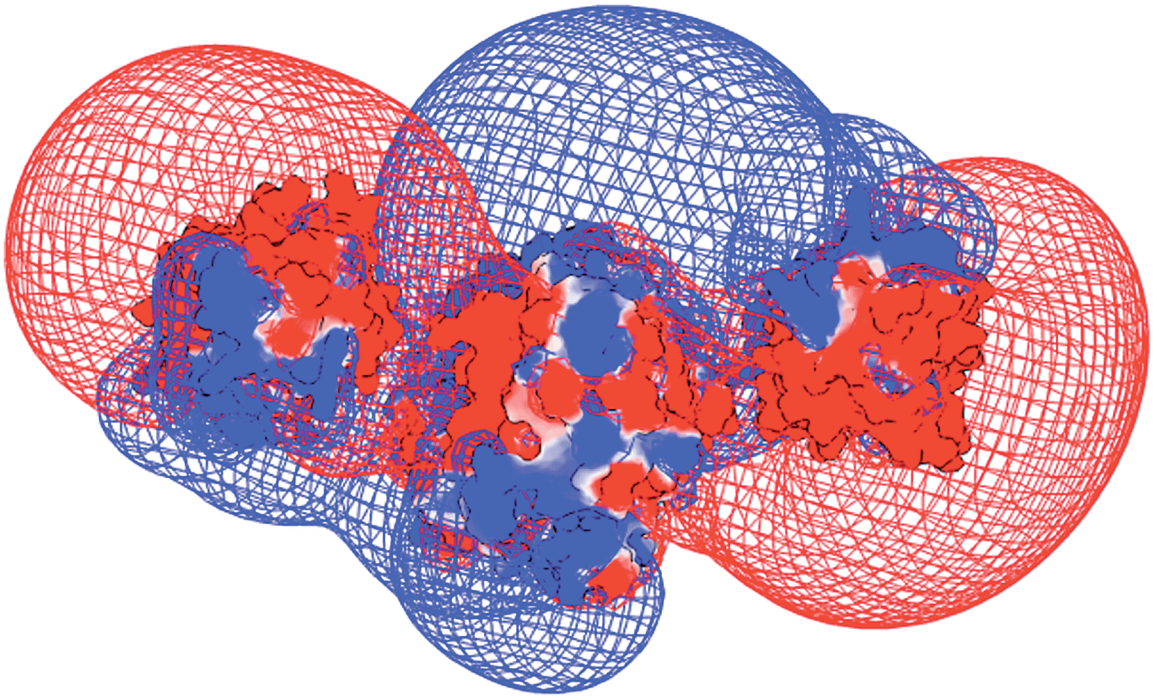

Figure 3.5: Proposed arrangement of BLG_2 (left): LF (center): BLG_2 (right). BLG–LF separation is taken to be less than 6 nm. Electrostatic potentials are contoured at −0.5 *kT*/*e* (red) and +0.5 *kT*/*e* (blue), potentials displayed are for pH 6.0. The calculated radius of gyration of this primary unit, R^{calc}_{g} = 4.5 nm, was obtained from CRYSON.

The coacervate phase appears homogenous at the length scales of optical microscopy, but the upturn seen at low-***q*** suggests that primary units must associate to form a structure greater than approximately 70 nm, not fully resolvable in the given ***q***-range. This requires the existence of an equilibrium structure of dimensions intermediate to those accessible to

fluorescence microscopy and SANS, and responsible for the bulk coacervate physical properties.

Data in the range of $\boldsymbol{q}$ = 0.01 to 0.48 Å^{-1} were compared directly to single particle form factors calculated[89] for BLG_2, and LF, alone, as well as from a molecular model of the proposed primary structural unit. In order to confirm the role of $LF(BLG_2)_2$ as the primary coacervate structural unit, scattering calculated from this model (Figure 3.6C) was compared directly to SANS data, as shown in Figure 3.6. The 'refined' primary unit (Figure 3.6C) is a minor structural rearrangement of the atomistic model shown in Figure 3.5.

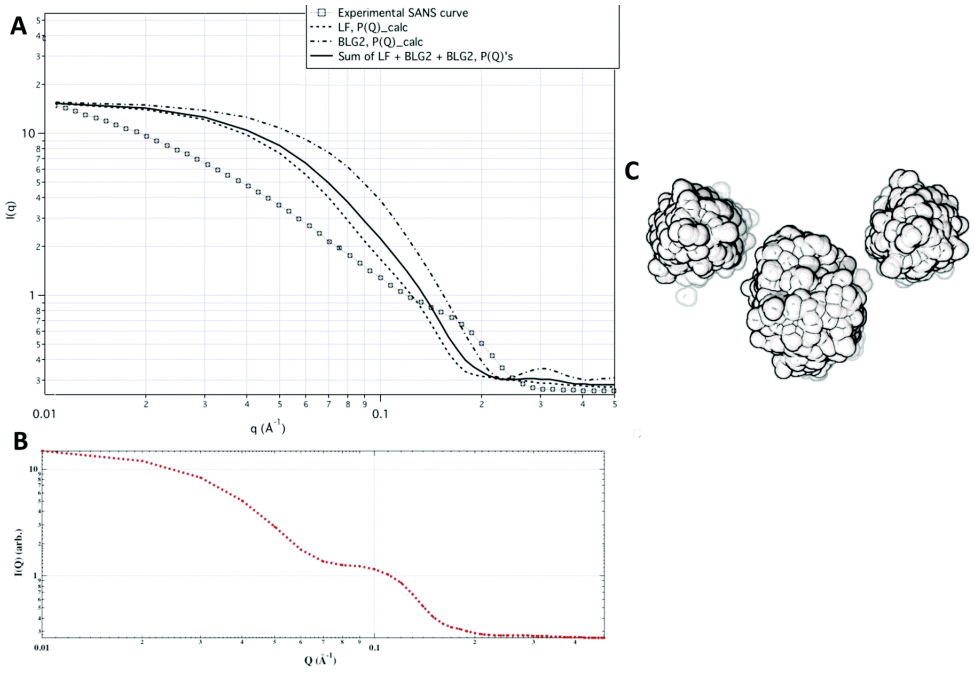

Figure 3.6: SANS data 0.004 < $\boldsymbol{q}$ < 0.48 Å^{-1} (open symbols) are presented alongside **(A)** calculated form factors for individual protein components LF, R^{calc}_g = 2.8 nm and BLG_2, R^{calc}_g = 2.1 nm, as well as for a form factor calculated from their arithmetic sum. **(B)** Form factor calculated from the proposed model of the primary unit, $LF(BLG_2)_2$ **(C)** refined geometry of primary unit, BLG_2–LF–BLG_2.

3.5.2 SANS is not Simply Additive

Scattering cannot result solely from free LF or BLG_2. It is clear from Figure 3.6A that scattering calculated from either component protein, or from their weighted sum, is inadequate to explain results below $\boldsymbol{q} = 0.12$ Å^{-1}. Diminution of scattering in Porod region #1 (see Figure 3.2) must be due to short-range interactions between the two proteins, while the upturn at very low $\boldsymbol{q}$ must result from higher-order structure comprised of assemblies of primary units. The observed exponent 1.4 is consistent with the absence of well-defined interfaces for these assemblies, in contrast to the scattering curves for individual proteins. The less well-defined peak at q^* in Figure 3.2 derives its breadth from a wider range of primary unit geometry in the actual sample.

3.5.3 Proposed Structure of $LF(BLG_2)_2$

The proposed structure of $LF(BLG_2)_2$ has dimensions consistent with those obtained from experimentally observed scattering. To determine the basis of these deviations in $\boldsymbol{q}$-dependent scattering, a molecular model of the primary unit, described by $LF(BLG_2)_2$, was constructed based on considerations of protein electrostatics. The initial, unrefined, model is presented in Figure 3.5, while scattering calculated from the refined configuration (Figure 3.6C), is shown above (Figure 3.6B). This arrangement adequately predicts the diminution of scattering intensity between $\boldsymbol{q} = 0.1$ and 0.01 Å^{-1}, suggesting that the data could best be described as an average of the angle-dependent scattering from a large ensemble of primary unit configurations with subtly different spacing and geometric arrangements. The calculated radii of gyration for the 'unrefined' and 'refined' models are in the range of 4.5 to 4.7 nm, consistent with dimensions obtained by Guinier analysis of figure 3.2.

3.5.4 Long-Range Order Through Inter-Primary Unit Interactions

Individual form factors for BLG dimers and LF monomers (Figure 3.6A) are insufficient to explain observed SANS data, but most scattering between $\boldsymbol{q}$ = 0.01 and 0.1 could be ascribed to the primary unit itself $LF(BLG_2)_2$, as represented by the average of an ensemble of different configurations. This leaves only the upturn at low-$\boldsymbol{q}$ unexplained, presumably resulting from association of primary units. Their organization can be characterized by a scaling law characteristic of loosely packed particles. One possible explanation for the observed long range order would be that the same protein charge anisotropy that stabilizes the $LF(BLG_2)_2$ primary unit also leads to attractive electrostatic interactions among primary units. This results in a network bridged by protein dipoles over a narrow range of length scales.

Changes in mixing pH should affect the fractional charges of titratable residues in both proteins, which are expected to affect the interactions among dipoles. The existence of a common value of G_0 for all mixing pH values supports a conserved elastic structure in all cases, while the decrease in characteristic frequency implies that the dynamics of the system are dramatically dependent on pH. This suggests that the lifetime of association of primary units or clusters varies with the crossover frequency, while the overall coacervate structure is preserved. Rheological properties likely arise from rearrangements of BLG_2 and LF within primary units, which may allow for optimization of repulsion and attraction.

CSLM reveals the presence of spherical and deformed droplets coalescing to form the coacervate, which can be interpreted as a sign of macroscopic viscoelasticity, consistent with findings from rheology. Solvent vacuoles within some droplets (Figure 3.1), is a sign of local

reorganization. This finding suggests that the coacervate can be characterized by motion on different time- and length-scales, as shown by rheology and SANS respectively. The absence of vacuole structures in the ALAC–LYS systems studied by Nigen *et al.* may suggest unique features of the LF–BLG_2 coacervates. The dissimilar tertiary structures and a high degree of charge asymmetry of BLG_2 and LF might facilitate the assembly of the unique structural unit, $LF(BLG_2)_2$.

3.6 Conclusions

Since neutron scattering of BLG–LF coacervates is poorly explained by a single, spatially fixed BLG_2–LF unit there must be ongoing intra-unit reorganization. Rheology verifies this assumption, showing that the elasticity of a network formed by the primary units is largely pH independent, while the shift in frequency dependence with pH reflects changes in the motions of individual proteins.

3.7 Acknowledgements

We acknowledge the support of NESTEC and of the NSF-sponsored Institute for Cellular Engineering IGERT Program (DGE-0654128) for travel support to Oak Ridge, TN. We thank Dr Yuri B. Melnichenko of the CG2 SANS beamline, at ORNL. Additional thanks to Christophe Tribet for helpful discussions.

3.8 Supporting Information

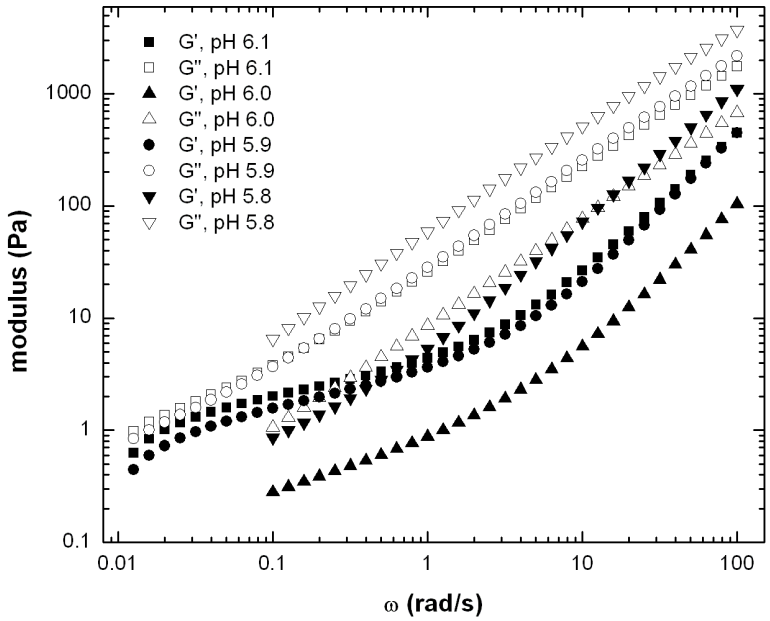

Figure 3.7: Dynamic oscillatory frequency sweeps at 5% strain (*G'*: closed and *G''*: open symbols) for coacervates prepared at four different mixing pHs. Triangles: pH 6.0, inverted triangles: pH 5.8, circles: pH 5.9 and squares: pH 6.1.

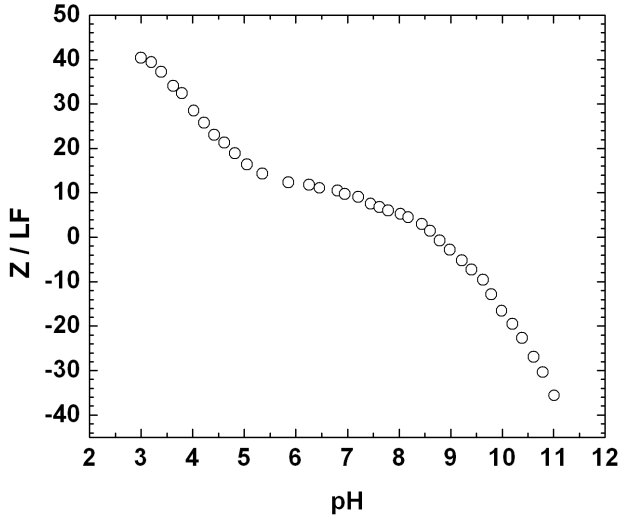

Figure 3.8: Potentiometric titration of bovine lactoferrin (LF) at room temperature (ca. 25^{o}C) with no added salt. [LF] = 20.8 g/L, total volume = 10 mL. Charge curve is the result of a high-to-low titration from isoionic pH using 0.1N HCl, and a low-to-high titration, starting from the same pH, using 0.1 N NaOH.

CHAPTER 4

NON-FREEZING WATER STRUCTURATION IN HETEROPROTEIN COACERVATES

Xiaosong Du, Daniel Seeman*, Paul L. Dubin, and David A. Hoagland ***2015,*** (submitted May 2015)

*corresponding author

4.1 Abstract

Surface-bound water in protein solutions has been identified with a reduction in its freezing point. We studied the presence of such non-freezing water (NFW) in various protein-polyelectrolyte, micelle-polyelectrolyte, and protein-protein (heteroprotein) coacervates, along with appropriate concentrated solutions of macromolecules alone, finding up to 15% w/w of NFW for the heteroprotein coacervate of lactoferrin (LF) and β-lactoglobulin (BLG). The level of NFW is always higher in coacervates than in the control (single-macromolecule) systems, particularly for protein-containing coacervates: a coacervate of bovine serum albumin (BSA) and poly(dimethyldiallylammonium chloride) (PDADMAC) showed a ratio of NFW/protein twice that of BSA alone (0.6 vs. 0.3), with a similarly high ratio for LF-BLG coacervate. These results are attributed to maximization of water-protein contacts, structural features that reflect the mode of sample assembly, as they are not seen in a non-coacervated LF-BLG solution with identical concentrations of all species.

4.2 Introduction

There has been long-standing interest in the role of protein hydration in crowded solutions of macromolecules, because such systems can serve as models for simple biological ones. At high protein concentration, hydration water has been shown to slow the effective diffusion of protein monomers relative to that in dilute solutions,[90, 91] possibly mediated by an increase in the protein's effective hydrodynamic size,[92] or simply by protein-water interactions.[93, 94] In order to understand the movement of proteins within such high-concentration solutions, it is also necessary to consider the diffusion of water molecules within a highly confined environment, a factor that controls both apparent molecular shape and size of the protein.[95, 96] The confinement of water near a protein surface carries a large entropic penalty; however, the formation of large numbers of enthalpically favorable hydrogen bonds, both among water molecules and with the protein surface, can often compensate energetically, with some theoretical treatments suggesting that such compensation is an essential feature of protein hydration.[97] The entropic portion of protein-solvent interactions in hydrated systems, is heavily influenced by electrolyte-mediated ordering of water molecules, similar to that seen in biological systems,[96, 98] which, can enhance repulsive protein-protein interactions, while disordering of water facilitates attractive interactions[96] and loss of solubility. [99]

Non-cognate or partially synthetic systems can resemble simple single-celled organisms: both are capable of sequestering and compartmentalizing charged macromolecules and establishing concentration gradients without the use of fixed membranes. Similarly, semi-permeable micro-compartments, consisting of conjugated protein–polymer building blocks, were seen to be capable of guest molecule encapsulation,

selective permeability and gene-directed protein synthesis.[100] The robust and porous micro-architectures in these biomimetic protocells were able to withstand partial dehydration and rehydration, allowing these protocells to be used in sustained storage and release of drugs and other bioactive molecules. Many such biomimetic systems can be formed from coacervates, or coacervate droplets, including those made from biological precursors. Coacervation in *E. coli* cell lysate-containing macromolecular components was found to create artificial, cell-like compartments in which the rate of mRNA production increased significantly with a transcription rate strikingly similar to those *in vivo*.[101] Coacervate droplets composed of polyelectrolyte and mononucleotides were used as a biomimetic reaction medium to stabilize the catalytic activity of contained enzymes.[102] A more recent review article by Keating[103] suggests that complex coacervation might be responsible for the segregation of nucleic acids in early protocells.

Complex coacervation is a special form of macromolecular liquid-liquid phase separation (LLPS) that gives rise to unique dense fluids with unusual sub-micron heterogeneity. In contrast to LLPS seen in many colloidal systems, complex coacervation arises from complexes of oppositely charged macroions formed by non-specific electrostatic interactions.[20] In typical LLPS systems, the homogeneous dense phase differs from the dilute phase only with respect to concentration; this is described by a coexistence plot, which expresses composition as a function of solute-solute interaction or temperature. In complex coacervation, however, the dense phase is not simply a more concentrated version of the dilute phase but exhibits microsopic heterogeneity due to the reorganization of the complex precursors; such ordering can be observed through structural or dynamic measurements.[104] Coacervation is also distinct from aggregation, not being subject to kinetics, and thus

displaying neither the corresponding fractal dimensions nor any internal interfaces.[70] A third notable feature of coacervates is the coexistence of dense and dilute microdomains within the equilibrium dense phase.[79] If these dense microdomains are essentially free of water, then most of the water in the coacervate should be bulk, i.e. normal freezing water (FW), and the amount of this FW should resemble the total amount of water. In contrast, concentrated protein solutions are known to exhibit varying amounts of "non-freezing" water,[105, 106, 107] related to protein solvation.[108, 109, 110, 111] Thus, if proteins in the dense domains of protein-based coacervates are well solvated (with or without rapid dynamics), much of the water should be NFW. Hence, comparison of NFW content should provide insight into the exact nature of dense microdomains within protein complex coacervates.

The formation of heteroprotein coacervates (HPCs), the most recently investigated category of complex coacervation[72, 87, 112] provides evidence of considerable structure formation. These HPCs differ from simple concentrated protein solutions in that they have (1) well-defined structure at the protein level[87, 113] and (2) substantial amounts of long–range order.[112, 113] This structuration is expected to involve overlap of protein hydration shells, resulting in large amounts of confined water. The formation of HPC from β-lactoglobulin (BLG) and lactoferrin (LF), to our knowledge the most studied HPC, is accompanied by expulsion of protons[114] due to a pK shift and involves a preferred orientation of the primary structural unit and assembly thereof[113] while an uncoacervated concentrated protein solution does not. This expulsion of protons was found to enhance protein dipoles and orientation of primary units within the coacervate, to a greater degree than that found in the uncoacervated BLG-LF mixture.[113, 114] In HPCs, the separation of primary units may not be uniform over longer length scales,[72, 113] but rather include local regions of lower water concentration

corresponding to locally organized primary unit "dipoles".[113] Thus, water trapped within HPCs should be more "perturbed" than the average water in a randomly organized simple binary protein mixture.

HPC structuration should differ from that found in more conventional coacervates, e.g. PE-PE, PE-micelle, and PE-protein systems. While average interprotein separation within HPCs and protein-PE coacervates might be similar, the heterogeneity and dynamics of protein sub-assemblies must differ in the presence of a protein-binding PE whose organizing effect can be seen by Cryo-TEM[115] and DLS,[116] indicating protein-rich and protein-poor on length scales on the order of more than 100 nm. Total internal fluorescence microscopy of BSA-PDADMAC coacervates[117] shows 200-400 nm protein-rich regions with lifetimes > 100 ms, indicating highly desolvated, even solid-like, domains from which water is likely to have been expelled along with counterions. HPCs are thus expected to have more uniformly distributed water than e.g. protein-polyelectrolyte coacervates. Water is thus more uniformly distributed in HPCs than in protein-PE coacervates, but measurements of NFW in coacervates have not been reported.

The purpose of this study is to gain insight into the properties of water confined within the coacervate phase, reflecting the intimacy of contacts between water and the macromolecular components. Here we examine water structure in HPCs in terms of non-freezing water. Calorimetric methods such as differential scanning calorimetry (DSC) have been used to monitor phase changes of water in polymers.[118] Such thermodynamic measurements permit the characterization of hydrated systems without recourse to detailed molecular models. We consider three coacervating systems with distinctly different components: protein-PE coacervates comprised of BSA and PDADMAC,[104] PE-micelle

coacervates formed from PDADMAC and SDS/TX-100 mixed micelles,[119] and a HPC of BLG and LF.[113] In addition, we carry out a unique and important comparison: we examine this HPC vis-à-vis a concentrated but not coacervated one-phase mixture of LF and BLG identical to the coacervate with respect to concentrations of all species, including water, the two macroions, NaCl, and $[H^+]$.

4.3 Experimental Section

Materials. The PDADMAC sample (gift from W. Jaeger, Fraunhofer, Golm) was prepared by free radical aqueous polymerization of diallydimethylammonium chloride and characterized after dialysis and lyophilization by membrane osmometry (M_n = 141 kDa) and light scattering (M_w = 219 kDa). BSA (68 kDa) with total free acid content ≤ 1.2 mg/g was from Roche Diagnostics (Indianapolis, IN; CAS 9048-46-8). BLG (monomer MW 18 kDa) and LF (76-80 kDa) were gifts from C. Schmitt (Nestle, Lausanne). Triton X-100 (TX-100) was purchased from Aldrich, sodium dodecyl sulfate (SDS, purity > 99%) from Fluka. NaCl, sodium acetate, sodium phosphate (monobasic), and standard NaOH, HCl, and acetic acid solutions were from Fisher Scientific. Milli-Q water was used in all sample preparation. Aluminum DSC pans and lids were purchased from TA Instruments, Tzero® technology.

Turbidimetric Titrations. Highly precise turbidimetric titrations (%T ± 0.05%) were carried out for solutions containing proteins, micelles and polyelectrolytes in order to determine the points of complex formation and phase separation (pH_c, pH_f). Within the range of 23-25 °C no temperature effect could be seen.

Preparation of Coacervates. To prepare PE-micelle coacervate, 4 g/L PDADMAC, in 20 mM TX100 I = 400 mM (NaCl), was titrated with 60 mM SDS (I = 400 mM NaCl) using a

2.0 mL Gilmont microburet to bring the solution to mole fraction SDS, Y =0.4. In order to form the PE-protein coacervate, BSA and PDADMAC were mixed together first in pH 5.0, I = 100 mM (NaCl) Milli-Q water to yield a solution 30 g/L in BSA and 6 g/L in PDADMAC. pH was then adjusted to 8.0 by the addition of 0.1 N NaOH. All three systems were brought to their respective coacervation states by adjustment of SDS content for the PE-micelle system, or pH for the protein-containing systems (see Figure 4.1). For protein-protein coacervate, LF and BLG were mixed to yield a solution of 20 g/L LF and 20 g/L BLG in pH 6.0 (no salt) followed by vortexing for 10 s. For each of the three systems, the resulting turbid suspensions of coacervate droplets were centrifuged (Beckman Coulter Allegra 6R) for 1 h at 4000 rpm, 20 °C to produce optically clear dilute (upper) and dense (lower) phases (supernatant and coacervate, respectively). The water content in coacervate (W_{H2O}), determined by comparing coacervate samples prior to and after freeze-drying, was 80%, 84% and 86% for LF/BLG, BSA/PDADMAC and Micelle/PDADMAC, respectively.

Differential Scanning Calorimetry (DSC) of Coacervates. Coacervate samples, 6-10 mg, were placed in hermetically sealable aluminum pans. Tests were run using a TA Instruments Q100 DSC equipped with an RCS cooling system in nitrogen, with a N_2 flow rate of 50 mL/min. Phase transitions of water were investigated by cooling the sample to −30 °C, equilibrating for 10 min and then heating to 30 °C at a rate of 5 °C/min, a heating rate that providing a good calorimetric response a to the physical phenomena occurring during the scan. On the basis of better instrument performance in heating mode, DSC analysis was performed only by imposing single heating ramps. Area of peaks and onset temperatures of melting were obtained automatically using Universal Analysis software from TA Instruments. The calibration of the instrument with pure water yielded the melting enthalpy of bulk water

(DH_w) as 323 J/g. The weight of freezable water (W_f) and non-freezing water (W_{nf}) were determined from integration of the endothermic peaks. W_f in coacervates can be determined as:

$$W_f = DH_c/DH_w \times 100\% \quad \textbf{(4.2)}$$

where DH_c is the melting enthalpy of water in the solution. W_f is used to determine W_{nf}:

$$W_{nf} = 1\text{-}DH_c/DH_w \times 100\% \quad \textbf{(4.3)}$$

In eqns (4.3) and (4.4) all the weight quantities denoting the different water states are relative to the total weight of water content.

4.4 Results & Discussion

Turbidimetric titrations were performed by addition of SDS to mixtures of PDADMAC and SDS/TX-100 mixed micelles, or NaOH to solutions of PDADMAC/BSA and BLG-LF, to determine regions in which LLPS occurs, leading to the formation of a second phase, indentified as the coacervate phase. The results are shown in Figure 4.1. Coacervation involving PEs requires *inter alia* charge neutralization of soluble complexes,[104] i.e.

$$Z_T = 0 = Z_{PE} + nZ_C \quad \textbf{(4.4)}$$

where Z_T is the total charge of the polymer chain with bound oppositely charged colloids, Z_{PE} is the charge of polyelectrolyte, Z_C is the charge of the colloid, either protein or micelle,

and *n* is the number of colloids bound per polymer chain, which depends on the affinity of the colloid for the PE, as represented by its binding constant. On the other hand, HPCs require a very precise balance of repulsive and attractive interactions in order for coacervation to occur, shown to be between pH 5.7-6.2 for BLG-LF HPCs.[113]

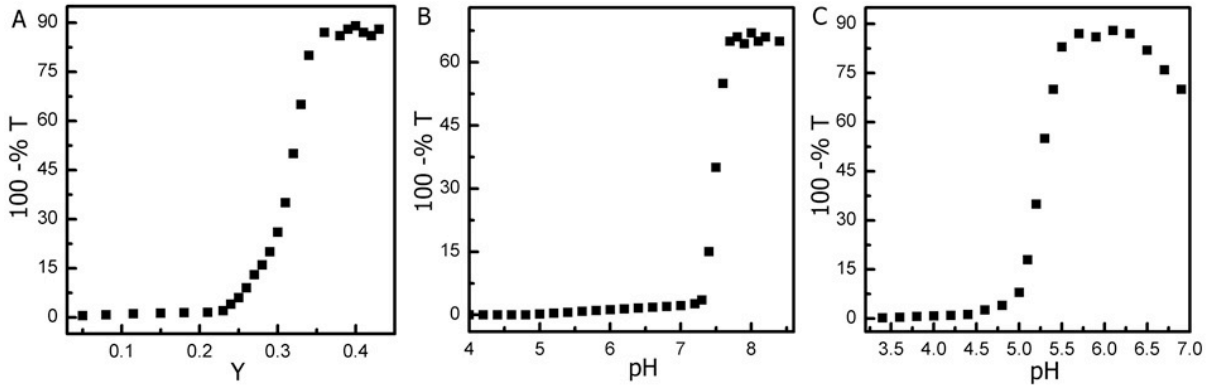

Figure 4.1: Turbidimetric titrations of **(A)** PDADMAC/micelle, **(B)** PDADMAC/BSA and **(C)** BLG-LF solutions. The onset of coacervation corresponds to the slope change, i.e. Y = 0.3 **(A)**, pH = 7.3 **(B)** and pH = 5.2 **(C)**.

4.4.1 DSC is Used to Extract NFW Content

Data obtained from heating scans for different coacervate samples (Figure 4.1) are summarized in Table 4.1. From the calorimetric traces (Figure 4.2) it can be observed that the endothermic melting peak is present for all coacervate samples. It is worth noting that coacervate samples display a DSC trace characterized by a single melting peak. This phenomenon can be attributed to the existence of only one type of freezable water. Each coacervating systems shows a different onset temperature of water melting (T_o), which is defined as the point of departure from the line of zero slope. PE-micelle coacervates gave the lowest T_o followed by PE-protein and HPC systems. The amount of *non-freezable water is* defined as the water amount present in the coacervate not associated with the endothermic

peak. It seems that PE-containing coacervates have similar W_t, W_f and W_{nf} regardless of the colloid. However, HPCs have lower W_f and higher W_{nf} than the PE-containing coacervates.

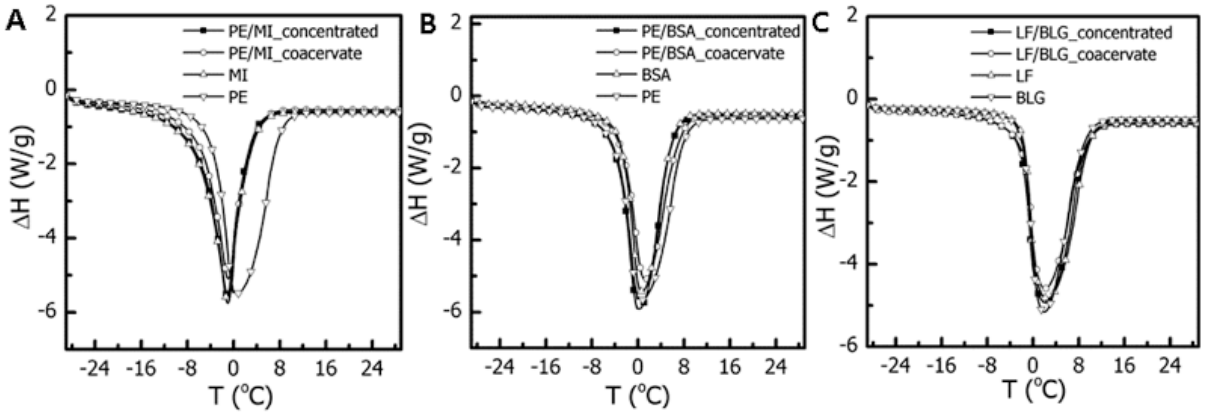

Figure 4.2: DSC scans of **(A)** PDADMAC/micelle, **(B)** PDADMAC/BSA and **(C)** BLG-LF samples.

4.4.2 NFW in Coacervates vs. Uncoacervated Mixtures

All coacervates were shown to have lower W_f and higher W_{nf} than uncoacervated mixtures of concentrated macroions prepared at concentrations equivalent to those in the coacervate. While the level of NFW is always higher in coacervates than in such concentrated one-phase samples, the difference is particularly notable for HPCs, which show a 5-10 fold increase in NFW.

Table 4.1: Freezable water (W_f), non-freezing water (W_{nf}) content for different systems.

	$W_{molecules}$ [a] (g)	DH (J/g)	W_f (wt%)	W_{nf} [b] (wt%)	$W_{nf}/W_{molecules}$ [c]
Concentrated LF/BLG	250	313±4	97±1%	3±1%	0.12±0.04
LF/BLG (coacervate)	250	273±7	85±2%	15±2%	0.6±0.1
LF	125	323±2	100%	0	0
BLG	125	322±2	100%	0	0
Concentrated BSA/PDAD	163	305±3	99±1%	1±1%	0.1±0.1
BSA/PDAD (coacervate)	163	276±6	90±2%	10±2%	0.6±0.1
BSA	130	293±3	95±1%	4±1%	0.3±0.1
PDAD	33	305±4	99±1%	1±1%	0.3±0.3
Concentrated Micelle/PDAD	190	286±4	96±1%	4±1%	0.2±0.1
Micelle/PDAD (coacervate)	190	273±6	92±2%	9±2%	0.5±0.1
Micelle	153	286±4	96±1%	4±1%	0.3±0.1
PDAD	37	292±3	98±1%	2±1%	0.5±0.3

[a] The weight of macromolecules per 1000 g DI water. [b] Percentage of non-freezing water relative to total water % NFW/(NFW+FW). [c] Weight ratio of non-freezable water (NFW) to macromolecules.

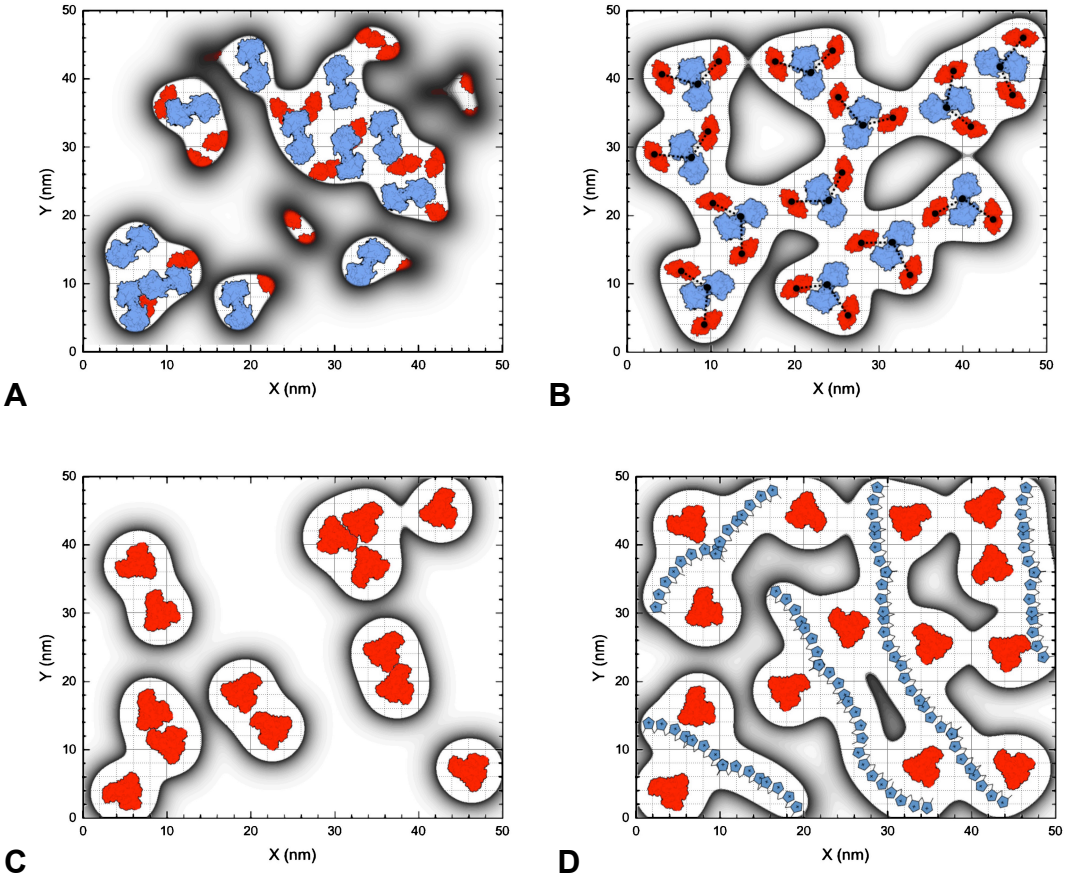

Figure 4.3: Representation of networks of hydration water in uncoacervated (**A,C**) and coacervated (**B,D**) protein solutions; visualized in a 50 nm × 50 nm plane with a thickness of 5 nm; assumes ca. 1.5 nm of hydrated water per protein. **(A)** 125 g/L LF + 125 g/L BLG_2, **(B)** 250 g/L $LF(BLG_2)_2$. **(C)** 130 g/L BSA, and **(D)** 37 g/L PDADMAC/ 130 g/L BSA

4.4.3 Role of Protein Hydration

The remarkable amount of NFW seen in the protein systems suggests that protein hydration is strongly affected by the coacervation process. This is most significant for BLG-LF coacervates, which have the largest value of NFW, and stands in contrast to the negligible amount of NFW for the free proteins. A similar, but smaller, effect is seen for the BSA/PDADMAC coacervate. It appears likely in both cases that, perhaps counter-intuitively, the number of protein-water contacts (i.e., level of hydration-water) is increased in the coacervates, relative to a control, which comprises the sum of concentrated BLG and LF

solutions. This could happen if protein-protein contacts are, in fact, diminished (i.e., replaced by protein-water contacts) in the coacervate. Figure 4.3 portrays this type of "structuration" in which electrostatic interactions between LF and BLG, on the length scale corresponding to average separations of ca. 1-2 nm between LF and BLG,[113] lead to an organization that in fact *reduces* intimate protein-protein contacts, thus enhancing protein-water contacts.

4.4.4 Structuration during the Coacervation Process

BLG-LF HPCs differ from simple concentrated protein solutions in multiple regards. Such factors include (1) the narrow range of preparation conditions (e.g., pH and *I*) that result in coacervation and (2) the existence of a well-defined structural unit, with a fixed stoichiometry. The large hydrodynamic volume occupied by the highly-hydrated coacervating species $LF(BLG_2)_2$ with R_g ca. 4-5 nm,[113] maximizes the number of protein-water contacts, compared with protein-alone solutions. Such concentrated proteins in uncoacervated samples, should have a large number of, unstructured, protein-protein interactions (e.g., aggregates or multimers), limiting the amount of possible protein-water interactions). Thus there is a significant structuration of water, relative to concentrated protein solution, when BLG_2 and LF are consolidated into a single primary unit, of limited flexibility that forms a structural unit of R_h ca. 4-5 nm, large enough to retain protein solvation shells.

For the BSA-PDADMAC coacervate, which exhibits the next largest NFW effect, inhibition of protein-protein contacts occurs by a different process, as shown in Figure 3D: protein-protein interactions are replaced by protein-polyelectrolyte interactions. A substantial body of literature demonstrates the reduction of rates of protein aggregation in the presence

of binding polyelectrolytes.[120, 121] This is also consistent with the notable observation that PDADMAC-BSA solutions with 200 g/L protein show no changes in DLS spectra even after extended storage at room temperature.[122]

Systems in which BSA is replaced with SDS/TX-100 micelles show NFW patterns that resemble those of the protein systems, but comparisons are greatly complicated by the very high ionic strengths required for formation of SDS/TX100/PDADMAC instead of precipitates. For this reason, and because of the very limited understanding of water structure in concentrated ionic micelle solutions, we hesitate to make comparisons with the protein systems.

4.5 Conclusions

An enhancement of nonfreezing water content was seen in several coacervating systems: LF/BLG (heteroprotein) coacervate; PDADMAC/BSA (PE-protein) coacervate; and a coacervate formed between PDADMAC and the anionic/nonionic (SDS/TX-100) mixed micelle. All coacervates were found to contain high levels of NFW, ca. 9-15% of total water. Comparisons to uncoacervated controls confirm that the coacervation process is responsible for maximizing protein-water contacts, i.e. NFW, in protein-containing coacervates. Compared to both PDADMAC/BSA and PDADMAC/micelle coacervates, heteroprotein coacervates have a higher percentage of NFW and a larger ratio of NFW to total macromolecule concentration. This can be attributed to a well-defined structural unit $LF(BLG_2)_2$ whose expanded configuration enhances protein-water contacts at the expense of protein-contacts. Similar compensating effects are responsible for a slightly lower NFW level of PDADMAC/BSA coacervates.

4.6 Acknowledgements

This project was supported by the National Science Foundation (CBET-1133289, CBET-0966923), and MRSEC in UMass-Amherst. We thank Prof. Ilja Voets for helpful discussions.

CHAPTER 5

PROTEIN CHARGE ANISOTROPY AND PHASE SEPARATION ROLE OF ELECTROSTATICS IN SELF-ASSOCIATON OF MONOCLONAL ANTIBODIES

Daniel Seeman, Paul L. Dubin *2015*, (In Prep)

5.1 Abstract

Turbidimetric self-association rates of mAb (%T min^{-1}) at low temperature, T = 11^{o}C show a maximum in disaggregation at pH < 7.5, when pH is adjusted from high-to-low. Titration with 4 M NaCl, at pH 4.5, results in a continuous increase in turbidity, leading to the appearance of so-called "opalescence". Antibodies centrifuged at T < 0^{o}C, at pHs 4.5 and 5.9 (C_p = 20 mg/mL) all underwent LLPS. The dense-phase was clearly identified, and a sharp interface between protein-rich and protein-poor phases was confirmed. Labeled "contaminant" protein (FITC-BLG) was found to be enriched in the dense phase, suggesting direct attractive interactions between BLG and mAb-1, which could be disrupted by changing pH prior to inducing LLPS of mAb.

5.2 Introduction

Liquid-liquid phase separation (LLPS) of monoclonal antibodies (mAbs), driven by the tendency of these proteins to self-associate under native conditions, can be exploited to separate mAbs from crude mixtures. The ability to design and produce novel protein-based pharmaceuticals such as mAbs has surpassed efforts to develop cost effective methods to purify and formulate.[123] Changes in pH and buffer composition[124] during purification have

been shown to produce a wide range of physical transitions, including liquid-liquid LLPS,[125, 126] solid-particle formation,[127, 128] crystallization,[128, 129] and finally precipitation.[125, 130, 131]

The phase separation temperature of such mAbs is strongly dependent on pH, and *I*. The predominant feature of mAb LLPS is the separation of a concentrated, single-component protein solution into two separate, well-defined aqueous layers without the use of solution additives. This transition is characterized by a well-defined upper critical solution temperature (UCST),[125, 132] below which self-association leads to separation into mAb-enriched and mAb-depleted aqueous phases. This depends strongly on pH,[125] with clear maxima at pH conditions that correspond to self-association.[133] Literature can be divided into two primary categories (1) those in which *simple* additives (salts and nonionic polymers) are used[125, 132] and (2) screens in which complex precipitants and solution additives are used.[128] While the latter are more common, it appears that the most important variables in these screens are ionic strength *I*, and starting protein concentration (C_p). Similar results can be obtained simply by varying pH, *I* and C_p.[125, 126]

Protein LLPS is an electrostatically controlled phenomena; strong dependence on pH and *I* points to an electrostatic cause of self-association. Increases in aggregation number,[134] and solution viscosity [133] in mAb formulations have been attributed to electrostatic attraction, regardless of the protein net charge. The protein charge patch,[12] *vis-à-vis* protein charge anisotropy,[12, 135, 136] has recently been attributed to the strong protein/protein interactions observed in high concentration solutions of mAbs.[137]

Non-cognate protein/protein interactions can be controlled via solution pH and ionic strength. Although much work has been done to minimize phase separation, recent work suggests that it should actually be possible to exploit this self-interaction to isolate mAb from

mixtures of host cell proteins (HCPs) and nucleic acids. LLPS of mAbs[125, 126, 132] can be induced at a wide range of pHs and ionic strengths, if T < 0°C incubations are used. This means that if solution conditions (pH, *I*) can be found where HCPs *do not* interact with the mAb of interest, it should be possible to selectively enrich one phase with mAb. Several cycles of LLPS could be used to vastly reduce the HCP:mAb ratio in the dense phase.

The goal of this work is to develop LLPS-based methods for purification of complex mixtures of mAbs (monomer, aggregate, and fragments), HCPs and host cell DNA, as well as other components of the culture media. Advantages of LLPS for purification would include (1) simplicity, (2) absence of expensive additives that need to be quantified, and (3) high levels of electrostatic selectivity. Turbidimetric pH-titrations, coupled with light-scattering and chromatographic analysis, will be used to identify conditions (pH, *I*, and C_p) of incipient phase separation at ambient T. Identifying conditions where interactions result in the formation of soluble clusters, should be predictive of phase separation at low T. Ultimately, enhancing mAb self-interaction and minimizing mAb/HCP interactions, should allow for optimal separation without the need for high MW additives that would require additional purification steps.

5.3 Experimental Section

Materials. A high isoelectric point therapeutic monoclonal antibody (mAb-1) was obtained from MassBiologics (Mattapan, MA). The mAb-1 lot used for this study was produced in CHO cells and purified over a protein A column. mAb-1 has a molecular weight of ca. 150 kDa and a pI of approximately 9.6, as determined by isoelectric focusing. Fluorescently labeled bovine β-lactoglobulin (BLG) (36 kDa) (Davisco Foods, Inc., batch number: JE 001-

8-415), was prepared by covalent labeling with FITC, as previously described.[88] Orange OT [1-(o-tolylazo)-2-naphthol] was purchased from Sigma-Aldrich, and Coomassie G-250 (Bradford dye) was obtained from Thermo Scientific; both were used without further purification.

Turbidimetric Methods. Turbidimetric autotitrations were performed by the addition of dilute (≤ 0.1N) titrant, NaOH (low-to-high) or HCl (high-to-low) to a solution of mAb-1, under constant stirring; all experimental variables (pH, transmittance, and time) were monitored simultaneously; ambient temperature was fixed at 11 °C. Transmittance was measured using a Brinkmann PC 800 colorimeter equipped with a 420 nm filter and a 1 cm path length fiber optic probe. Since the rate of pH change (dpH/dt) is known, the instantaneous rate of aggregation at any pH ($(d\tau/dt)_{pH}$) can be obtained from the product of ($d\tau$/dpH) and (dpH/dt).

Inducing mAb LLPS. LLPS experiments were conducted by adjusting mAb-1 to a target pH, at room temperature, prior to lowering to T < 0^{o}C, after which the samples were centrifuged allowing for gradual temperature increase. This is done at a two different mAb concentrations (50 mg/mL and 20 mg/mL) and three ionic strengths (I = 10 mM, 140 mM, and 270 mM). The interface can than be visualized upon addition of a small molecule dye, Orange OT, which is unable to diffuse into the (highly viscous) lower phase. The protein rich phase, for mAb alone experiments, is identified by the use of a protein-binding dye (Bradford Reagent) which changes color proportional to the amount of protein present.

Localization of Contaminant Proteins. Mixtures spiked with low concentrations of dye-labeled "contaminant" proteins with isoelectric points (pIs) and sizes comparable to HCPs are used to identify non-interacting conditions. FITC-tagged β-lactoglobulin (BLG), a model

"contaminant" protein with an isoelectric point (pI) around 5.2, is mixed and unlabeled mAb-1. The dyed "contaminant" located by visual inspection of the dense phase, post-LLPS. BLG would be an example of a strongly interacting contaminant protein. FITC-labeled BSA (pI ~ 4.9), should be representative of the low pI proteins typically encountered in mixtures of HCPs from the CHO K1 cell line.[138]

Computational Methods. DelPhi V. 4r1.1 was used to visualize electrostatic potentials around mAb-1, as a function of pH and *I*. A homology model of mAb-1 was constructed from sequence, using a typical IgG backbone as a template. Amino acid charges were calculated using a modified form of the spherical-smeared-charge model proposed by Charles Tanford.[4]

5.4 Results & Discussion

5.4.1 Self-Association Rates from Turbidity Titrations

Apparent self-association rates (%T min^{-1}) were extracted from a pH autotitration (Figure 5.1A) performed at a fixed rate of pH change, d(pH)/d*t*, showing a maximum in disaggregation, noted by the negative change in turbidity with time, at pH < 7.5 (from high pH), demonstrating the inherent reversibility of this process, which suggests an equilibrium system. Titration from low pH, starting at pH = 4.5, show that the rate of turbidity change, dτ/d*t*, reported in units of %T/min, is nearly constant, ca. 0.6 %T/min, until around pH 7, after which it drops sharply until pH 9, where it transitions to disaggregation. This indicates that mAb self-associates strongly as pH is increased; which must be due to attractive interactions; while at high pH (still pH < pI) repulsive interactions between mAbs are sufficient to disrupt aggregates formed at lower pH, maybe due to accumulation of charge on

such aggregates. However, once the direction of pH change is reversed, the turbidity change, $d\tau/dt$, increases to a rate nearly identical to that seen at low-pH in the low-to-high direction, ca. 0.6 %T/min. The rate crosses zero at a pH of 7.5, indicating a hysteresis with respect to titration direction, resulting from inequivalent mechanisms of aggregation and disaggregation. The rate of disaggregation remains constant, although, remarkably once $d(pH)/dt = 0$ at pH 4.5, the solution remains stably turbid, remaining at a τ of approximately 15% T.

5.4.2 Salt Titrations

Subsequent titration of mAb-1 with 4 M NaCl (Figure 5.1B), after having been adjusted from high-to-low pH at T = 11°C, shows a steady increase in turbidity, hinting at the existence of soluble precursors, which may ultimately lead to LLPS upon lowering of T. The rate of turbidity increase, $d\tau/d([NaCl])$ is approximately 1/20 mM^{-1}, up until a total *I* of 100mM NaCl is reached. Above this ionic strength, the magnitude of $d\tau/d([NaCl])$ drops to ca. 1/40 mM^{-1}. At this point the solution appears visually turbid in a manner consistent with literature reports of so-called "opalescence" in antibody solutions, and displays a complete lack of kinetics, even without continued stirring.

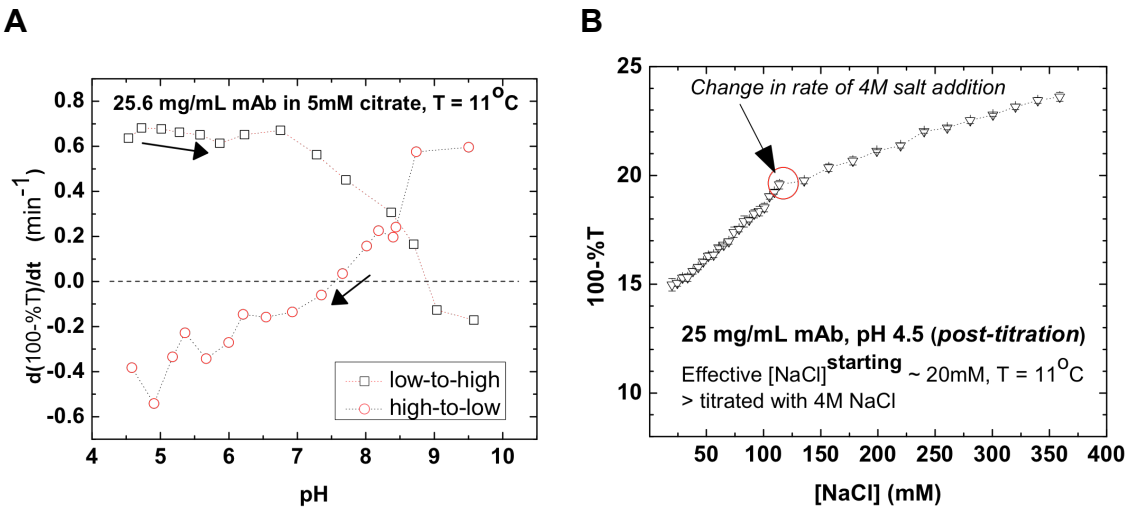

Figure 5.1: (A) self-association rates extracted from turbidimetric autotitrations at low T **(B)** titration of the same sample with 4 M NaCl leads to "opalescence", suggesting a precursor to LLPS.

5.4.3 LLPS after Centrifugation at Sub-Freezing Temperature

A 50 mg/mL solution of mAb-1 was adjusted to pH 4.5 in the absence of added salt, followed by addition of 4 M NaCl to a final *I* of 270 mM. The sample was cooled to T < 0°C, then centrifuged at room temperature allowing gradual warming while spinning (Figure 5.2). Orange OT was added to the upper phase in order to visualize the sharp interface between the high- and low- viscosity regions (Figure 5.2A). To verify that the bottom phase was protein-rich, 3uL of the lower (*right*) and upper (*left*) phases was isolated, and diluted in an equal volume of Bradford dye (Figure 5.2B). When transmitted light is blue shifted, it indicates the presence of protein, when it is red-shifted it indicates its absence. Neither phase is totally devoid of protein, but the shift towards purple for the upper phase versus a solid blue for the lower phase, demonstrates that the concentration of mAb in the lower phase is dramatically enriched relative to the upper phase.

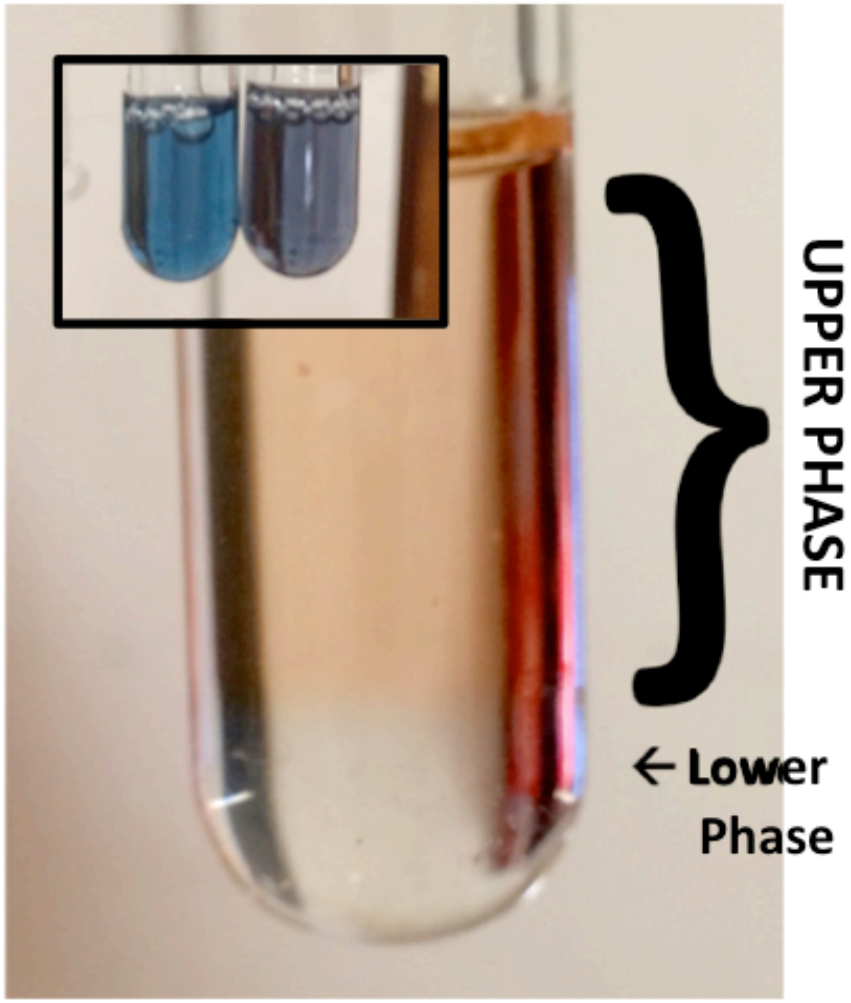

Figure 5.2: 50 mg/mL solution of mAb-1, 270 mM NaCl after LLPS. Orange OT added post-centrifugation. **(inset)** 3 uL of lower- (*left*) and upper- (*right*) phases, added to Bradford Dye. Lower phase is enriched with mAb-1.

5.4.4 Heteroprotein Interactions Persist During LLPS

Sample(s) prepared at pHs 4.5 and 5.9 with 20mg/mL mAb-1 were brought to I = 270 mM via addition of 4M NaCl (Figure 5.3). After LLPS, the samples containing only mAb-1 (*not shown*) form two discrete aqueous phases, as in figure 5.2A indicating that lower initial C_p does not inhibit LLPS. Identical samples, spiked with fluorescently-labeled "contaminant" protein (FITC-BLG), show nearly all dye-tagged protein (yellow) in the lower, mAb-rich, phase (Figure 5.3). This suggests that direct interactions between FITC-BLG and mAb-1 lead

to colocalization of the two proteins in the dense phase. Therefore, understanding charge-patch mediated protein-protein attraction will be useful in predicting overall separation efficiency.

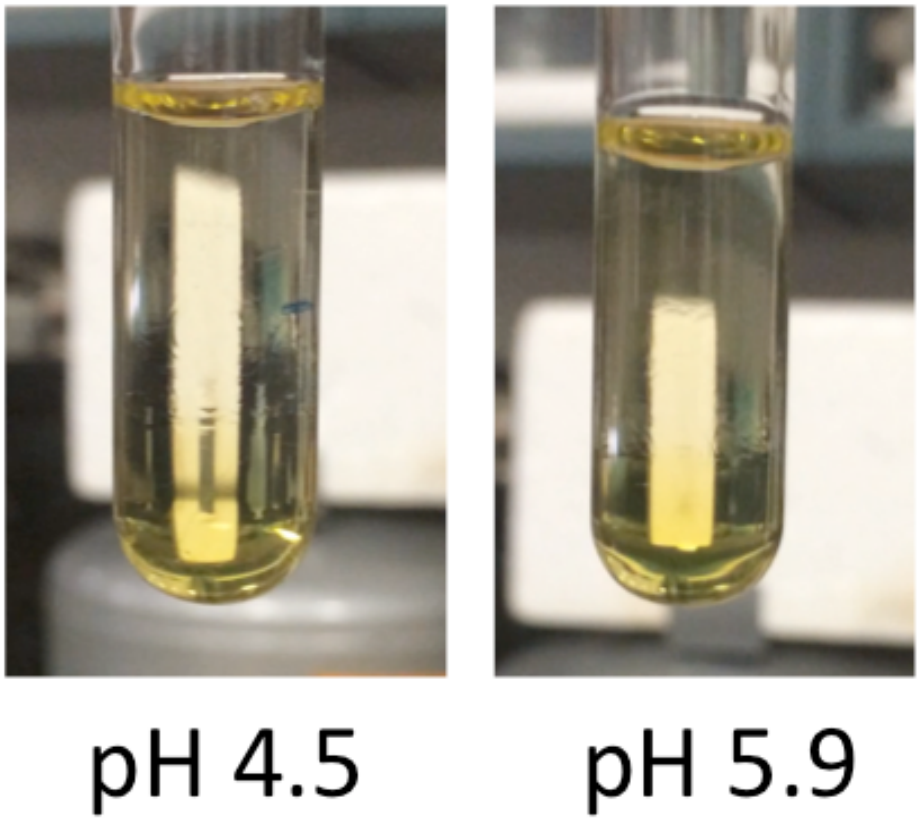

Figure 5.3: LLPS after incubation at T < 0°C. pHs 4.5 and 5.9 $[\text{mAb-1}]^{\text{final}}$ = 20 mg/mL, I = 270 mM spiked with FITC-β-lactoglobulin.

Quantitative electrostatic modeling of mAbs is used to visualize charge anisotropy as a function of pH and I (Figure 5.4). Electrostatics is relevant to both (1) self-association leading to LLPS and (2) mAb/HCP interactions leading to either retention or exclusion of "contaminants". Even at pH < pI substantial variation in protein charge anisotropy, or "patchy-ness", is observed as a function of pH. This observation suggests that strong electrostatic attraction, between mAb monomers is still possible at pH << pI.

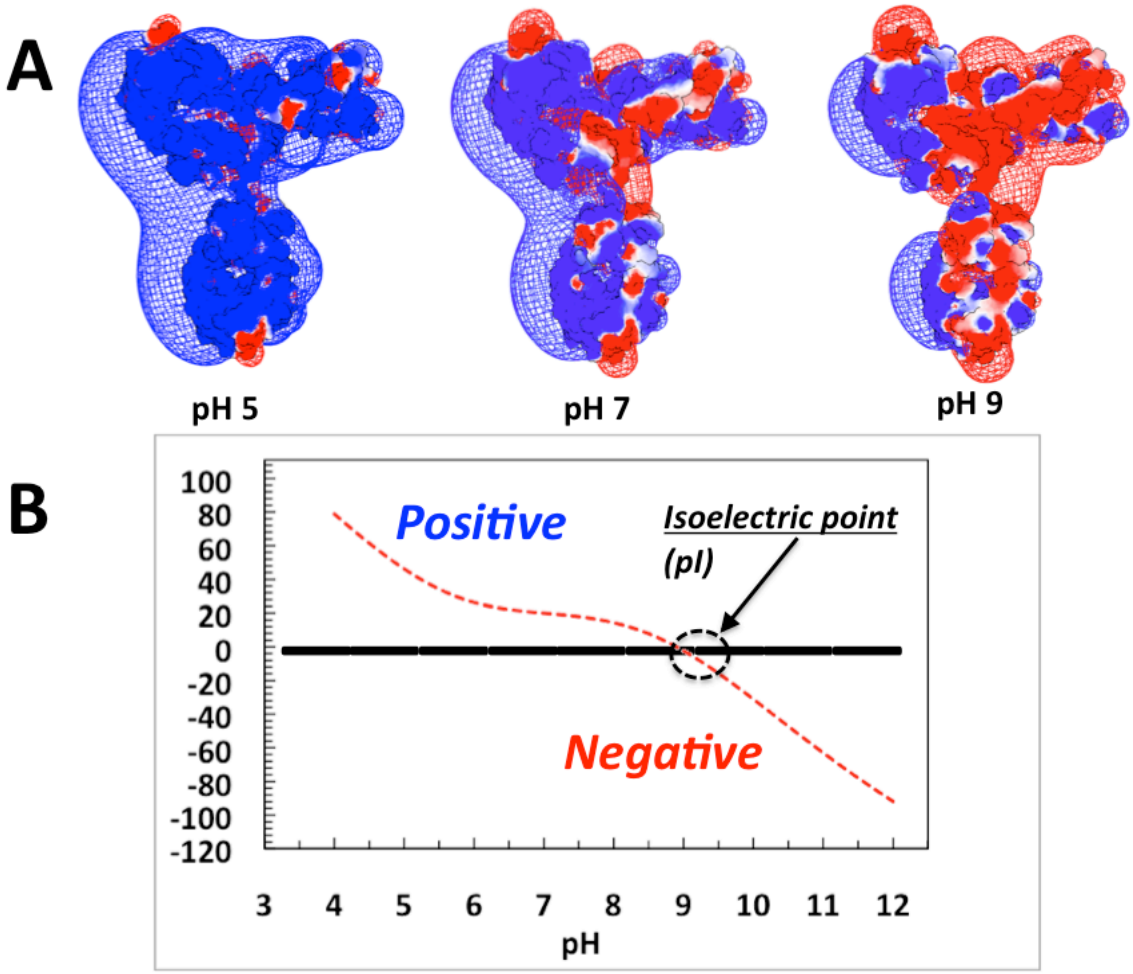

Figure 5.4: (A) Electrostatic potentials of mAb-1 at pH 5, 7, and 9, at I = 0.025 mM. ± 0.5 kT/e **(B)** computed charge curve.

5.5 Conclusions

Phase separation occurs readily at T << UCST for C_p ~ 20 mg/mL. These are low relative to current literature on LLPS, and show that LLPS is not impeded by low C_p "contaminants". pHs where electrostatic attraction between mAb and such model contaminant(s) is minimized, can be used to reduce the amount of non-mAb protein in the dense phase. Since both phases are water rich, the dense phase could be easily harvested for subsequent rounds of LLPS. Since the behavior of mAb monomer is driving phase separation, it will be possible control the depletion or enrichment of model proteins, or more

generally HCPs, by controlling the attractions between mAb and HCPs. Direct knowledge of mAb electrostatics, will be useful in predicting conditions that lead to self-association. It is conceivable that such work could eventually allow for the design of future mAbs optimized for purification efficiency as well as formulation stability. This suggests that solution conditions (pH and *I*) could be established where LLPS provides separation of crude mixtures into a mAb-rich and HCP-poor dense phase.

5.6 Acknowledgements

This research was supported by the National Center for Advancing Translational Sciences, National Institutes of Health, through Grant UL1TR000161. The content is solely the responsibility of the authors and does not necessarily represent the official views of the NIH.

CHAPTER 6

COACERVATION OF MONOCLONAL ANTIBODY WITH HYALURONIC ACID: METHODS FOR ASSESSING COACERVATE YIELD AND SELECTIVITY

Daniel Seeman*, Alexander J. Malanowski, Rachel Wollacott, and Paul L. Dubin *2015*,

(To be Submitted)

*corresponding author

6.1 Abstract

A method was developed in order to determine the yield and selectivity of coacervates prepared from monoclonal antibody (mAb) and hyaluronic acid (HA). The yield of mAb, in such coacervates, is shown to be as high as 80%, with final concentrations of mAb-A > 170 mg/mL. Size-exclusion chromatography with multi-angle laser light scattering detection (SEC-MALLS) shows that, at r = 10 (i.e., a 10X excess of mAb:HA), the yield of HA is ca. 75%. Removal of HA by ultrafiltration should be easily accomplished. All but one sample, show complete separation of bovine serum albumin (BSA) from mAb, with the two proteins going into the supernatant, and coacervate phase, respectively.

6.2 Introduction

Monoclonal antibodies (mAbs) are currently of major pharmaceutical importance, but their industrial-scale purification involves a complex array of separation techniques, predominantly expensive and time-consuming chromatographies. This has led to a search for effective non-chromatographic separations whose selectivity has been demonstrated largely

by trial and error. Unlike other forms of liquid-liquid phase separation (LLPS), PE-induced complex coacervation attains high yields and selectivity, based on well-understood effects of solution conditions, and protein and polyelectrolyte properties. The particular benefits of this approach have been recently established with the biocompatible natural polysaccharide hyaluronic acid (HA). Effective analytical methodologies are required to assess the yield and selectivity of this approach for purification of mAbs, particularly conducive to the analysis of coacervates formed with HA. High molecular weight HA was selected as a coacervating agent based on recent success in separating two proteins of similar pI.[139]

Although monoclonal antibodies have emerged as one of the most prevalent biotherapeutics,[131, 140] representing a large investment in the production of biologics, the principal challenge arises from purification, typically involving an array of separation techniques.[141] A typical mAb purification consists of cell clarification, affinity chromatography capture,[142, 143] and multiple ion-exchange chromatography steps.[144, 145] Cell clarification based on either centrifugation or microfiltration involves the removal of intact cells, cellular debris, and other generally insoluble components of the culture media, while protein A affinity chromatography,[146] by far the most effective but expensive part of the process, is used to selectively capture and concentrate mAbs. Overall production challenges stem from the large number of coupled and labor-intensive chromatographic steps.[131, 141] Thus the development of effective non-chromatographic purification methods has been an ongoing objective.

Coacervation is known to be a nondestructive and concentrating technique for inducing phase-separation (LLPS) of target proteins, and thus shows great promise for use in purification of mAb. Coacervates form when complexes of oppositely charged

macromolecules, in this case protein and polyelectrolytes (PE), form a new dense phase enriched in protein. Coacervates formed from complexes of PEs and proteins remain aggregate-free, and have been shown on numerous occasions to preserve enzyme activity. Such coacervating systems have been used to deliver proteins such as growth factors,[147] vaccines,[148] and plasmids;[149] or as templates for scaffolds.[150, 151] Until recently, the failure to recognize the remarkable potential for selectivity in PE-protein coacervation has been an obstacle to applying this uniquely powerful separation process to mAbs.

PE-protein coacervates are reversible equilibrium fluids, in which proteins at high concentrations remain aggregation-free, and retain structural integrity and activity. Regardless of starting concentrations, PE-protein coacervates are dense, optically clear fluids typically containing ca. 200 mg/mL protein, 30-50 mg/mL PE, and 70-80 % water at the initial ionic strength (*I*).[20] There is no evidence of any time dependence, and enzymes encapsulated in coacervate droplets have been demonstrated to retain enzymatic activity.[152, 153] Low-speed centrifugation easily separates the protein-rich coacervate from its supernatant, providing a simple mechanism to separate mixtures containing multiple proteins with different affinities for the coacervating PE.

Coacervation of hyaluronic acid (HA) with model proteins BSA and BLG allowed for separation of the two component proteins, however a higher degree of selectivity would be required for purification of mAbs. Coacervation and separation of model proteins BSA and BLG with HA has been published previously.[139] This work focused on construction of phase-boundaries for protein/PE coacervates, allowing for separation of two proteins with similar pIs by selective phase separation. One challenge in applying this method to the purification of mAbs, is the high degree of selectivity required in a production environment, as well as

the development of methods for detecting and quantitating mAb, HA, and model impurity BSA in the resultant coacervate phase.

Precipitation of mAbs with anionic polyelectrolytes (PEs) has been shown to provide a limited degree of selectivity for mAb,[154, 155, 156, 157, 158] although such methods are not ideal. The ability to recover active mAb in this way[131, 154, 159] depends on the degree to which the dense phase is solid- versus liquid-like. Extensions to other proteins or conditions are impeded by the absence of underlying principles for a process often involving complex kinetics, as well as ambiguity about the exact nature of the dense phase.[154, 156, 157] Much of the literature addresses incremental variations in already established purification "platforms" among well-established methods for purifying biologics, with results often reported in terms of log enrichment of mAb, or log depletion of a particular impurity.[160, 161] Uncertainties, resulting from redissolution and quantitation of dense phases, are reduced when the PE-protein interaction leads to a well-defined equilibrium dense liquid, i.e., coacervate.[20, 70] However, protein/PE coacervation has not hitherto been applied to mAb purification.

In this work we assess the yield and selectivity of the coacervate phase, in order to (1) establish the suitability of mAb/HA coacervation as a replacement for existing chromatographic methods, and (2) develop a method for assessing the success of particular conditions of pH and I in separating mAb from low pI impurities. In this case, BSA was taken as a model impurity, meant to be an analog to Chinese Hamster Ovary (CHO) host cell proteins,[143] the majority of which have low pIs.[138] Coacervates were prepared containing ternary mixtures of mAb, BSA, and anionic polyelectrolyte HA, and subsequently analyzed using size-exclusion chromatography (SEC) with multi-angle laser light scattering detection

(MALLS) and strong cation-exchange chromatography (SCX). While removal of HA is not explicitly addressed, analytical procedures for its quantitation are demonstrated.

6.3 Experimental Section

Materials. SZE grade sodium hyaluronate (HA), from Shiseido, Lot No. A07A, $[\eta] = 2.6$ m^3/kg, was used without further purification. A high isoelectric point therapeutic monoclonal antibody (mAb-A) was obtained from MassBiologics (Mattapan, MA). The mAb-A lot used for this study was produced in CHO cells and purified over a protein A column. mAb-A has a molecular weight of 147.6 kDa and a pI of approximately 9.6 (determined by isoelectric focusing).

Turbidimetry. Turbidity was measured at ambient temperature (T = 21-24 °C) with a Brinkmann PC800 colorimeter equipped with a 1 cm path length probe, and a 470 nm filter. For pH titrations, dilute NaOH was used to adjust the pH of mAb (1 mg/mL) and HA (0.1 mg/mL) stock solutions to pH 8, prior to mixing in equal parts. The final concentrations were 0.5 mg/mL MAb-A, and 0.05 mg/mL HA resulting a 10:1 excess of mAb on a weight basis (r = 10). The solution pH was then lowered by controlled addition of dilute 0.01 N HCl solution, which was added dropwise from a microburet under constant stirring. Both pH and transmittance (%T) were recorded after each addition of titrant, allowing sufficient time for the solution to reach equilibrium. Titration is continued until redissolution of coacervate, facilitated by loss of HA charge at acidic conditions, is observed at low pH. All stock solutions were prepared in I = 0.025 M NaCl. Residual buffer from mAb formulation is < 1 mM by dilution. For comparison a control titration is conducted in the absence of HA.

Preparation of Coacervates. In order to analyze the composition of the coacervate, 40 mL of sample was prepared using a final mAb concentration of 0.5 mg/mL, $r = 10$. Samples were prepared at I = 5, 10, 25, and 50mM NaCl, and pHs 7.9, 7.6, 7.2, and 5.2; corresponding roughly to the pH of maximum turbidity for each ionic strength. In each case the sample was adjusted down from a non-interacting pH using dilute (< 0.1 N) HCl, and then centrifuged at 4100 rpm for 60 minutes at T = 21°C. The supernatant was then isolated from the coacervate (dense phase) by decanting. For SCX analysis the coacervate was then entirely redissolved in phosphate buffer, containing 1 M NaCl, then diluted to a final salt concentration of 50 mM NaCl prior to injection.

Size-Exclusion Chromatography. Supernatant from a coacervate prepared at $r = 10$, $I = 25$ mM, centrifuged at pH 7.2-7.3, was analyzed directly by size exclusion chromatography (SEC) using a TOSOH TSK-G3000SW_{XL} column, run on a waters HPLC, using a model 410 differential refractometer (dRI), and an on-line multi-angle laser light scattering (MALLS) detector (Wyatt Technology). Samples were run in 20 mM phosphate, pH 7, 500 mM NaCl with < 1% NaN_3. For each run samples were injected manually using a 100 uL loop, and run at a flow rate of 1 mL/min unless otherwise indicated. Using SEC mAb is only partially resolved from model impurity BSA. The refractive index increments (dn/dc) for protein[18] (mAb or BSA), and HA[162] were taken to be 0.185, and 0.11 mL/g respectively. Concentration of HA remaining in the dense phase, and by extension yield of HA in coacervate, is estimated from dRI signal, using dn/dc to determine the total amount of HA injected in 100 uL of supernatant.

Cation-Exchange Chromatography. Samples were run on an HPLC 1090LC, using a diode-array detector (DAD) set to collect traces at 280, 254, 230, and 214 nm

simultaneously. Standard curves relating peak-height (mAU) at the selected wavelengths were generating by injecting 100 uL of sample, for a concentration series of mAb-A and BSA stock solutions (prepared by serial dilution) onto a Pharmacia HR 5/5 strong cation-exchange (SCX) column, using a flow rate of 2 mL/min and a step gradient (Buffer A = 0 M NaCl, pH 8 phosphate / Buffer B = 1 M NaCl, pH 8 phosphate). BSA (negatively charged at pH 8) elutes prior to increasing % of Buffer B (t = 0.4 min), whereas mAb-A is retained until a moderately higher %B (t = 2.2 min). Each sample is injected 2X.

6.4 Results & Discussion

Type I titration of mAb with HA (Figure 6.1, black open squares) at an ionic strength (*I*) of 0.025 M show that complexation must occur at pH < pI. Solutions of basic protein, mAb-A, with anionic polyelectrolyte, HA, below the protein's isoelectric point results in a stable, non-interacting solution. Once the mixture is lowered to below ca. pH 7.6, the system abruptly undergoes LLPS (Figure 6.2A). Titration of mAb-A alone (Figure 6.1, red open circles) shows very minimal pH-dependent self-association, thus the turbidity increase seen in the presence of HA must result from interactions with the target mAb. Centrifugation of a large volume of coacervate prepared at pH 7.2 – 7.3 and I = 0.025 M shows the formation of a characteristic highly viscous, dense-fluid phase (Figure 6.2B).

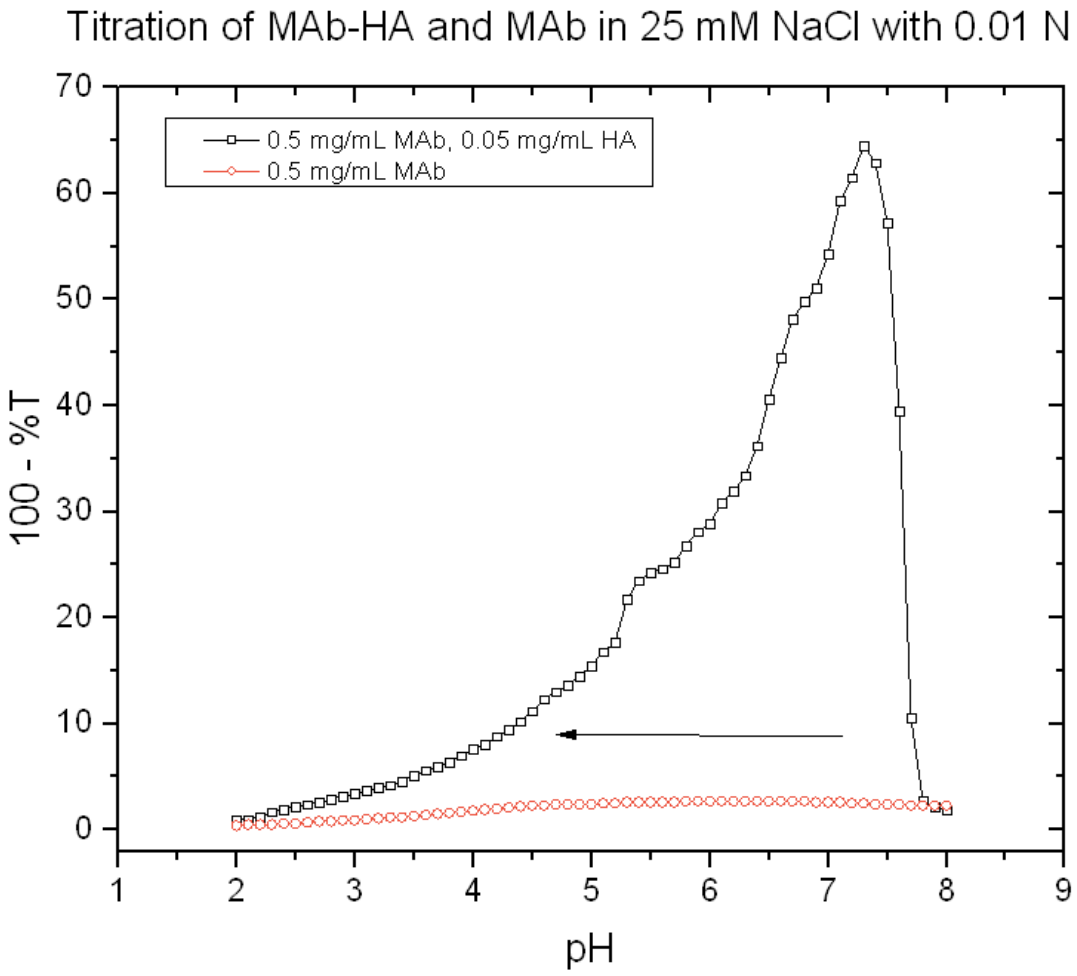

Figure 6.1: Turbidimetric pH titration of a mAb/HA mixture **(black)** from a non-interacting pH (8.0). As the pH of the solution is lowered, an attractive interaction between mAb and HA begins, and phase separation occurs. The onset of phase separation is easily and reproducibly determined by measurements of turbidity. A control experiment is preformed using mAb alone (red), showing minimal self-association of mAb in this pH range.

Although it will be shown that mAb-A is largely absent from the supernatant, quantitation of the coacervate dense phases still requires a method for fully resolving the components of a ternary mixture of mAb, BSA (a model impurity) and HA, which conveniently elutes near the column void volume. Coacervate prepared at I = 0.025 M, pH 7.2, corresponding to the region of maximum turbidity (Figure 6.1), was analyzed by SEC with online multi-angle laser light scattering (MALLS) detection (Figure 6.3B). In high salt,

500mM NaCl, used to screen electrostatic interactions with the column packing, the elution peak of MAb-A (Figure 6.9) partially overlaps with those of BSA multimers, mainly dimer (Figure 6.8).

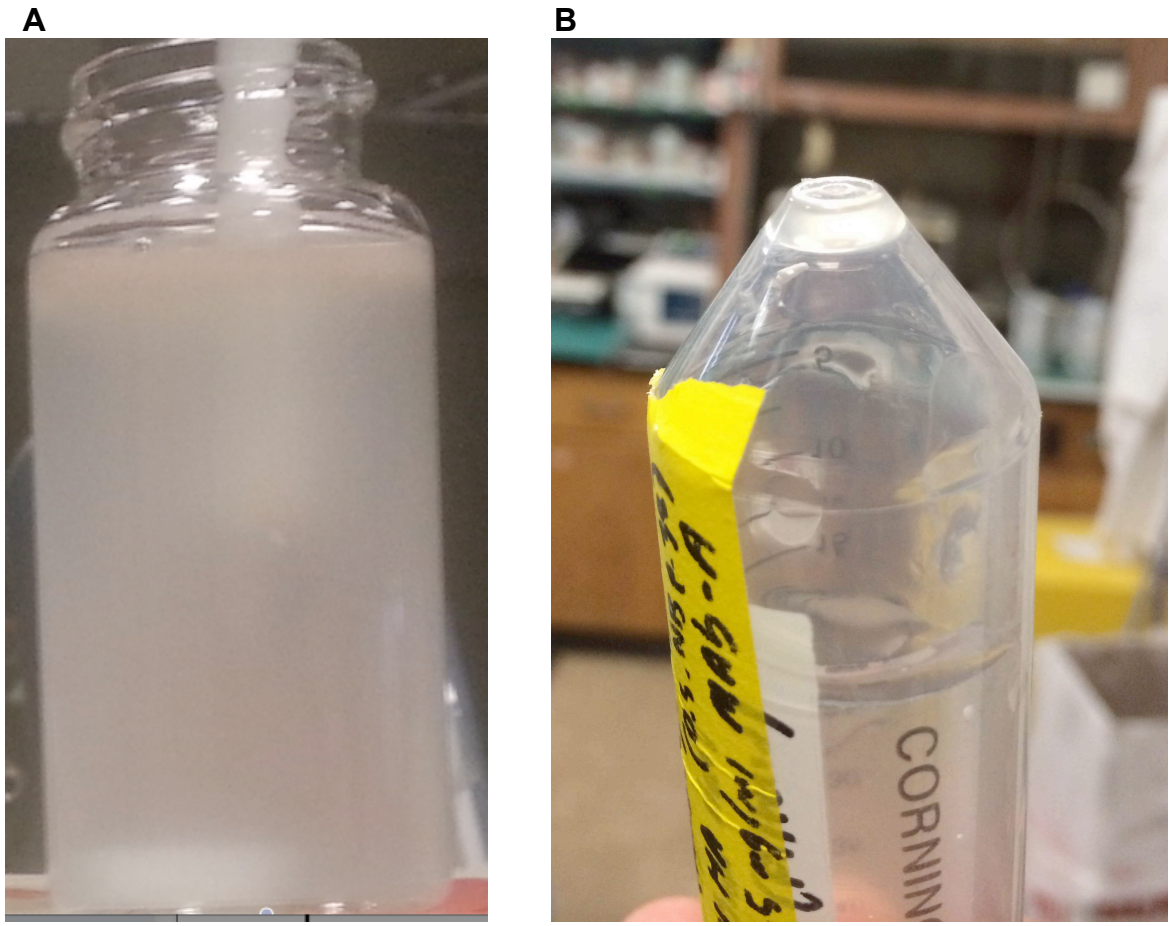

Figure 6.2: Photograph of a mAb/HA mixture at pH 7.3 (the maximum in turbidity) **(A)** prior to centrifugation (**B)** *post*-centrifugation, after supernatant has been removed/decanted and centrifuge tube inverted. Note the dense coacervate phase is a viscous liquid (*top*).

Supernatants of mAb/BSA/HA coacervates, prepared at ca. 25 mM NaCl, appear to be selectively depleted of both mAb-A, and higher molecular weight HA chains. Depletion of HA determined from the dRI trace suggests a coacervate yield of HA ca. 75%. Previous studies[163, 164] have reported the efficiency, of polycation (e.g., PDADMAC), in coacervating proteins of various pIs, as well as the effect of polyelectrolyte molecular weight (i.e., high

molecular weight PEs have a higher affinity for protein).[163] This suggests that the ca. 2.5X reduction, in apparent molecular weight, of the post-coacervation void peak (Figure 6.3B), relative to an injection of HA alone (Figure 6.7), may be due to selective incorporation of larger HA chains, into these coacervates.

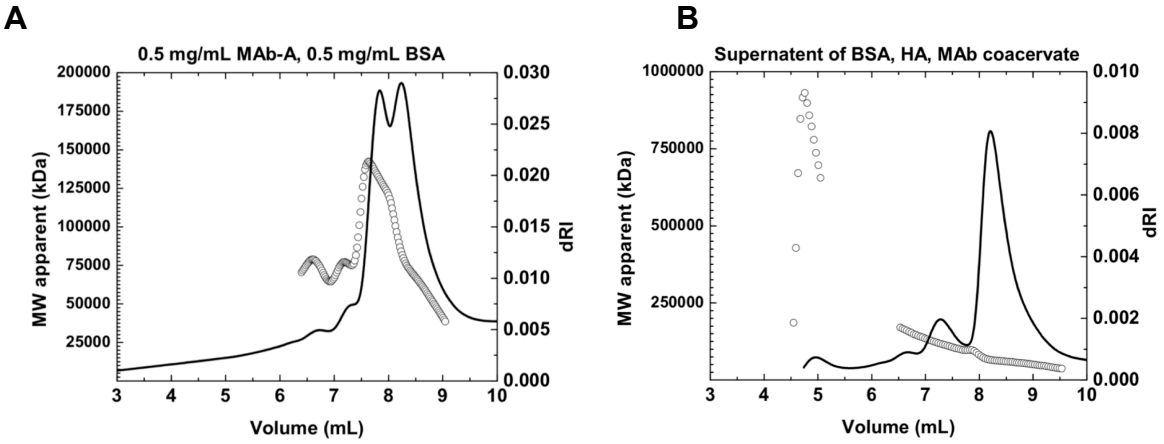

Figure 6.3: SEC MALLS, with TOSOH TSK G3000SWXL, using dRI and LS detection. Peak elution volume assignments V_e = 5.1, 6.8, 7.3, 7.8 and 8.4 mL: HA, BSA trimer, BSA dimer, MAb-A and BSA monomer, based on solo injections (6.7, 6.8, 6.9). **(A)** 1:1 mixture of MAb-A and BSA **(B)** supernatant of mAb/HA/BSA coacervate prepared at pH 7.3, *I* = 25mM.

This makes direct determination of protein concentration challenging; however relative amounts can be determined by comparison with injections of known mixing ratio. A 1:1 mixture of mAb-A and BSA (Figure 6.3A) was run to facilitate comparison with the more complex ternary mixture. Relative to the starting solution, the supernatant appears, both from dRI and light scattering traces, to be nearly entirely depleted of mAb-A without any apparent diminution of the concentration of serum albumin in the supernatant. This suggests that after centrifugation the majority of mAb is in the coacervate, while model impurity BSA remains in the supernatant (Figure 6.3B). Direct analysis of the coacervate requires a separation method that can resolve mAb from low pI model impurities.

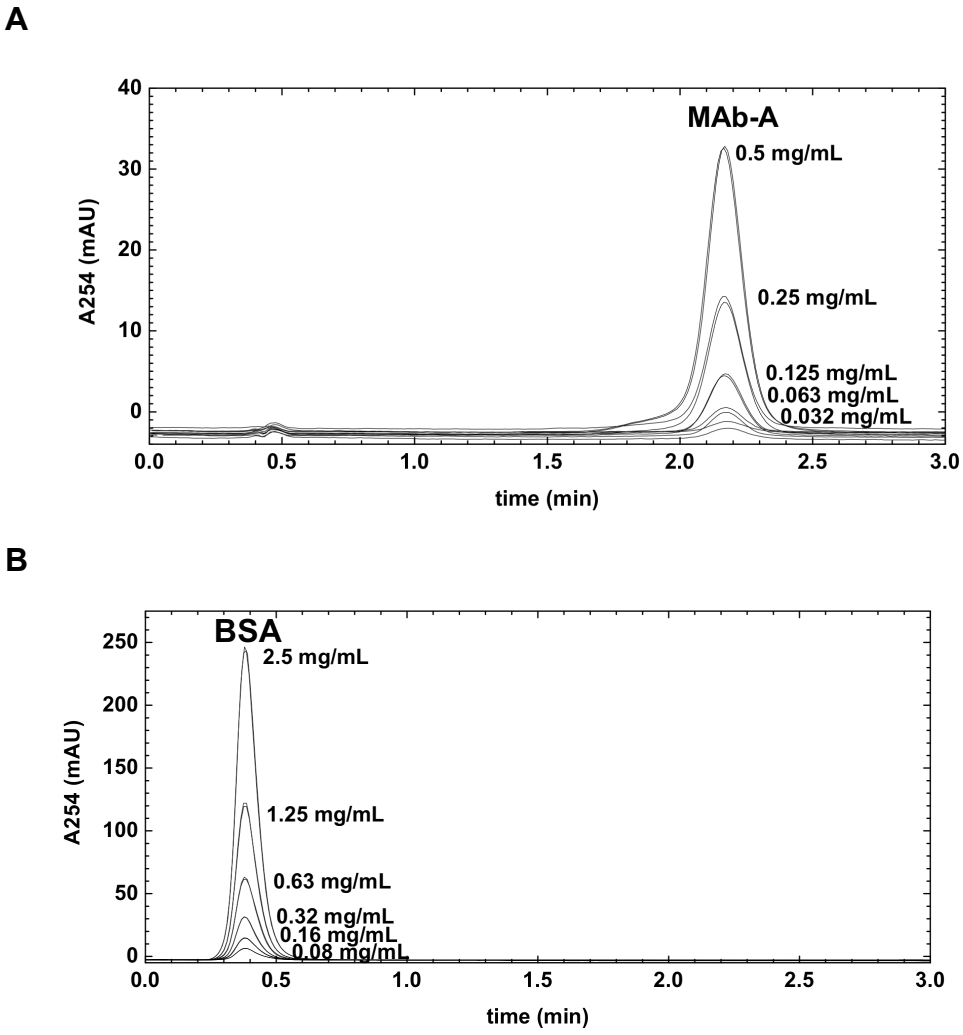

Figure 6.4: Strong cation-exchange (SCX) chromatograms (254 nm detection) of **(A)** mAb-A and **(B)** BSA used to construct calibration curves (Figure 6.5A,B). Including those obtained at 280, 230, and 214 nm.

6.4.1 Ion-Exchange is Able to Resolve BSA from mAb-A

Analytical ion-exchange chromatography allows separation of BSA and mAb, arising from differences, in protein net charge, and protein charge patches.[165] Solo injections of BSA and mAb-A onto a SCX are separated from each other by several column volumes (Figure 6.4), indicating ease of resolution. Detection at 254 nm minimizes the signal of HA, which elutes close the elution volume of anionic BSA. To facilitate concentration determination, all

injection volumes were fixed at 100 uL. All samples were prepared at a fixed *I*, ca. 50 mM NaCl, including standards (e.g., serial dilutions of mAb-A and BSA), and redissolved coacervates.

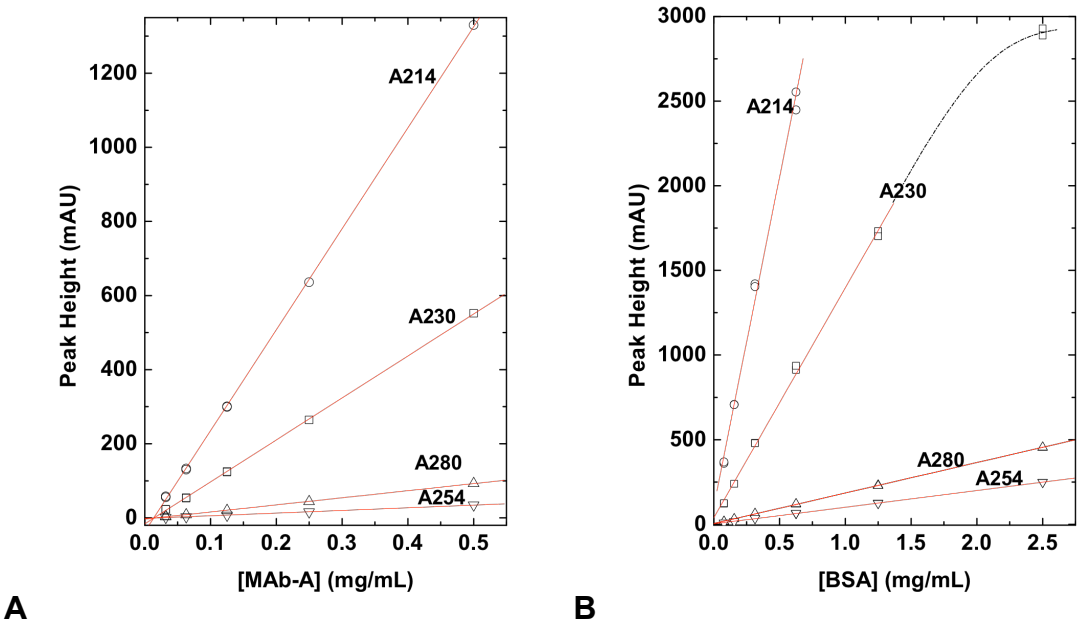

Figure 6.5: Injection of mAb-A onto HR 5/5 S-column. Calibration curves constructed for **(A)** mAb-A (elutes at 2.2 min, run at 2 mL/min), and **(B)** BSA (elutes at 0.4 min, run at 2 mL/min). Concentration determination is at four wavelengths (280, 254, 230, and 214 nm). Detector saturation occurs at peak heights above approximately 2800 mAU (*dashed line*).

6.4.2 mAb-A/HA Coacervates Are Mostly Free of BSA

As shown in Figure 6.6, removal of BSA from mAb-A occurs following coacervation at pH ≥ 7.2, and the corresponding ionic strengths $I \leq 25$ mM. At lower pH, corresponding to protein charge states sufficient to overcome screening by high salt, the interaction of BSA with HA may no longer be negligible. At pH 5.2, the peak intermediate to BSA and mAb could be assumed to result from direct interactions between mAb-A and BSA, which are oppositely charged at the pH of redissolution. Comparison with phase boundaries for

BSA/HA[139] suggest that pH 5.2 is close enough to pH_{φ} for BSA with HA that slight variations in preparation pH may result in coacervates either enriched in, or devoid of, BSA.

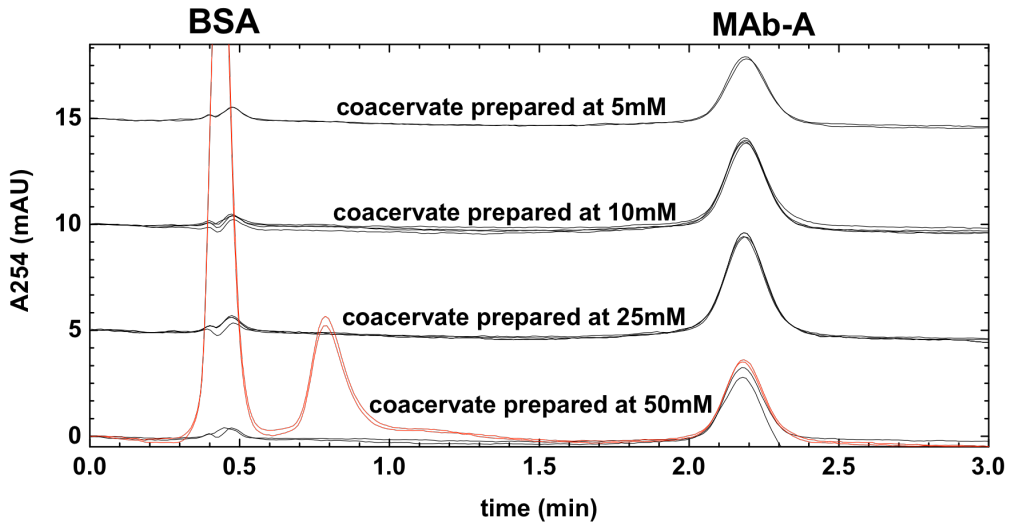

Figure 6.6: Strong cation-exchange (SCX) chromatography of redissolved coacervates prepared at varying ionic strengths and pHs: 5, 10, 25 and 50 mM; and 7.9, 7.6, 7.2 and 5.2. HA is not detected at 254 nm. The peak at 0.8 minutes corresponds to neither free BSA, nor to free mAb.

Table 6.1: Yields of mAb-A in coacervates prepared at pH of turbidity maxima

	5mM	10mM	25mM	50mM	< Yields (%MAb-A)
Mass% mAb in coacervate	60%	74%	83%	69%	
Standard Deviation	0.4%	1.7%	0.8%	1.4%	

The yield, defined as the mass% of mAb in the coacervate, determined by analysis at detection wavelengths of λ = 214, 230, 254, and 280 nm. Standard deviations represent variance between yields calculated using both trials *and* all four detection wavelengths. 50 mM trial 2 data (from Figure 6, red) was omitted in this analysis.

6.4.3 Optimizing Selectivity Requires mAb/HA Phase Boundaries

The yield of mAb-A is shown to be highest at I = 25 mM, however this could be further improved by optimizing either mixing ratio, or pH. For all permutations of I and pH the yield was shown to be no lower than 60%, and as high as 83% at r = 10 (Table 6.1), although it is not yet known if this is the optimal mAb:HA ratio. In order to achieve both optimal yield *and* selectivity it is clearly necessary to consider the phase boundaries of not just mAb, but also of the impurity protein(s).

6.5 Conclusions

HA, an injectable anionic polysaccharide, is used to induce selective coacervation, with the target mAb (e.g., mAb-A). Yields are assessed by, (1) SEC-MALLS analysis of supernatant, and (2) direct analysis of redissolved coacervate phases, using analytical SCX. The yield of mAb-A, determined from SCX, is high > 80% by mass, where the concentration of mAb-A in dense phase is ca. greater than 170 mg/mL. At a single mixing ratio, r = 10, it is shown that the yield of anionic polyelectrolyte (e.g., HA), in the coacervate, is ca. 75%. The process of coacervation, for mAb-A/BSA/HA mixtures coacervated at I = 25 mM, involves selective enrichment of higher molecular weight PE chains in the dense phase, which may facilitate removal of HA by ultrafiltration. In contrast to methods relying on protein/PE precipitation, mAb/HA coacervates have been shown to be easily redissolved, by adjustment of I or pH, allowing recovery of monomeric mAb, and finally providing a high degree of selectivity (i.e., coacervation of mAb, without any detectible “impurity” proteins). Of all combinations of preparation conditions (i.e., pH and I) examined, only coacervates prepared at I = 50 mM NaCl and pH 5.2 show any detectable BSA in the coacervate. Future work will

involve mapping out optimal conditions (pH, *I*, and r) for separation of mAb from low pI "contaminant" proteins, which will be facilitated by construction of a phase boundary, relating these variables.

6.6 Acknowledgements

This research was supported by the National Center for Advancing Translational Sciences, National Institutes of Health, through Grant UL1TR000161. The content is solely the responsibility of the authors and does not necessarily represent the official views of the NIH. Alexander J. Malanowski acknowledges a Jack Ragle Summer Research Fellowship in Chemistry from the University of Massachusetts-Amherst.

6.7 Supporting Information:

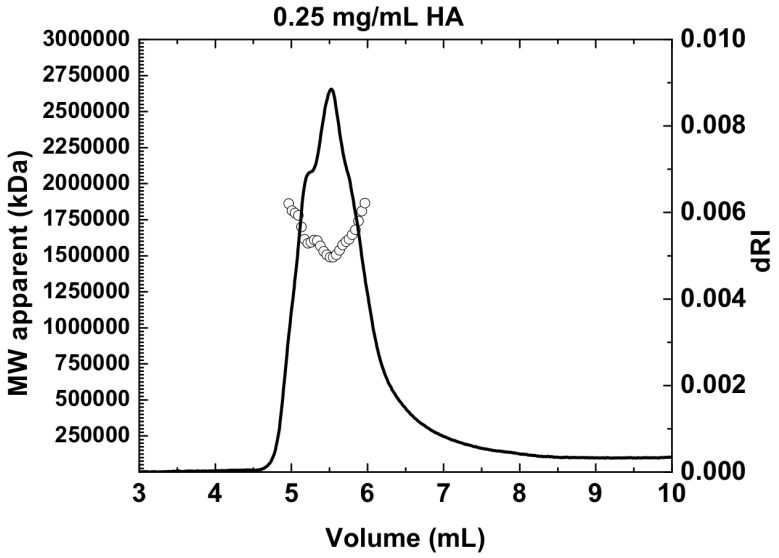

Figure 6.7: SEC-MALLS of HA alone using TSK G3000SW$_{XL}$ at 1 mL/min. Run at pH 7, 500 mM NaCl, 20 mM phosphate, dRI trace (right-axis), calculated MW (open symbols). Measured dn/dc for HA is 0.11 mL/g, [HA] = 0.25 mg/mL. V_e = 5.1 mL (void) and 5.5 mL.

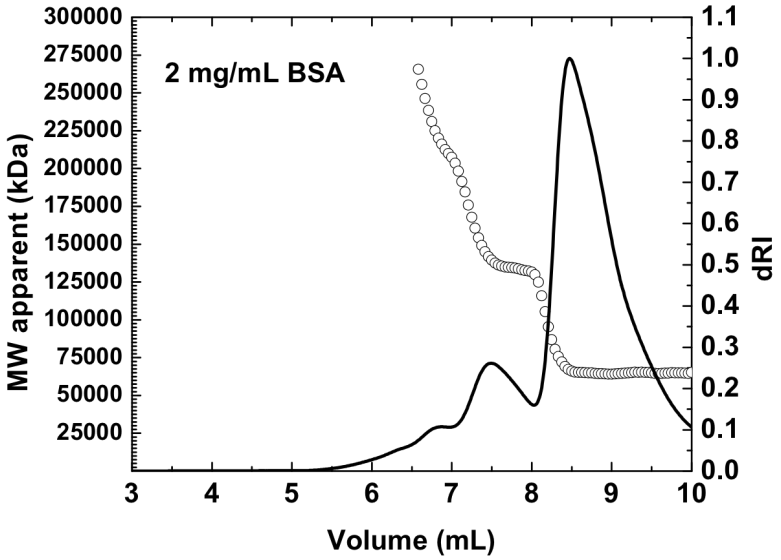

Figure 6.8: SEC-MALLS of 2 mg/mL BSA alone at 1 mL/min. Run at pH 7, 500 mM NaCl, 20 mM phosphate. Used d*n*/d*c* of 0.185 mL/g. Monomer (V_e = 8.5), dimer (V_e = 7.3 mL), and trimer (V_e = 6.8 mL) are clearly resolved.

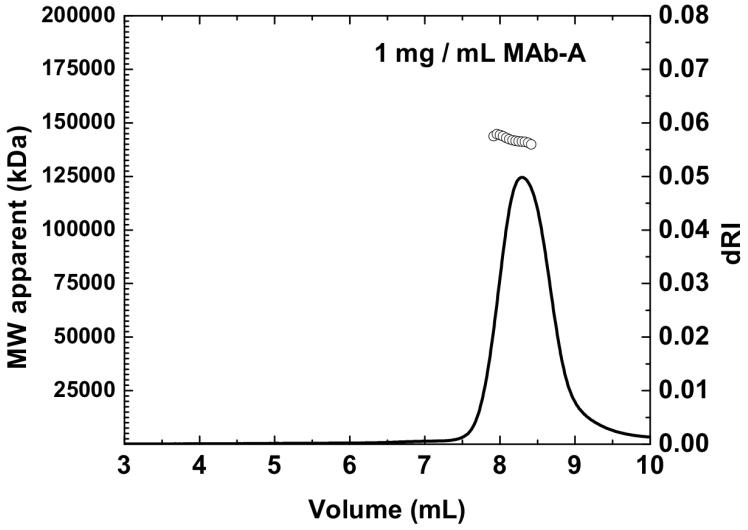

Figure 6.9: SEC-MALS of 1 mg/mL mAb-A alone at 1 mL/min run at pH 7, 500 mM NaCl, 20 mM phosphate. mAb-A has an apparent MW ~ 150 kDa (consistent with monomer MW).

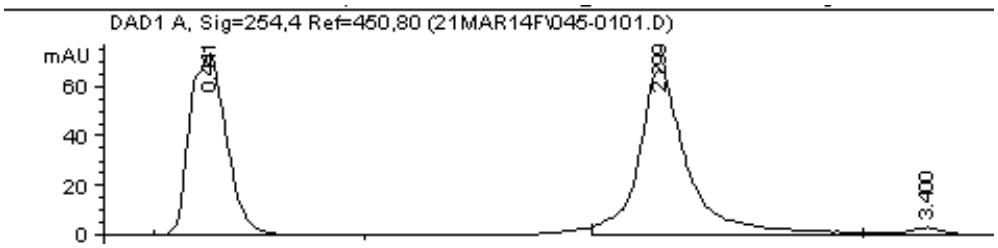

Figure 6.10: Injection of a mixture of BSA and mAb-A onto a HR 5/5 SCX column. The peaks are fully resolved.

Table 6.2: Summary of peak heights and peak widths.

A

Injected 250 uL, mixed in 25 mM NaCl		**Run, 50 mM Phos, pH 8.5, 500 mM NaCl**	
MAb-A	***Using A_{230}***		
Flow Rate (mL/min)	***Elution Volume (mL)***	***Peak Width (mL)***	***Tailing?***
0.50	8.39	0.63	Yes
0.75	8.24	0.65	No
1.00	8.27	0.67	No
1.25	7.99	0.74	No
1.50	7.95	0.71	No

B

Injected 250 uL, mixed in 500 mM NaCl		**Run, 50 mM Phos, pH 8.5, 500 mM NaCl**	
MAb-A	***Using A_{230}***		
Flow Rate (mL/min)	***Elution Volume (mL)***	***Peak Width (mL)***	***Tailing?***
0.50	7.45	0.56	Some
0.50	7.50	0.60	Some
1.50	7.58	0.79	No
1.50	7.58	0.83	No

C

Injected 250 uL in 500 mM NaCl		**Run, 50 mM Phos, pH 8.5, 500 mM NaCl**	
BSA	***Using A_{230}***		
Flow Rate (mL/min)	***Elution Volume (mL)***	***Peak Width (mL)***	***Dimer present?***
0.50	8.07	0.69	15%
0.50	8.10	0.68	14%
1.50	8.16	0.99	18%
1.50	8.14	1.01	18%

Peak heights and peak widths, reported above, for solutions of mAb-A **(A,B)** and BSA **(C)** alone analyzed by SEC (TSK G3000SWXL) show that even optimal choices of flow rate, salt, and running buffer will not provide full baseline separation of BSA from mAb.

CHAPTER 7

SELECTIVE COACERVATION OF MONOCLONAL ANTIBODY WITH ANIONIC POLYELECTROLYTE HYALURONIC ACID

Daniel Seeman, Alexander J. Malanowski, Rachel Wollacott, and Paul L. Dubin ***2015,***
(In Prep)

7.1 Abstract

Anionic polysaccharide hyaluronic acid (HA), was used to isolate a target monoclonal antibody (mAb) from bovine serum albumin (BSA), with a yield as high as 80%, and a selectivity ratio, S, of ca. 490 for coacervates prepared at $pH_c^{BSA} < pH < pH_\varphi^{mAb}$. Values corresponding to the start of complexation, and coacervation (pH_c, pH_φ) are reported over a range of ionic strengths ca. $I < 200$ mM, above which coacervation is no longer observed. Finally, yield of mAb is show to correlate with equilibrium turbidity values, obtained from pH titration.

7.2 Introduction

Selective coacervation of monoclonal antibody with hyaluronic acid (HA) is a promising replacement for affinity-based capture steps currently associated with purification of antibodies. Protein A is nearly universally adopted in such industrial purifications, but its usefulness is limited both by cost and reusability, thus driving the quest for highly-selective, but concentrating, non-chromatographic approaches. Methods based on polyelectrolyte

precipitation of antibodies have been shown to provide some degree of selectivity; however more systematic selection of conditions are needed to provide more control of the yield, stability, and resolubilization of active antibody, especially given the complex kinetics of precipitation. On the other hand, protein-polyelectrolye coacervation is an equilibrium phenomenon, a true liquid−liquid phase separation (LLPS), resulting in enrichment of the target protein and preservation of its native state. In this study we use an anionic polysaccharide, HA, to selectively coacervate a target mAb from a mixture containing a low-pI model impurity.

Protein A affinity chromatography is widely adopted as the initial purification step, in industrial scale purification of monoclonal antibodies (mAbs), but prohibitively high cost related to the stability and lifetime of the column, limits its usefulness. The high affinity and selectivity of Protein A chromatography have made it the preferred method for capturing mAbs from cell culture supernatant (CCS), but the excessive cost of commercial scale columns, which are on the order of several million dollars, forces the use of smaller columns and multiple chromatography cycles. Drawbacks of Protein A include (1) the use of low pH to elute mAb, with possible consequences for its stability, (2) the propensity of protein A ligand to leach from the resin, requiring subsequent polishing steps to avoid immunogenic effects of co-eluted Protein A, and (3) the lack of a rigorous cleaning procedure for the resin, ultimately limiting its reusability. Similar problems have led to a search for non-chromatographic methods for purification of mAbs.

Precipitation of mAbs with anionic polyelectrolytes (PEs) has been shown to provide a limited degree of selectivity for mAb,[154, 155, 156, 157, 158] although such methods are not ideal. The ability to recover active mAb in this way[131, 154, 159] depends on the degree to which the

dense phase is solid- versus liquid-like. Little attention is paid to the exact conditions (pH, *I*) used for phase separation, and the selection of an optimal PE is not systematic.[131] Extensions to other proteins or conditions are impeded by the absence of underlying principles for a process involving often-complex kinetics, as well as ambiguity about the exact nature of the dense phase. Such uncertainties are reduced when the PE-protein interaction leads to a protein-rich well-defined equilibrium dense fluid, i.e., coacervate.

PE/protein complex coacervation is a type of liquid-liquid phase separation (LLPS) induced by electrostatic attraction between proteins and PEs. The arrangement and density of protein charges is highly pH and *I* -dependent, therefore the critical pH[166] (pH_c) depends on (1) the charge anisotropy of a particular protein, and (2) the extent to which protein charges are screened at a particular *I*. This pH_c corresponds to a critical local protein surface charge density, and may occur when the two macromolecules are of like-charge, ultimately controlled by the balance between attraction and repulsion.[79] Phase separation is defined as occurring at pH_φ, and requires the complexes to reach a condition of local charge neutrality.[167] Centrifugation allows for isolation of a dense, protein-rich phase, typically referred to as the coacervate phase. For a binary protein mixture, i.e., a mixture of two separate proteins, the two can be separated on the basis of differing values of pH_φ, resulting in selective enrichment of one the target protein, so long as conditions (pH, *I*) for phase separation are mapped out in advance.[139] Proper selection of solution conditions will maximize selectivity and efficiency for optimal purity and yield of mAb, from clarified CHO cell culture, or Protein-A eluate.

Here, we use hyaluronic acid (HA), an FDA approved cartilage-injectable anionic polysaccharide, to induce selective coacervation with the target mAb (mAb-A). Coacervation

occurs due to electrostatic interactions; therefore, pH and ionic strength needs to be optimized for each additional antibody. Titrations of pH, at different ionic strengths, are used to determine optimal phase separation conditions that lead to maximal mAb selectivity and recovery. Comparison with phase boundaries of HA with BSA, used here as a model protein impurity, allows for determination of optimal separation conditions.

7.3 Experimental Section

Materials. SZE grade sodium hyaluronate, the sodium salt of hyaluronic acid (HA), from Shiseido, Lot No. A07A, $[\eta]$ = 2.6 m^3/kg, was used without further purification. A high isoelectric point monoclonal antibody (mAb-A) was obtained from MassBiologics (Mattapan, MA), with a molecular weight of 147.6 kDa, and a p*I* of 9.6 as determined by isoelectric focusing.

Turbidimetry. Turbidity was measured at room temperature (T = 20-25 °C) using a Brinkmann PC800 colorimeter equipped with a 1 cm path length probe, and a 420 nm filter. For "type I" titrations, dilute NaOH was used to adjust the pH of mAb (1 mg/mL) and HA (0.1 mg/mL) stock solutions to the starting pH, prior to mixing in equal parts. The final concentrations were 0.5 mg/mL MAb-A, and 0.05 mg/mL HA resulting a 10:1 excess of mAb on a weight basis (r = 10). Solution pH was then lowered by controlled addition of dilute 0.01 N HCl solution, which was added dropwise from a microburet under constant stirring. Both pH and transmittance (%T) were recorded after each addition of titrant, allowing sufficient time for the solution to reach equilibrium. Titration is continued until redissolution of coacervate, facilitated by loss of HA charge at acidic conditions, is observed at low pH.

Preparation of mAb/HA coacervates. In order to analyze the composition of the coacervate, samples were prepared using 1 g/L mAb-A, 1 g/L BSA, and 0.2 g/L HA, at I = 25 mM, and pHs 4.5, 5.5, and 7.2. Supernatant was removed from the coacervate; the entire volume of the dense phase was then resuspended in phosphate buffer, containing 1 M NaCl. Each sample was diluted to a final salt concentration of 50 mM NaCl prior to analysis.

Cation-Exchange chromatography. Samples were run on an Agilent 1100 HPLC, with UV detection at 230 nm. Standard curves were constructed by injecting standard solutions using a 10 uL loop, onto a Pharmacia HR 5/5 strong cation-exchange (SCX) column, with a flow rate of 2 mL/min, as previously described (Chapter 6).

7.4 Results & Discussion

7.4.1 Determination of Critical Conditions for MAb-A/HA.

Continuous pH titration experiments of MAb-A/HA and BSA/HA are used to determine conditions where only mAb should undergo coacervation. Turbidimetric pH titrations are used to construct a phase boundary for mAb/HA coacervates, the overlap of which facilitates comparison with previously reported conditions for BSA/HA coacervation (Figure 7.1). All measured values of mAb/HA pH_c are in the region where $\alpha = 1$, in other words, where the polyelectrolyte is fully charged and invariant with respect to pH. However, values of pH_ϕ obtained at $I > 60$ mM, fall in the range of $1 > \alpha > 0.5$, where the charge on HA is reduced as pH is lowered. Furthermore, nearly all pH_c and pH_φ values are at $\alpha < 1$ for BSA, the more acidic of the two proteins. Finally, all critical pH values, pH_c and pH_φ, are at $\alpha > 0.5$, suggesting a unique role of HA charge in controlling electrostatic attractions between proteins.

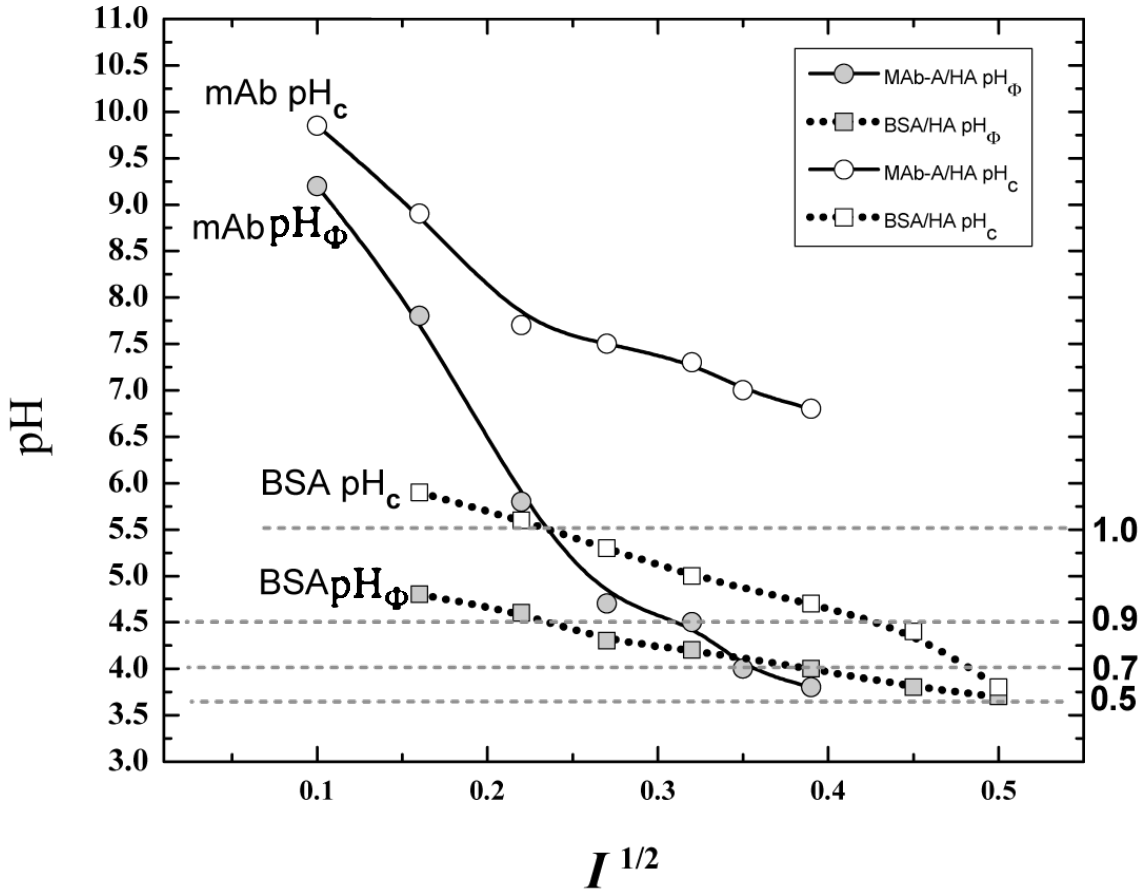

Figure 7.1: Superimposed phase boundaries of mAb-A/HA (solid) and BSA/HA[139] (dashed) at r = 10. Regions *above* pH_c are non-interacting; soluble complex formation occurs in the region of pH < pHc and pH > pH_φ; and coacervation begins at pH < pH_φ. Degree of ionization, α, of HA is shown in right axis.

7.4.2 Rescaling of Boundary Conditions According to Protein Charge

Scaling of critical values, according to the magnitude of protein charge, allows comparison between critical conditions for BSA/HA and mAb/HA coacervates. Such comparisons (Figure 7.2) reveal a nearly linear dependence of pH_φ on $I^{1/2}$; whereas, the more gradual slope of pH_c, near zero at I > 65 mM, is similar to that which is seen for BSA/HA.

Such a dramatic dependence of the pH of phase separation on protein charge, implies that there may be a feature, unique to mAb, that leads to a different role of net protein charge. Considering the large size of mAb-A, and as a result, the large number of ionizable groups on

its surface, it may be possible that the pH of phase separation, pH_{φ}, depends on the local charge of a particular charge domain within the target mAb, rather than on bulk charge neutrality.

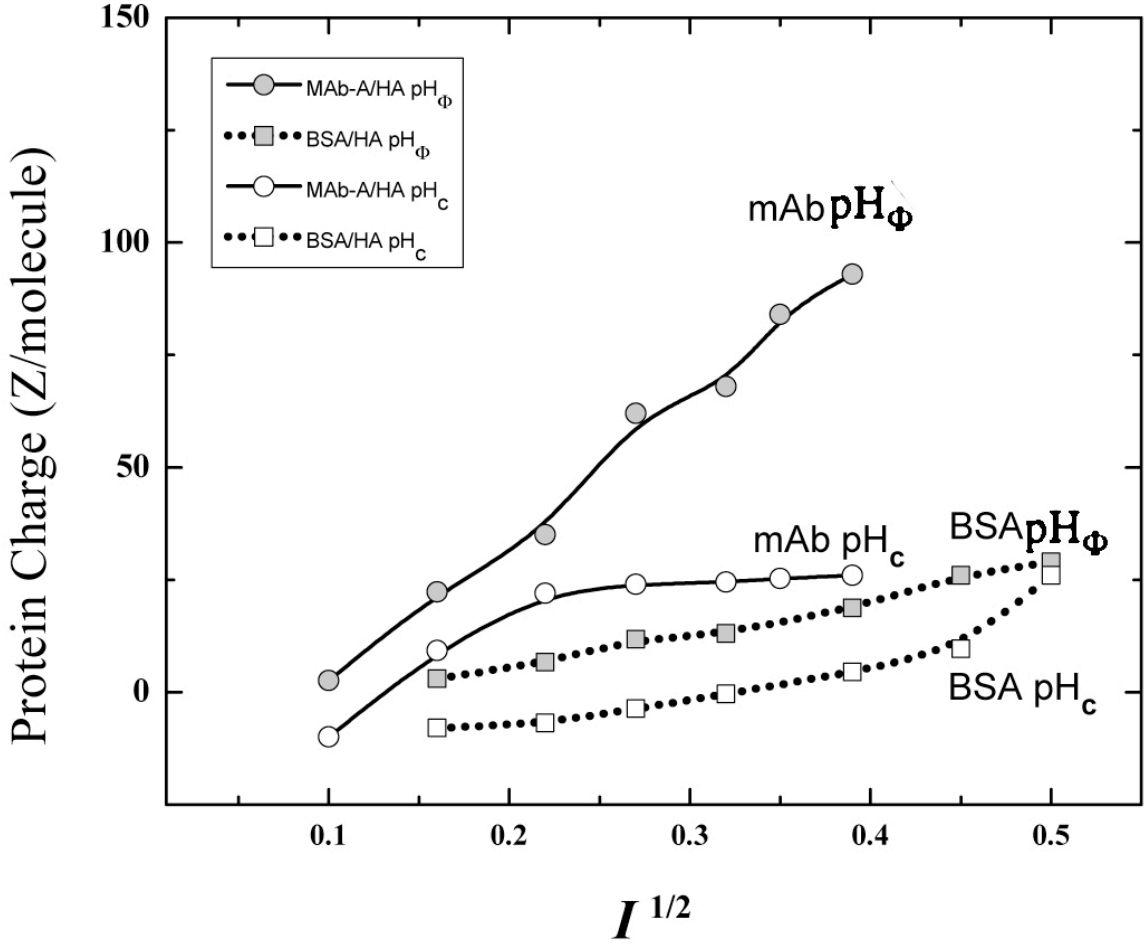

Figure 7.2: mAb-A/HA (solid) and BSA/HA[139] (dashed) at r = 10, normalized to protein charge. $Z < pH_c$ corresponds to non-interacting conditions, where protein charge density is too low to result in complexation.

At pH < 10, both proteins (mAb and BSA) have similar dependences of charge on pH (Figure 7.3), suggesting that despite mAb-A having a remarkably higher pI, and larger number of basic amino acids, the two proteins may have similar charge anisotropy. At highly basic solution conditions, pH > 11, both proteins converge on similar, net negative, total charges.

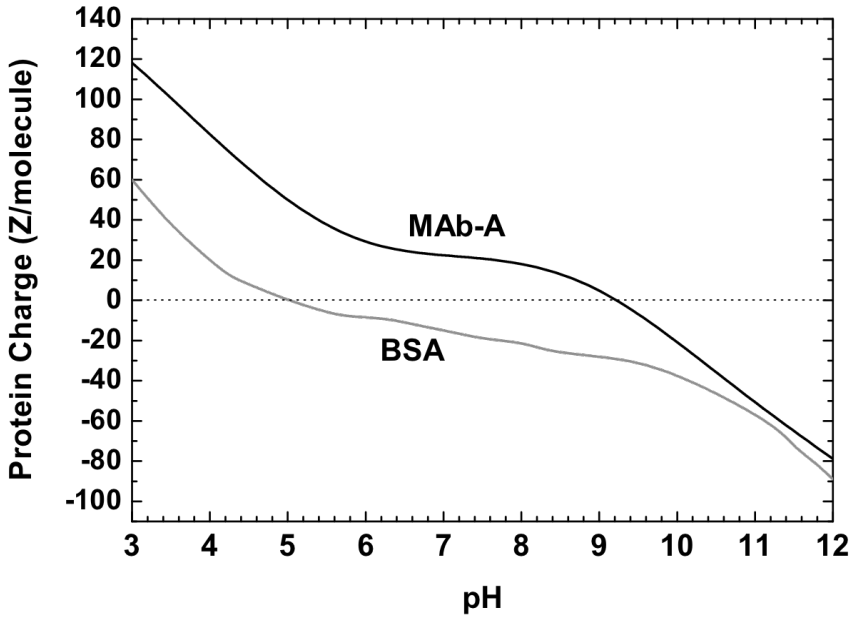

Figure 7.3: Charge curve(s) for BSA (pI 4.9) and mAb-A (pI 9.6).

7.4.3 Turbidity as a Predictor of Coacervate Yield

A previously developed strong-cation exchange (SCX) based method for quantitating the amount of protein contained within mAb/HA coacervates, at given conditions of pH and *I*, was used to determine the yield of coacervates, prepared at conditions along the above phase boundary (Figure 7.4). Samples were prepared at $I = 25$ mM, and pHs 4.5, 5.5, and 7.2. This allows determination of the total mass of protein in the coacervate, relative to starting solutions, at pHs corresponding to different points in a turbidimetric titration. The mass yields of such coacervates are reported in Figure 7.4B, along with turbidity values from a titration, also at $I = 25$ mM.

A

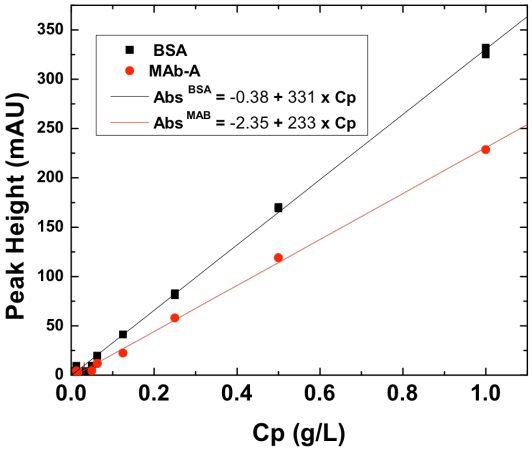

B

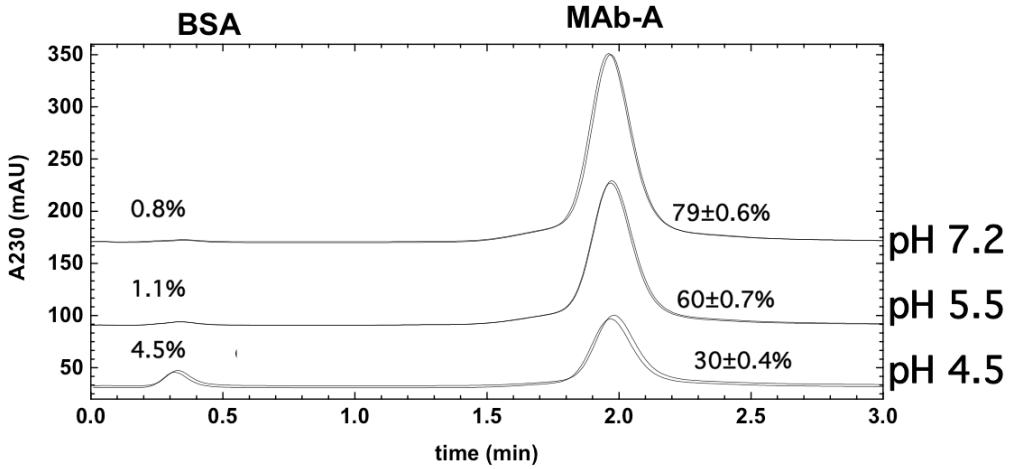

Figure 7.4: Determination of the concentration of BSA & mAb in coacervates prepared at different points in the phase boundary**; (A)** calibration based on 10uL injections uses peak heights at 230 nm; **(B)** %yield of mAb is shown.

7.4.4 Selectivity of HA for mAb

Selectivity arises from the larger enrichment of mAb in the coacervate relative to BSA. Comparison of mAb/HA and BSA/HA phase boundaries allows us to identify conditions for selectively coacervating mAb. The selectivity ratio for mAb/HA and BSA/HA was evaluated at fixed *I*, at various points in the above phase boundary (Figures 7.1 and 7.2). The ratio of $(\text{mAb:BSA})^{coac}/(\text{mAb:BSA})^{sup}$, is used as an indication of the degree of selectivity of HA for mAb, vs. BSA, in a particular region of pH and *I*. This selectivity ratio,

S, is shown to increase by 15X, between pH 4.5 and 5.5, reaching a final value of S = 490 at the turbidimetric maximum (Table 7.1).

Table 7.1: Selectivity ratios at pH 4.5, 5.5, 7.2

Selectivity of MAb-A/BSA/HA coacervation	**mAb:BSA**
pH 4.5	**S = 9**
(coacervate)	**6.5**
(supernatant)	**0.7**
pH 5.5	**S = 135**
(coacervate)	**54**
(supernatant)	**0.4**
pH 7.2	**S = 490**
(coacervate)	**105**
(supernatant)	**0.2**

Selectivity, S, as represented by the ratio of $(mAb:BSA)^{coac}/(mAb:BSA)^{sup}$. Samples prepared at I = 25 mM, and pH 4.5, 5.5, and 7.2. The two limiting cases, S = ∞ and S = 1, would correspond to complete selectivity *and* no selectivity, respectively.

7.5 Conclusions

Phase boundaries for mAb-A (pI ~ 9.6) are reported here, along with those of model "impurity" BSA (pI = 4.9). All pH_c values, determined for mAb, are in the region of pH where the ionization state of HA is invariant; on the other hand, values of pH_{ϕ}^{mAb}, cross into the pH range where $1 > \alpha > 0.5$. All critical pH values, pH_c and pH_{ϕ}, are at $\alpha > 0.5$, suggesting that diminution of HA charge with decreasing pH may be responsible for narrowing of the coacervation region at higher salt. Conditions for selective coacervation of mAb-A are deduced from mAb/HA and BSA/HA phase boundaries. Selectivity of mAb-A/HA binding was evaluated at constant ionic strength, I = 25 mM, at various points in the phase boundary. The selectivity, defined as the enhancement of mAb:BSA ratio in the coacervate, relative to the supernatant, is shown to increase by ca. 15X, from S = 9 to S =

135, between pH 4.5 and 5.5, reaching a final value of S = 490 at the point of maximum turbidity, by which point BSA is nearly undetectable in the coacervate.

7.6 Acknowledgements

This research was supported by the National Center for Advancing Translational Sciences, National Institutes of Health, through Grant UL1TR000161. The content is solely the responsibility of the authors and does not necessarily represent the official views of the NIH. Alexander J. Malanowski acknowledges a Jack Ragle Summer Research Fellowship in Chemistry from the University of Massachusetts-Amherst.

CHAPTER 8

SELF-ASSOCIATION OF MONOCLONAL ANTIBODIES PREDICTING ANOMALOUS INTERACTIONS WITH STATIONARY PHASE

Daniel Seeman, Paul L. Dubin *2015*, (In Prep)

8.1 Abstract

Monoclonal antibodies (mAb), are shown to interact anomalously with chromatography columns when run at low ionic strength (*I*). Absolute molecular weight (MW) determination *vis-à-vis* light scattering detection, suggests that late eluting peaks, are actually 2X *larger* in aggregation number than monomeric antibody (monomer MW ca. 150 kDa).

8.2 Introduction

The ability to design and produce novel biologically-based pharmaceuticals such as monoclonal antibodies (mAbs)[131, 140] has surpassed efforts to formulate or stabilize such proteins; processing mAbs involves moving through a wide range of pHs and buffer compositions prior to reaching a final formulation condition.[131, 141] Stringent FDA guidelines require a well-defined product, meaning that self-association during processing needs to be both measurable and predictable.[168] Better understanding of pre-formulation mAb protein-protein interactions could help optimize yield and minimize downstream costs.

Many such quality control measures rely heavily on chromatography-based analytical methodology,[169, 170] for determining whether the final product is comprised entirely

of intact, monomeric mAb.[170, 171] This is complicated by the fact that methods such as size-exclusion chromatography[172] (SEC) are representative of molecular weight[173], only so long as elution of the protein-of-interest is ideal[174, 175] (e.g., no direct interaction with stationary phase[176, 177]). Elution volumes in non-ideal SEC are no longer dependent solely on hydrodynamic factors,[178] i.e., size; in other words, charged species can elute early or late,[179, 180] depending how strongly they interact with column packing.[172, 181]

To that end, non-ideal interactions between a pharmaceutical mAb (mAb-1) are studied, both in terms of changes in the chromatographic partition coefficient, K_{SEC}, and apparent molecular weight determined from multi-angle laser light scattering (SEC-MALLS) detection.

8.3 Experimental Section

Materials. A high isoelectric point therapeutic monoclonal antibody (mAb-1) was obtained from MassBiologics (Mattapan, MA). The mAb-1 lot used for this study was produced in CHO cells and purified over a protein A column. mAb-1 has a molecular weight of ca. 150 kDa and a pI of approximately 9.6, as determined by isoelectric focusing.

SEC-MALLS of purified mAb. mAb-1 was analyzed directly by size exclusion chromatography (SEC) using a TOSOH TSK-G3000SW_{XL} column, run on a waters HPLC, using a model 410 differential refractometer (dRI), and an on-line multi-angle laser light scattering (MALLS) detector (Wyatt Technology). Samples were run in 20 mM phosphate, pH 7, 500 mM NaCl with < 1% NaN_3. For each run samples were injected manually using a 100 uL loop, and run at a flow rate of 1 mL/min unless otherwise indicated. The refractive

index increments (d*n*/d*c*) for monoclonal antibody (mAb) was taken as 0.185 mL/g. Samples were run in 20 mM phosphate, pH 7, and either 500 mM or 200 mM NaCl.

8.4 Results & Discussion

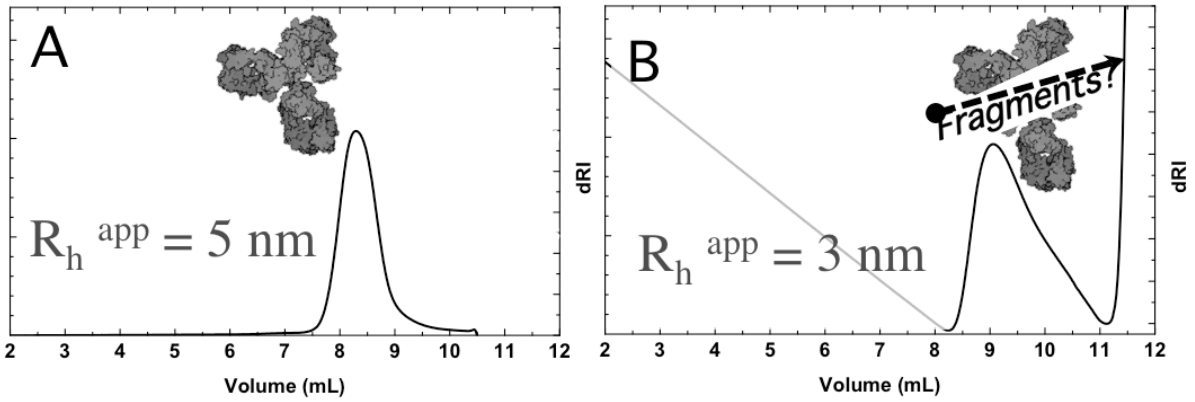

Figure 8.1: SEC of 1 mg/mL mAb-A **(A)** run at pH 7, 500 mM NaCl, 20 mM phosphate and **(B)** pH 7, 200 mM NaCl, 10mM phosphate. Apparent hydrodynamic sizes (R_h) determined from column calibration.

The elution volume, V_e, in lower salt (i.e., 200 mM NaCl) is delayed (note, extended x-axis in panel 8.1B) relative to a sample run in 500 mM NaCl. The difference in elution volume, V_e = 8.2 mL for 500 mM, and V_e = 9.1 for 200 mM, indicates two possibilities; either (1) the presence of a lower molecular weight species, or a (2) stronger interaction with the column. Based strictly on typical standard-based column calibration, this would represent a decrease in hydrodynamic size, from R_h = 5 nm for non-interacting mAb, to 3 nm for the late-eluting peak.

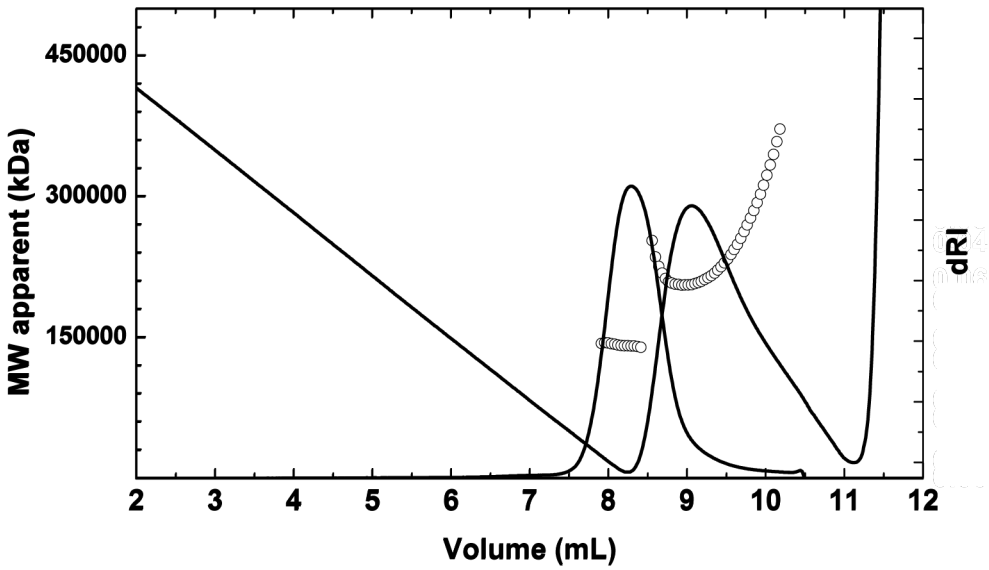

Figure 8.2: SEC-MALLS of mAb-A in 500 mM NaCl and 200mM NaCl. MALLS molecular weights correspond to an aggregation number N^{agg} ca. 2X monomer for the sample run in 200 mM salt. Upturn in dRI trace at V_e = 11 mL is due to solvent peak. At early times, dRI trace has yet to return to baseline after equilibration in low salt buffer.

For this column, the void volume (V_0) is 5.1 mL and the total column volume (V_t), determined by the location of the solvent peak, is 11.2 mL. Thus, it is possible to calculate chromatographic partition coefficients for samples run at 200 mM and 500 mM NaCl, using the following expression:

$$K_{SEC} = (V_e - V_0)/(V_t - V_0) \quad \textbf{(8.1)}$$

For mAb run in 500 mM NaCl, for which it can be assumed that electrostatic interactions with the column are sufficiently screened as to be non-interacting, K_{SEC} = 0.5; versus K_{SEC} = 0.66, for the sample run at strongly interacting conditions (i.e., 200 mM).

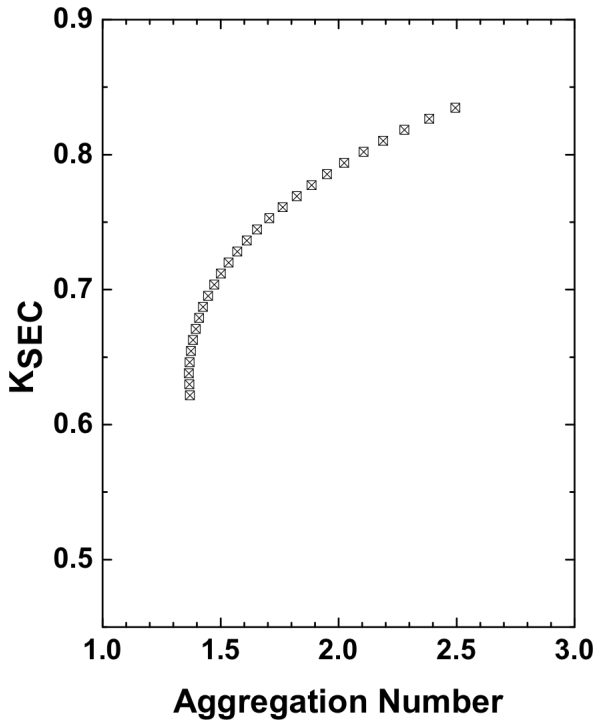

Figure 8.3: Chromatographic partition coefficients (K_{SEC}) for sample run at 200 mM as a function of apparent aggregation number (from MALLS)

It is worth noting that the apparent molecular weight, determined by MALLS, is *higher than* that of monomer. The average molecular weight, calculated using the sum of all multi-angle scattering data collected between V_e = 8 and 10 mL, is ca. 300 kDa, compared to the 150 kDa monomer of MAb-1. This result strongly implies that not only is this mAb interacting more strongly with the column; but that such interactions have actually promoted, or possibly are the product of, dimerization. Furthermore, the shoulder, visible at V_e > 9.5 mL, must correspond to a high aggregation number species, possibly aggregates of mAb, or maybe clusters similar to those responsible for LLPS of mAb at low temperature (chapter 5).

8.4 Conclusions

Hydrodynamic based SEC calibration methods, suggest apparent molecular weight for mAb-1, injected at 200 mM NaCl, that is smaller than that of mAb monomer, where such delayed elution volumes are typically attributed to the existence of antibody fragments, of smaller size than monomer. However, MALLS-based, absolute molecular weight determination, strongly suggests that such late eluting peaks, are actually *larger than monomer*, ranging in size from well-defined dimeric mAb, to large aggregates. This suggests that anomalous hydrodynamic effects, rather than fragmentation or chemical degradation, is responsible this type of delayed elution.

8.5 Acknowledgements

This research was supported by the National Center for Advancing Translational Sciences, National Institutes of Health, through Grant UL1TR000161. The content is solely the responsibility of the authors and does not necessarily represent the official views of the NIH.

CHAPTER 9

CONCLUSIONS & FUTURE OUTLOOK

9.1 Summary and Conclusions

Turbidimetric titrations of aggregation-prone proteins, can provide accurate measurements of the pH-dependence of the turbidimetric aggregation rate ($d\tau/dt$). This is used, in the case of model protein BLG, to identify two, predominantly electrostatic, self-association steps, and a condition where the macroscopic aggregation rate is equal to zero. Such a "quench" condition can be exploited to conduct static light scattering (SLS) of aggregates, which showed the formation of increasingly dense fractal structures over time.

Scattering was also used to elucidate the basic structural unit in a coacervate prepared from two, oppositely charged, globular proteins. Small-angle neutron scattering (SANS) data of BLG–LF heteroprotein coacervates (HPCs) is poorly explained by a single, rigidly fixed BLG_2–LF unit, therefore, there must be ongoing rearrangement within a primary unit; although it seems that the two component proteins retain their globular structures. Rheology shows that the elasticity of this network of primary units is only weakly dependent on mixing pH (within the range of pH 5.8 – 6.1), where changes in frequency dependence, must reflect changes in the dynamics of component proteins.

A high level of nonfreezing water (NFW) was found in several coacervating systems, with the most significant effect for LF-BLG heteroprotein coacervates. HPCs have the highest percentage of NFW *and* a larger ratio of NFW:total macromolecule, which can be attributed to the existence of a well-defined structural unit, described by $LF(BLG_2)_2$ which enhances protein-water contacts at the expense of protein-contacts.

Phase separation of monoclonal antibody (mAb) occurs readily at temperatures below the upper critical solution temperature. It is possible that this could assist in designing mAbs, optimized for purification efficiency, as well as optimizing stability with respect to formulation. Solution conditions (pH and *I*) could be established where LLPS allows for separation of crude mixtures into a mAb-enhanced, and HCP-depleted, dense phase.

Injectable anionic polysaccharide hyaluronic acid (HA) was used to induce selective coacervation of mAb, without coacervation of impurity proteins. Yields are assessed by analysis of supernatant, and also by direct analysis of the coacervate phase. Even at an un-optimized ratio of mAb:HA, over 80% of mAb is shown to go into the coacervate phase. The concentration of mAb in dense phase was shown to be over 170 mg/mL, similar in magnitude to that seen for typical protein-PE coacervates (usually ca. 200 mg/mL). The yield of HA in the coacervate was estimated to be at least 75%, with a concomitant 2X increase in apparent molecular weight, relative to supernatant. Selective enrichment of higher molecular weight HA chains may make it easier to remove residual HA by ultrafiltration methods. Additionally, mAb/HA coacervates are easily redissolved, by adjusting either *I* or pH, allowing recovery of intact monomeric mAb.

Phase boundaries for a high pI mAb were generated and compared with those of BSA. Selectivity ratios for mAb/HA BSA/HA coacervates were shown to increase with increasing pH, before reaching a final value of S = 490 at the point of maximum turbidity determined from pH titration. We demonstrate the ability to rapidly determine conditions useful for the selective coacervation of mAb-A, or for any other mAb, with HA.

Monoclonal antibodies can interact anomalously with the stationary phase of any chromatography column cable of holding charge. Classical SEC calibration methods imply

that the molecular weight of such strongly interacting species should be smaller than that of monomer, and are frequently attributed to the existence of chemically degraded antibody fragments. However, SEC-MALLS of mAb run in low salt strongly suggest that such late eluting peaks must have an aggregation number of at least 2X, representing either mAb dimer, or aggregate.

9.2 Overview

As demonstrated in this work; protein-protein interactions in solutions *of a single protein* can either results in open-ended kinetic aggregation (as in the case of model protein BLG); or if conditions of pH and *I* are optimal leads to a special form of LLPS (as with mAb); qualitatively similar to complex coacervation, but comprised of a single self-interacting macroion. Heteroprotein-interactions reflect the need for a specific geometric ordering (facilitated by complementarity of protein surface charge); resulting in a highly limited set of conditions at which two, oppositely charged, proteins can be mixed to form a heteroprotein coacervate; demonstrated specifically for coacervates of LF and BLG. The conditions under which a protein and polyelectrolyte can be combined to form a coacervate are far more expansive; the versatility of this method having been exploited to selectively coacervate a highly anisotropic protein, monoclonal antibody. Lastly, non-ideal chromatographic behavior, reflected in delayed elution volumes for highly charged proteins, likely involve attractive electrostatic interactions, facilitated by protein charge patches; similar to the interactions that result in complexation on "wrong side" of pI in classical protein containing coacervates.

9.3 Outlook

Understanding the relationship between protein charge anisotropy and macromolecular phenomenon such as complexation, coacervation, and phase separation, will allow for greater control over the conditions under which such processes can occur. This work will aid in applying robust electrostatic modeling of proteins to a number of classical coacervating systems. Such methods can also be coupled with electrostatically-based Monte Carlo simulations (Figure 9.1), to facilitate understanding the relationship between charged proteins, and their polymeric binding partners.

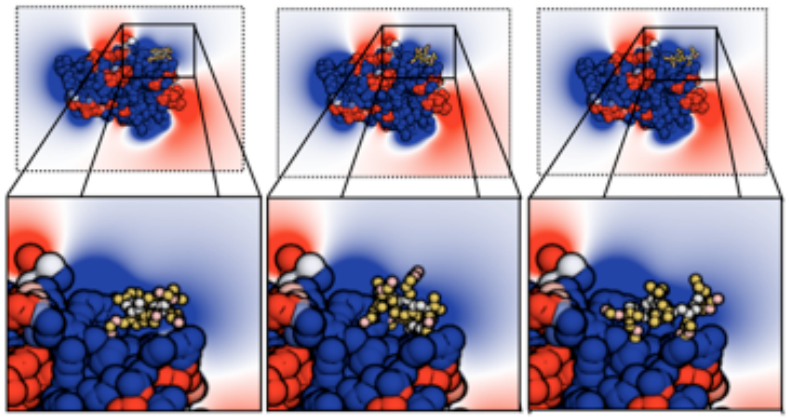

Figure 9.1: Monte Carlo simulations: Antithrombin binding a model Hp pentasaccharide. Expanded view shows binding at the positive (blue) AT domain with retention of conformational flexibility.

Much of the work done to improve general understanding of protein phase behavior can be directly utilized in the production of biologics, specifically monoclonal antibodies (mAbs). This will help, both in terms of (1) understanding native aggregation of mAbs, and the various ways this can impair downstream processing and formulations, and (2) potentially allow for the use of protein charge anisotropy as a design criteria in the production of stable mAbs.

Although, the more immediate impact will be in terms of efforts to validate non-chromatographic methods for purification of mAbs. Methods based on liquid-liquid phase separation have the potential to greatly reduce dependency on the vastly expensive affinity chromatographies, currently used in the industrial scale production of protein drugs. Replacing the expensive Protein A chromatography columns used in the production of mAbs, with one of the non-chromatographic methods evaluated in this work may be able to significantly reduce the cost of the downstream processing. The success of LLPS-based purification methods (including coacervation) will depend on finding conditions that (1) result in phase, via selective enrichment of the lower phase and (2) minimize mAb/HCP interactions, in order to avoid incidental concentration of contaminants.

BIBLIOGRAPHY

1. Asthagiri, D.; Paliwal, A.; Abras, D.; Lenhoff, A. M.; Paulaitis, M. E. A consistent experimental and modeling approach to light-scattering studies of protein-protein interactions in solution. *Biophys J* 2005, *88* (5), 3300-3309.

2. Liu, Y.; Fratini, E.; Baglioni, P.; Chen, W. R.; Chen, S. H. Effective long-range attraction between protein molecules in solutions studied by small angle neutron scattering - art. no. 118402. *Phys Rev Lett* 2005, *95* (11).

3. Sharp, K. A.; Honig, B. Calculating Total Electrostatic Energies with the Nonlinear Poisson-Boltzmann Equation. *J Phys Chem-Us* 1990, *94* (19), 7684-7692.

4. Tanford, C.; Kirkwood, J. G. Theory of Protein Titration Curves .1. General Equations for Impenettrable Spheres. *J Am Chem Soc* 1957, *79* (20), 5333-5339.

5. Arosio, P.; Rima, S.; Lattuada, M.; Morbidelli, M. Population Balance Modeling of Antibodies Aggregation Kinetics. *J Phys Chem B* 2012, *116* (24), 7066-7075.

6. Carpenter, J. F.; Randolph, T. W.; Jiskoot, W.; Crommelin, D. J. A.; Middaugh, C. R.; Winter, G.; Fan, Y. X.; Kirshner, S.; Verthelyi, D.; Kozlowski, S.; Clouse, K. A.; Swann, P. G.; Rosenberg, A.; Cherney, B. Overlooking Subvisible Particles in Therapeutic Protein Products: Gaps That May Compromise Product Quality. *J Pharm Sci-Us* 2009, *98* (4), 1201-1205.

7. Roberts, C. J. Kinetics of irreversible protein aggregation: Analysis of extended Lumry-Eyring models and implications for predicting protein shelf life. *J Phys Chem B* 2003, *107* (5), 1194-1207.

8. Frieden, C. Protein aggregation processes: In search of the mechanism. *Protein Sci* 2007, *16* (11), 2334-2344.

9. Fink, A. L. Protein aggregation: folding aggregates, inclusion bodies and amyloid. *Fold Des* 1998, *3* (1), R9-R23.

10. Sanchez-Ruiz, J. M. Protein kinetic stability. *Biophys Chem* 2010, *148* (1-3), 1-15.

11. Nicolai, T.; Britten, M.; Schmitt, C. beta-Lactoglobulin and WPI aggregates: Formation, structure and applications. *Food Hydrocolloid* 2011, *25* (8), 1945-1962.

12. Park, J. M.; Muhoberac, B. B.; Dubin, P. L.; Xia, J. L. Effects of Protein Charge Heterogeneity in Protein-Polyelectrolyte Complexation. *Macromolecules* 1992, *25* (1), 290-295.

13. Seyrek, E.; Dubin, P. L.; Tribet, C.; Gamble, E. A. Ionic strength dependence of protein-polyelectrolyte interactions. *Biomacromolecules* 2003, *4* (2), 273-282.

14. Meakin, P. A historical introduction to computer models for fractal aggregates. *J Sol-Gel Sci Techn* 1999, *15* (2), 97-117.

15. Ferrone, F. Analysis of protein aggregation kinetics. *Method Enzymol* 1999, *309*, 256-274.

16. Lin, M. Y.; Lindsay, H. M.; Weitz, D. A.; Ball, R. C.; Klein, R.; Meakin, P. Universal Reaction-Limited Colloid Aggregation. *Phys Rev A* 1990, *41* (4), 2005-2020.

17. Kurganov, B. I.; Rafikova, E. R.; Dobrov, E. N. Kinetics of thermal aggregation of tobacco mosaic virus coat protein. *Biochemistry-Moscow+* 2002, *67* (5), 525-533.

18. Wang, K. Y.; Kurganov, B. I. Kinetics of heat- and acidification-induced aggregation of firefly luciferase. *Biophys Chem* 2003, *106* (2), 97-109.

19. Golub, N. V.; Markossian, K. A.; Sholukh, M. V.; Muranov, K. O.; Kurganov, B. I. Study of kinetics of thermal aggregation of mitochondrial aspartate aminotransferase by dynamic light scattering: protective effect of alpha-crystallin. *Eur Biophys J Biophy* 2009, *38* (5), 547-556.

20. Kayitmazer, A. B.; Seeman, D.; Minsky, B. B.; Dubin, P. L.; Xu, Y. Protein-polyelectrolyte interactions. *Soft Matter* 2013, *9* (9), 2553-2583.

21. Philo, J. S.; Arakawa, T. Mechanisms of Protein Aggregation. *Curr Pharm Biotechno* 2009, *10* (4), 348-351.

22. Brady, G. P.; Sharp, K. A. Entropy in protein folding and in protein-protein interactions. *Curr Opin Struc Biol* 1997, *7* (2), 215-221.

23. Grymonpre, K. R.; Staggemeier, B. A.; Dubin, P. L.; Mattison, K. W. Identification by integrated computer modeling and light scattering studies of an electrostatic serum albumin-hyaluronic acid binding site. *Biomacromolecules* 2001, *2* (2), 422-429.

24. Dufrechou, M.; Poncet-Legrand, C.; Sauvage, F. X.; Vernhet, A. Stability of White Wine Proteins: Combined Effect of pH, Ionic Strength, and Temperature on Their Aggregation. *J Agr Food Chem* 2012, *60* (5), 1308-1319.

25. Gummadi, S. N. What is the role of thermodynamics on protein stability? *Biotechnol Bioproc E* 2003, *8* (1), 9-18.

26. Schreiber, G.; Fersht, A. R. Rapid, electrostatically assisted association of proteins. *Nat Struct Biol* 1996, *3* (5), 427-431.

27. Selzer, T.; Schreiber, G. Predicting the rate enhancement of protein complex formation from the electrostatic energy of interaction. *J Mol Biol* 1999, *287* (2), 409-419.

28. Mathews, C. K.; Holde, K. E. v.; Ahern, K. G. *Biochemistry, 3rd ed.* 2000.

29. Cruz, L.; Urbanc, B.; Buldyrev, S. V.; Christie, R.; GomezIsla, T.; Havlin, S.; McNamara, M.; Stanley, H. E.; Hyman, B. T. Aggregation and disaggregation of senile plaques in Alzheimer disease. *P Natl Acad Sci USA* 1997, *94* (14), 7612-7616.

30. Urbanc, B.; Cruz, L.; Buldyrev, S. V.; Havlin, S.; Hyman, B. T.; Stanley, H. E. Dynamic feedback in an aggregation-disaggregation model. *Phys Rev E* 1999, *60* (2), 2120-2126.

31. Majhi, P. R.; Ganta, R. R.; Vanam, R. P.; Seyrek, E.; Giger, K.; Dubin, P. L. Electrostatically driven protein aggregation: beta-lactoglobulin at low ionic strength. *Langmuir* 2006, *22* (22), 9150-9159.

32. Xu, Y.; Seeman, D.; Yan, Y. F.; Sun, L. H.; Post, J.; Dubin, P. L. Effect of Heparin on Protein Aggregation: Inhibition versus Promotion. *Biomacromolecules* 2012, *13* (5), 1642-1651.

33. Xu, Y.; Yan, Y. F.; Seeman, D.; Sun, L. H.; Dubin, P. L. Multimerization and Aggregation of Native-State Insulin: Effect of Zinc. *Langmuir* 2012, *28* (1), 579-586.

34. Schmitt, C.; Bovay, C.; Rouvet, M.; Shojaei-Rami, S.; Kolodziejczyk, E. Whey protein soluble aggregates from heating with NaCl: Physicochemical, interfacial, and foaming properties. *Langmuir* 2007, *23* (8), 4155-4166.

35. Schmitt, C.; Moitzi, C.; Bovay, C.; Rouvet, M.; Bovetto, L.; Donato, L.; Leser, M. E.; Schurtenberger, P.; Stradner, A. Internal structure and colloidal behaviour of covalent whey protein microgels obtained by heat treatment. *Soft Matter* 2010, *6* (19), 4876-4884.

36. Davis, P. J.; Williams, S. C. Protein modification by thermal processing. *Allergy* 1998, *53*, 102-105.

37. Ehn, B. M.; Ekstrand, B.; Bengtsson, U.; Ahlstedt, S. Modification of IgE binding during heat processing of the cow's milk allergen beta-lactoglobulin. *J Agr Food Chem* 2004, *52* (5), 1398-1403.

38. Hamada, D.; Dobson, C. M. A kinetic study of beta-lactoglobulin amyloid fibril formation promoted by urea. *Protein Sci* 2002, *11* (10), 2417-2426.

39. Krebs, M. R. H.; Devlin, G. L.; Donald, A. M. Amyloid Fibril-Like Structure Underlies the Aggregate Structure across the pH Range for beta-Lactoglobulin. *Biophys J* 2009, *96* (12), 5013-5019.

40. Lansbury, P. T.; Lashuel, H. A. A century-old debate on protein aggregation and neurodegeneration enters the clinic. *Nature* 2006, *443* (7113), 774-779.

41. Le Bon, C.; Nicolai, T.; Durand, D. Growth and structure of aggregates of heat-denatured beta-Lactoglobulin. *Int J Food Sci Tech* 1999, *34* (5-6), 451-465.

42. Verheul, M.; Roefs, S. P. F. M.; de Kruif, C. G. Kinetics of heat-induced aggregation of beta-lactoglobulin. *J Agr Food Chem* 1998, *46* (3), 896-903.

43. Burgos, I.; Dassie, S. A.; Villarreal, M. A.; Fidelio, G. D. Thermodynamic and structural analysis of homodimeric proteins: Model of beta-lactoglobulin. *Bba-Proteins Proteom* 2012, *1824* (2), 383-391.

44. Loupiac, C.; Bonetti, M.; Pin, S.; Calmettes, P. beta-lactoglobulin under high pressure studied by small-angle neutron scattering. *Bba-Proteins Proteom* 2006, *1764* (2), 211-216.

45. Mckenzie, H. A.; Sawyer, W. H. Effect of Ph on Beta-Lactoglobulins. *Nature* 1967, *214* (5093), 1101-&.

46. Renard, D.; Lefebvre, J.; Griffin, M. C. A.; Griffin, W. G. Effects of pH and salt environment on the association of beta-lactoglobulin revealed by intrinsic fluorescence studies. *Int J Biol Macromol* 1998, *22* (1), 41-49.

47. Baldini, G.; Beretta, S.; Chirico, G.; Franz, H.; Maccioni, E.; Mariani, P.; Spinozzi, F. Salt-induced association of beta-lactoglobulin by light and X-ray scattering. *Macromolecules* 1999, *32* (19), 6128-6138.

48. Gottschalk, M.; Nilsson, H.; Roos, H.; Halle, B. Protein self-association in solution: The bovine beta-lactoglobulin dimer and octamer. *Protein Sci* 2003, *12* (11), 2404-2411.

49. Verheul, M.; Pedersen, J. S.; Roefs, S. P. F. M.; de Kruif, C. G. Association behavior of native beta-lactoglobulin. *Biopolymers* 1999, *49* (1), 11-20.

50. Timasheff, S. N.; Townend, R. Structure of Beta-Lactoglobulin Tetramer. *Nature* 1964, *203* (494), 517-&.

51. Townend, R.; Timasheff, S. N. Molecular Interactions in Beta-Lactoglobulin .3. Light Scattering Investigation of the Stoichiometry of the Association between Ph 3.7 and 5.2. *J Am Chem Soc* 1960, *82* (12), 3168-3174.

52. Townend, R.; Winterbottom, R. J.; Timasheff, S. N. Molecular Interactions in Beta-Lactoglobulin .2. Ultracentrifugal and Electrophoretic Studies of the Association of Beta-Lactoglobulin Below Its Isoelectric Point. *J Am Chem Soc* 1960, *82* (12), 3161-3168.

53. Kumosins, T. F.; Timashef, S. Molecular Interactions in Beta-Lactoglobulin .X. Stoichiometry of Beta-Lactoglobulin Mixed Tetramerization. *J Am Chem Soc* 1966, *88* (23), 5635-&.

54. Piazza, R.; Iacopini, S. Transient clustering in a protein solution. *Eur Phys J E* 2002, *7* (1), 45-48.

55. Timasheff, S. N.; Townend, R. The Association Behavior of Beta-Lactoglobulins-a and Beta-Lactoglobulins-B. *J Am Chem Soc* 1958, *80* (16), 4433-4434.

56. Lin, M. Y.; Lindsay, H. M.; Weitz, D. A.; Ball, R. C.; Klein, R.; Meakin, P. Universality of Fractal Aggregates as Probed by Light-Scattering. *P Roy Soc Lond a Mat* 1989, *423* (1864), 71-87.

57. Xu, Y.; Mazzawi, M.; Chen, K. M.; Sun, L. H.; Dubin, P. L. Protein Purification by Polyelectrolyte Coacervation: Influence of Protein Charge Anisotropy on Selectivity. *Biomacromolecules* 2011, *12* (5), 1512-1522.

58. Navea, S.; Tauler, R.; de Juan, A. Monitoring and modeling of protein processes using mass spectrometry, circular dichroism, and multivariate curve resolution methods. *Anal Chem* 2006, *78* (14), 4768-4778.

59. Giger, K.; Vanam, R. P.; Seyrek, E.; Dubin, P. L. Suppression of insulin aggregation by heparin. *Biomacromolecules* 2008, *9* (9), 2338-2344.

60. Kim, A. Y.; Berg, J. C. Fractal aggregation: Scaling of fractal dimension with stability ratio. *Langmuir* 2000, *16* (5), 2101-2104.

61. Nozaki, Y.; Bunville, L. G.; Tanford, C. Hydrogen Ion Titration Curves of Beta-Lactoglobulin. *J Am Chem Soc* 1959, *81* (21), 5523-5529.

62. Jho, Y. S.; Safran, S. A.; In, M.; Pincus, P. A. Effect of Charge Inhomogeneity and Mobility on Colloid Aggregation. *Langmuir* 2012, *28* (22), 8329-8336.

63. Perkin, S.; Kampf, N.; Klein, J. Long-range attraction between charge-mosaic surfaces across water. *Phys Rev Lett* 2006, *96* (3).

64. Cooper, C. L.; Goulding, A.; Kayitmazer, A. B.; Ulrich, S.; Stoll, S.; Turksen, S.; Yusa, S.; Kumar, A.; Dubin, P. L. Effects of polyelectrolyte chain stiffness, charge mobility, and charge sequences on binding to proteins and micelles. *Biomacromolecules* 2006, *7* (4), 1025-1035.

65. Priftis, D.; Laugel, N.; Tirrell, M. Thermodynamic Characterization of Polypeptide Complex Coacervation. *Langmuir* 2012, *28* (45), 15947-15957.

66. de Kruif, C. G.; Weinbreck, F.; de Vries, R. Complex coacervation of proteins and anionic polysaccharides. *Curr Opin Colloid In* 2004, *9* (5), 340-349.

67. Gummel, J.; Boue, F.; Clemens, D.; Cousin, F. Finite size and inner structure controlled by electrostatic screening in globular complexes of proteins and polyelectrolytes. *Soft Matter* 2008, *4* (8), 1653-1664.

68. van de Weert, M.; Andersen, M. B.; Frokjaer, S. Complex coacervation of lysozyme and heparin: Complex characterization and protein stability. *Pharm Res* 2004, *21* (12), 2354-2359.

69. Kizilay, E.; Dinsmore, A. D.; Hoagland, D. A.; Sun, L. H.; Dubin, P. L. Evolution of hierarchical structures in polyelectrolyte-micelle coacervates. *Soft Matter* 2013, *9* (30), 7320-7332.

70. Kizilay, E.; Kayitmazer, A. B.; Dubin, P. L. Complexation and coacervation of polyelectrolytes with oppositely charged colloids. *Adv Colloid Interfac* 2011, *167* (1-2), 24-37.

71. Leisner, D.; Imae, T. Interpolyelectrolyte complex and coacervate formation of poly(glutamic acid) with a dendrimer studied by light scattering and SAXS. *J Phys Chem B* 2003, *107* (32), 8078-8087.

72. Anema, S. G.; de Kruif, C. G. Complex coacervates of lactotransferrin and beta-lactoglobulin. *J Colloid Interf Sci* 2014, *430*, 214-220.

73. Nigen, M.; Croguennec, T.; Renard, D.; Bouhallab, S. Temperature affects the supramolecular structures resulting from alpha-lactalbumin-lysozyme interaction. *Biochemistry-Us* 2007, *46* (5), 1248-1255.

74. Tiwari, A.; Bindal, S.; Bohidar, H. B. Kinetics of Protein-Protein Complex Coacervation and Biphasic Release of Salbutamol Sulfate from Coacervate Matrix. *Biomacromolecules* 2009, *10* (1), 184-189.

75. Yan, Y.; Kizilay, E.; Seeman, D.; Flanagan, S.; Dubin, P. L.; Bovetto, L.; Donato, L.; Schmitt, C. Heteroprotein Complex Coacervation: Bovine beta-Lactoglobulin and Lactoferrin. *Langmuir* 2013, *29* (50), 15614-15623.

76. Bouhallab, S.; Croguennec, T. Spontaneous Assembly and Induced Aggregation of Food Proteins. *Adv Polym Sci* 2014, *256*, 67-101.

77. Nigen, M.; Croguennec, T.; Madec, M. N.; Bouhallab, S. Apo alpha-lactalbumin and lysozyme are colocalized in their subsequently formed spherical supramolecular assembly. *Febs J* 2007, *274* (23), 6085-6093.

78. Nigen, M.; Le Tilly, V.; Croguennec, T.; Drouin-Kucma, D.; Bouhallab, S. Molecular interaction between apo or holo alpha-lactalbumin and lysozyme: Formation of heterodimers as assessed by fluorescence measurements. *Bba-Proteins Proteom* 2009, *1794* (4), 709-715.

79. Cooper, C. L.; Dubin, P. L.; Kayitmazer, A. B.; Turksen, S. Polyelectrolyte-protein complexes. *Curr Opin Colloid In* 2005, *10* (1-2), 52-78.

80. Hiroshi, M. A.; Kikuchi, R.; Ogawa, K.; Kokufuta, E. Light scattering study of complex formation between protein and polyelectrolyte at various ionic strengths. *Colloid Surface B* 2007, *56* (1-2), 142-148.

81. Girard, M.; Turgeon, S. L.; Gauthier, S. F. Quantification of the interactions between beta-lactoglobulin and pectin through capillary electrophoresis analysis. *J Agr Food Chem* 2003, *51* (20), 6043-6049.

82. Hattori, T.; Kimura, K.; Seyrek, E.; Dubin, P. L. Binding of bovine serum albumin to heparin determined by turbidimetric titration and frontal analysis continuous capillary electrophoresis. *Anal Biochem* 2001, *295* (2), 158-167.

83. Gummel, J.; Cousin, F.; Verbavatz, J. M.; Boue, F. Wide scale range structure in polyelectrolyte-protein dense complexes: Where Sans meets freeze-fracture microscopy. *J Phys Chem B* 2007, *111* (29), 8540-8546.

84. Salvatore, D.; Croguennec, T.; Bouhallab, S.; Forge, V.; Nicolai, T. Kinetics and Structure during Self-Assembly of Oppositely Charged Proteins in Aqueous Solution. *Biomacromolecules* 2011, *12* (5), 1920-1926.

85. Priftis, D.; Megley, K.; Laugel, N.; Tirrell, M. Complex coacervation of poly(ethylene-imine)/polypeptide aqueous solutions: Thermodynamic and rheological characterization. *J Colloid Interf Sci* 2013, *398*, 39-50.

86. Anema, S. G.; de Kruif, C. G. Coacervates of lysozyme and beta-casein. *J Colloid Interf Sci* 2013, *398*, 255-261.

87. Desfougeres, Y.; Croguennec, T.; Lechevalier, V.; Bouhallab, S.; Nau, F. Charge and Size Drive Spontaneous Self-Assembly of Oppositely Charged Globular Proteins into Microspheres. *J Phys Chem B* 2010, *114* (12), 4138-4144.

88. Zhang, D. M.; Vangala, K.; Jiang, D. P.; Zou, S. G.; Pechan, T. Drop Coating Deposition Raman Spectroscopy of Fluorescein Isothiocyanate Labeled Protein. *Appl Spectrosc* 2010, *64* (10), 1078-1085.

89. Svergun, D. I.; Richard, S.; Koch, M. H. J.; Sayers, Z.; Kuprin, S.; Zaccai, G. Protein hydration in solution: Experimental observation by x-ray and neutron scattering. *P Natl Acad Sci USA* 1998, *95* (5), 2267-2272.

90. Harada, R.; Sugita, Y.; Feig, M. Protein Crowding Affects Hydration Structure and Dynamics. *J Am Chem Soc* 2012, *134* (10), 4842-4849.

91. Pizzitutti, F.; Marchi, M.; Sterpone, F.; Rossky, P. J. How protein surfaces induce anomalous dynamics of hydration water. *J Phys Chem B* 2007, *111* (26), 7584-7590.

92. Sterpone, F.; Stirnemann, G.; Laage, D. Magnitude and Molecular Origin of Water Slowdown Next to a Protein. *J Am Chem Soc* 2012, *134* (9), 4116-4119.

93. Tarek, M.; Tobias, D. J. Single-particle and collective dynamics of protein hydration water: A molecular dynamics study. *Phys Rev Lett* 2002, *89* (27).

94. Otting, G.; Wuthrich, K. Studies of Protein Hydration in Aqueous-Solution by Direct Nmr Observation of Individual Protein-Bound Water-Molecules. *J Am Chem Soc* 1989, *111* (5), 1871-1875.

95. Wang, J. H. Theory of the Self-Diffusion of Water in Protein Solutions - a New Method for Studying the Hydration and Shape of Protein Molecules. *J Am Chem Soc* 1954, *76* (19), 4755-4763.

96. Ball, P. Water as an active constituent in cell biology. *Chem Rev* 2008, *108* (1), 74-108.

97. Lumry, R.; Rajender, S. Enthalpy-Entropy Compensation Phenomena in Water Solutions of Proteins and Small Molecules - a Ubiquitous Property of Water. *Biopolymers* 1970, *9* (10), 1125-&.

98. Chaplin, M. Opinion - Do we underestimate the importance of water in cell biology? *Nat Rev Mol Cell Bio* 2006, *7* (11), 861-866.

99. Curtis, R. A.; Ulrich, J.; Montaser, A.; Prausnitz, J. M.; Blanch, H. W. Protein-protein interactions in concentrated electrolyte solutions - Hofmeister-series effects. *Biotechnol Bioeng* 2002, *79* (4), 367-380.

100. Huang, X.; Li, M.; Green, D. C.; Williams, D. S.; Patil, A. J.; Mann, S. Interfacial assembly of protein-polymer nano-conjugates into stimulus-responsive biomimetic protocells. *Nat Commun* 2013, *4*.

101. Sokolova, E.; Spruijt, E.; Hansen, M. M. K.; Dubuc, E.; Groen, J.; Chokkalingam, V.; Piruska, A.; Heus, H. A.; Huck, W. T. S. Enhanced transcription rates in membrane-free protocells formed by coacervation of cell lysate. *P Natl Acad Sci USA* 2013, *110* (29), 11692-11697.

102. Crosby, J.; Treadwell, T.; Hammerton, M.; Vasilakis, K.; Crump, M. P.; Williams, D. S.; Mann, S. Stabilization and enhanced reactivity of actinorhodin polyketide synthase

minimal complex in polymer-nucleotide coacervate droplets. *Chem Commun* 2012, *48* (97), 11832-11834.

103. Keating, C. D. Aqueous Phase Separation as a Possible Route to Compartmentalization of Biological Molecules. *Accounts Chem Res* 2012, *45* (12), 2114-2124.

104. Kayitmazer, A. B.; Strand, S. P.; Tribet, C.; Jaeger, W.; Dubin, P. L. Effect of polyelectrolyte structure on protein-polyelectrolyte coacervates: Coacervates of bovine serum albumin with poly(diallyidimethylammonium chloride) versus chitosan. *Biomacromolecules* 2007, *8* (11), 3568-3577.

105. Ali, S.; Bettelheim, F. A. Non-Freezing Water in Protein Solutions. *Colloid Polym Sci* 1985, *263* (5), 396-398.

106. Hills, B. P.; Takacs, S. F.; Belton, P. S. The Effects of Proteins on the Proton Nmr Transverse Relaxation-Times of Water .1. Native Bovine Serum-Albumin. *Mol Phys* 1989, *67* (4), 903-918.

107. Mathurdevre, R. Nmr-Studies of Water in Biological-Systems. *Prog Biophys Mol Bio* 1979, *35* (2), 103-134.

108. Tompa, K.; Bokor, M.; Verebélyi, T.; Tompa, P. Water rotation barriers on protein molecular surfaces. *Chemical Physics* 2015, *448*.

109. Rupley, J. A.; Careri, G. Protein Hydration and Function. *Adv Protein Chem* 1991, *41*, 37-172.

110. Yang, P. H.; Rupley, J. A. Protein-Water Interactions - Heat-Capacity of the Lysozyme-Water System. *Biochemistry-Us* 1979, *18* (12), 2654-2661.

111. Meister, K.; Strazdaite, S.; DeVries, A. L.; Lotze, S.; Olijve, L. L. C.; Voets, I. K.; Bakker, H. J. Observation of ice-like water layers at an aqueous protein surface. *P Natl Acad Sci USA* 2014, *111* (50), 17732-17736.

112. de Kruif, C. G.; Pedersen, J.; Huppertz, T.; Anema, S. G. Coacervates of Lactotransferrin and beta- or kappa-Casein: Structure Determined Using SAXS. *Langmuir* 2013, *29* (33), 10483-10490.

113. Kizilay, E.; Seeman, D.; Yan, Y.; Du, X.; Dubin, P. L.; Donato-Capel, L.; Bovetto, L.; Schmitt, C. Structure of bovine beta-lactoglobulin-lactoferrin coacervates. *Soft Matter* 2014.

114. Flanagan, S. E.; Malanowski, A. J.; Kizilay, E.; Seeman, D.; Dubin, P. L.; Donato-Capel, L.; Bovetto, L.; Schmitt, C. Complex Equilibria, Speciation, and Heteroprotein Coacervation of Lactoferrin and β-Lactoglobulin. *Langmuir* 2015.

115. Swanson-Vethamuthu, M.; Dubin, P. L.; Almgren, M.; Li, Y. J. Cryo-TEM of polyelectrolyte-micelle complexes. *J Colloid Interf Sci* 1997, *186* (2), 414-419.

116. Kayitmazer, A. B.; Bohidar, H. B.; Mattison, K. W.; Bose, A.; Sarkar, J.; Hashidzume, A.; Russo, P. S.; Jaeger, W.; Dubin, P. L. Mesophase separation and probe dynamics in protein-polyelectrolyte coacervates. *Soft Matter* 2007, *3* (8), 1064-1076.

117. Kizilay, E. Coacervation of Oppositely Charged Macromolecules, Micelles and Proteins: Disproportionation and Hierarchical Structures. Ph.D, University of Massachusetts - Amherst2014.

118. Hatakeyama, T.; Hatakeyama, H.; Nakamura, K. Non-Freezing Water-Content of Monovalent and Divalent Cation Salts of Polyelectrolyte Water-Systems Studied by Dsc. *Thermochim Acta* 1995, *253*, 137-148.

119. Wang, Y. L.; Kimura, K.; Dubin, P. L.; Jaeger, W. Polyelectrolyte-micelle coacervation: Effects of micelle surface charge density, polymer molecular weight, and polymer/surfactant ratio. *Macromolecules* 2000, *33* (9), 3324-3331.

120. Chen, B. L.; Arakawa, T.; Morris, C. F.; Kenney, W. C.; Wells, C. M.; Pitt, C. G. Aggregation Pathway of Recombinant Human Keratinocyte Growth-Factor and Its Stabilization. *Pharmaceut Res* 1994, *11* (11), 1581-1587.

121. Hamada, H.; Arakawa, T.; Shiraki, K. Effect of Additives on Protein Aggregation. *Curr Pharm Biotechno* 2009, *10* (4), 400-407.

122. Mattison, K. W. Structure, mobility, and enzyme activity in protein-polyelectrolyte complexes. Ph.D, Purdue University1999.

123. Marichal-Gallardo, P. A.; Alvarez, M. M. State-of-the-art in downstream processing of monoclonal antibodies: Process trends in design and validation. *Biotechnol Progr* 2012, *28* (4), 899-916.

124. Sule, S. V.; Cheung, J. K.; Antochshuk, V.; Bhalla, A. S.; Narasimhan, C.; Baisdell, S.; Shameem, M.; Tessier, P. M. Solution pH That Minimizes Self-Association of Three Monoclonal Antibodies Is Strongly Dependent on Ionic Strength. *Mol Pharmaceut* 2012, *9* (4), 744-751.

125. Nishi, H.; Miyajima, M.; Nakagami, H.; Noda, M.; Uchiyama, S.; Fukui, K. Phase Separation of an IgG1 Antibody Solution under a Low Ionic Strength Condition. *Pharm Res-Dordr* 2010, *27* (7), 1348-1360.

126. Mason, B. D.; Zhang, L.; Remmele, R. L.; Zhang, J. F. Opalescence of an IgG2 Monoclonal Antibody Solution as it Relates to Liquid-Liquid Phase Separation. *J Pharm Sci-Us* 2011, *100* (11), 4587-4596.

127. Sule, S. V.; Sukumar, M.; Weiss, W. F.; Marcelino-Cruz, A. M.; Sample, T.; Tessier, P. M. High-Throughput Analysis of Concentration-Dependent Antibody Self-Association. *Biophys J* 2011, *101* (7), 1749-1757.

128. Johnson, H. R.; Lenhoff, A. M. Characterization and Suitability of Therapeutic Antibody Dense Phases for Subcutaneous Delivery. *Mol. Pharmaceutics* 2013, *10* (10), 3582–3591.

129. Trilisky, E.; Gillespie, R.; Osslund, T. D.; Vunnum, S. Crystallization and Liquid-Liquid Phase Separation of Monoclonal Antibodies and Fc-Fusion Proteins: Screening Results. *Biotechnol Progr* 2011, *27* (4), 1054-1067.

130. Ahmad, S. S.; Dalby, P. A. Thermodynamic parameters for salt-induced reversible protein precipitation from automated microscale experiments. *Biotechnol Bioeng* 2011, *108* (2), 322-32.

131. Shukla, A. A.; Thommes, J. Recent advances in large-scale production of monoclonal antibodies and related proteins. *Trends Biotechnol* 2010, *28* (5), 253-261.

132. Wang, Y.; Lomakin, A.; Latypov, R. F.; Laubach, J. P.; Hideshima, T.; Richardson, P. G.; Munshi, N. C.; Anderson, K. C.; Benedek, G. B. Phase transitions in human IgG solutions. *J Chem Phys* 2013, *139* (12).

133. Yadav, S.; Laue, T. M.; Kalonia, D. S.; Singh, S. N.; Shire, S. J. The Influence of Charge Distribution on Self-Association and Viscosity Behavior of Monoclonal Antibody Solutions. *Mol Pharmaceut* 2012, *9* (4), 791-802.

134. Yearley, E. J.; Zarraga, I. E.; Shire, S. J.; Scherer, T. M.; Gokarn, Y.; Wagner, N. J.; Liu, Y. Small-Angle Neutron Scattering Characterization of Monoclonal Antibody Conformations and Interactions at High Concentrations. *Biophys J* 2013, *105* (3), 720-731.

135. Xu, Y.; Dubin, P. Protein purification by polyelectrolyte coacervation: Influence of protein charge anisotropy on selectivity. *Abstr Pap Am Chem S* 2012, *243*.

136. Chaudhri, A.; Zarraga, I. E.; Yadav, S.; Patapoff, T. W.; Shire, S. J.; Voth, G. A. The Role of Amino Acid Sequence in the Self-Association of Therapeutic Monoclonal Antibodies: Insights from Coarse-Grained Modeling. *J Phys Chem B* 2013, *117* (5), 1269-1279.

137. Lilyestrom, W. G.; Yadav, S.; Shire, S. J.; Scherer, T. M. Monoclonal Antibody Self-Association, Cluster Formation, and Rheology at High Concentrations. *J Phys Chem B* 2013, *117* (21), 6373-6384.

138. Tscheliessnig, A. L.; Konrath, J.; Bates, R.; Jungbauer, A. Host cell protein analysis in therapeutic protein bioprocessing - methods and applications. *Biotechnol J* 2013, *8* (6), 655-670.

139. Du, X. S.; Dubin, P. L.; Hoagland, D. A.; Sun, L. H. Protein-Selective Coacervation with Hyaluronic Acid. *Biomacromolecules* 2014, *15* (3), 726-734.

140. Gottschalk, U. The renaissance of protein purification. *Biopharm Int* 2006, 8-9.

141. Shukla, A. A.; Hubbard, B.; Tressel, T.; Guhan, S.; Low, D. Downstream processing of monoclonal antibodies - Application of platform approaches. *J Chromatogr B* 2007, *848* (1), 28-39.

142. Ghose, S.; Allen, M.; Hubbard, B.; Brooks, C.; Cramer, S. M. Antibody variable region interactions with Protein A: Implications for the development of generic purification processes. *Biotechnol Bioeng* 2005, *92* (6), 665-673.

143. Tarrant, R. D. R.; Velez-Suberbie, M. L.; Tait, A. S.; Smales, C. M.; Bracewell, D. G. Host cell protein adsorption characteristics during protein a chromatography. *Biotechnol Progr* 2012, *28* (4), 1037-1044.

144. Connell-Crowley, L.; Nguyen, T.; Bach, J.; Chinniah, S.; Bashiri, H.; Gillespie, R.; Moscariello, J.; Hinckley, P.; Dehghani, H.; Vunnum, S.; Vedantham, G. Cation exchange chromatography provides effective retrovirus clearance for antibody purification processes. *Biotechnol Bioeng* 2012, *109* (1), 157-165.

145. Stein, A.; Kiesewetter, A. Cation exchange chromatography in antibody purification: pH screening for optimised binding and HCP removal. *J Chromatogr B* 2007, *848* (1), 151-158.

146. Follman, D. K.; Farner, R. L. Factorial screening of antibody purification processes using three chromatography steps without protein A. *J Chromatogr A* 2004, *1024* (1-2), 79-85.

147. Huang, M.; Vitharana, S. N.; Peek, L. J.; Coop, T.; Berkland, C. Polyelectrolyte complexes stabilize and controllably release vascular endothelial growth factor. *Biomacromolecules* 2007, *8* (5), 1607-1614.

148. Boyoglu, S.; Vig, K.; Pillai, S.; Rangari, V.; Dennis, V.; Khazi, F.; Singh, S. R. Enhanced delivery and expression of a nanoencapsulated DNA vaccine vector for respiratory syncytial virus. *Nanomed-Nanotechnol* 2009, *5* (4), 463-472.

149. Dass, C. R.; Contreras, K. G.; Dunstan, D. E.; Choong, P. F. M. Chitosan microparticles encapsulating PEDF plasmid demonstrate efficacy in an orthotopic metastatic model of osteosarcoma. *Biomaterials* 2007, *28* (19), 3026-3033.

150. Li, Z. S.; Ramay, H. R.; Hauch, K. D.; Xiao, D. M.; Zhang, M. Q. Chitosan-alginate hybrid scaffolds for bone tissue engineering. *Biomaterials* 2005, *26* (18), 3919-3928.

151. Elbert, D. L. Liquid-liquid two-phase systems for the production of porous hydrogels and hydrogel microspheres for biomedical applications: A tutorial review. *Acta Biomater* 2011, *7* (1), 31-56.

152. Xia, J. L.; Mattison, K.; Romano, V.; Dubin, P. L.; Muhoberac, B. B. Complexation of trypsin and alcohol dehydrogenase with poly(diallyldimethylammonium chloride). *Biopolymers* 1997, *41* (4), 359-365.

153. Dubin, P. L.; Muhoberac, B. B.; Xia, J. Enzyme-Polyelectrolyte Coacervate Complex and Method of Use. *U.S. Patent 5834271* 1998.

154. Capito, F.; Bauer, J.; Rapp, A.; Schroter, C.; Kolmar, H.; Stanislawski, B. Feasibility Study of Semi-Selective Protein Precipitation With Salt-Tolerant Copolymers for Industrial Purification of Therapeutic Antibodies. *Biotechnol Bioeng* 2013, *110* (11), 2915-2927.

155. Capito, F.; Skudas, R.; Stanislawski, B.; Kolmar, H. Polyelectrolyte-protein interaction at low ionic strength: required chain flexibility depending on protein average charge. *Colloid Polym Sci* 2013, *291* (7), 1759-1769.

156. McDonald, P.; Victa, C.; Carter-Franklin, J. N.; Fahrner, R. Selective Antibody Precipitation Using Polyelectrolytes: A Novel Approach to the Purification of Monoclonal Antibodies. *Biotechnol Bioeng* 2009, *102* (4), 1141-1151.

157. Peram, T.; McDonald, P.; Carter-Franklin, J.; Fahrner, R. Monoclonal Antibody Purification Using Cationic Polyelectrolytes: An Alternative to Column Chromatography. *Biotechnol Progr* 2010, *26* (5), 1322-1331.

158. Sieberz, J.; Stanislawski, B.; Wohlgemuth, K.; Schembecker, G. Identification of parameter interactions influencing the precipitation of a monoclonal antibody with anionic polyelectrolytes. *Sep Purif Technol* 2014, *127*, 165-173.

159. Wang, J.; Diehl, T.; Aguiar, D.; Dai, X. P.; Arunakumari, A. Precipitation of Process-Derived Impurities in Non-Protein A Purification Schemes for Antibodies. *Biopharm Int* 2009, 4-+.

160. Rathore, A. S.; Kumar, V.; Tugcu, N.; Godavarti, R. Evolution of the Monoclonal Antibody Purification Platform. *Biopharm Int* 2013, *26* (11), 32-+.

161. Shamashkin, M.; Godavarti, R.; Iskra, T.; Coffman, J. A Tandem Laboratory Scale Protein Purification Process Using Protein A Affinity and Anion Exchange Chromatography Operated in a Weak Partitioning Mode. *Biotechnol Bioeng* 2013, *110* (10), 2655-2663.

162. Lee, H.; Cho, I. H.; Moon, M. H. Effect of dissolution temperature on the structures of sodium hyaluronate by flow field-flow fractionation/multiangle light scattering. *J Chromatogr A* 2006, *1131* (1-2), 185-191.

163. Dubin, P. L.; Gao, J.; Mattison, K. Protein-Purification by Selective Phase-Separation with Polyelectrolytes. *Separ Purif Method* 1994, *23* (1), 1-16.

164. Wang, Y. F.; Gao, J. Y.; Dubin, P. L. Protein separation via polyelectrolyte coacervation: Selectivity and efficiency. *Biotechnol Progr* 1996, *12* (3), 356-362.

165. Lesins, V.; Ruckenstein, E. Patch Controlled Attractive Electrostatic Interactions between Similarly Charged Proteins and Adsorbents. *Colloid Polym Sci* 1988, *266* (12), 1187-1190.

166. Mattison, K. W.; Dubin, P. L.; Brittain, I. J. Complex formation between bovine serum albumin and strong polyelectrolytes: Effect of polymer charge density. *J Phys Chem B* 1998, *102* (19), 3830-3836.

167. Antonov, M.; Mazzawi, M.; Dubin, P. L. Entering and Exiting the Protein-Polyelectrolyte Coacervate Phase via Nonmonotonic Salt Dependence of Critical Conditions. *Biomacromolecules* 2010, *11* (1), 51-59.

168. Draft Guidance for Industry from FDA: Quality Considerations in Demonstrating Biosimilarity to a Reference Protein Product. *Biotechnol Law Rep* 2012, *31* (2), 185-195.

169. Wen, J.; Arakawa, T.; Philo, J. S. Size-exclusion chromatography with on-line light-scattering, absorbance, and refractive index detectors for studying proteins and their interactions. *Anal Biochem* 1996, *240* (2), 155-166.

170. Marassi, V.; Roda, B.; Zattoni, A.; Tanase, M.; Reschiglian, P. Hollow fiber flow field-flow fractionation and size-exclusion chromatography with multi-angle light scattering detection: A complementary approach in biopharmaceutical industry. *J Chromatogr A* 2014, *1372*, 196-203.

171. Lowe, D.; Dudgeon, K.; Rouet, R.; Schofield, P.; Jermutus, L.; Christ, D. Aggregation, Stability, and Formulation of Human Antibody Therapeutics. *Adv Protein Chem Str* 2011, *84*, 41-61.

172. Wang, Y. W.; Teraoka, I.; Hansen, F. Y.; Peters, G. H.; Hassager, O. A Theoretical Study of the Separation Principle in Size Exclusion Chromatography. *Macromolecules* 2010, *43* (3), 1651-1659.

173. Ritter, A.; Schmid, M.; Affolter, S. Determination of molecular weights by size exclusion chromatography (SEC) - Results of round robin tests. *Polym Test* 2010, *29* (8), 945-952.

174. Dubin, P. L.; Principi, J. M. Failure of Universal Calibration for Size Exclusion Chromatography of Rodlike Macromolecules Versus Random Coils and Globular-Proteins. *Macromolecules* 1989, *22* (4), 1891-1896.

175. Meunier, D. M.; Lyons, J. W.; Kiefer, J. J.; Niu, Q. J.; DeLong, L. M.; Li, Y. F.; Russo, P. S.; Cueto, R.; Edwin, N. J.; Bouck, K. J.; Silvis, H. C.; Tucker, C. J.; Kalantar, T. H. Determination of Particle Size Distributions, Molecular Weight Distributions, Swelling, Conformation, and Morphology of Dilute Suspensions of Cross-Linked Polymeric Nanoparticles via Size-Exclusion Chromatography/Differential Viscometry. *Macromolecules* 2014, *47* (19), 6715-6729.

176. Senak, L.; Wu, C. S.; Malawer, E. G. Size Exclusion Chromatography of Poly(Vinylpyrrolidone) .2. Absolute Molecular-Weight Distribution by Sec Lalls and Sec with Universal Calibration. *J Liq Chromatogr* 1987, *10* (6), 1127-1150.

177. Gaborieau, M.; Nicolas, J.; Save, M.; Charleux, B.; Vairon, J. P.; Gilbert, R. G.; Castignolles, P. Separation of complex branched polymers by size-exclusion chromatography probed with multiple detection. *J Chromatogr A* 2008, *1190* (1-2), 215-223.

178. Shah, G.; Dubin, P. L. Adsorptive Interaction of Ficoll Standards with Porous-Glass Size-Exclusion Chromatography Columns. *J Chromatogr A* 1995, *693* (2), 197-203.

179. Romano, V. A.; Ebeyer, T.; Dubin, P. L. Influence of net protein charge and stationary phase charge on protein retention in size exclusion chromatography. *Acs Sym Ser* 1996, *635*, 88-102.

180. Cai, C. H.; Romano, V. A.; Dubin, P. L. Ionic Strength Dependence of Protein Retention on Superose-12 in Sec-Iec Mixed-Mode Chromatography. *J Chromatogr A* 1995, *693* (2), 251-261.

181. Dubin, P. L.; Edwards, S. L.; Kaplan, J. I.; Mehta, M. S.; Tomalia, D.; Xia, J. L. Carboxylated Starburst Dendrimers as Calibration Standards for Aqueous Size Exclusion Chromatography. *Anal Chem* 1992, *64* (20), 2344-2347.